Scattering and absorption in 2D optics

Mariani, F.

Scattering and absorption in 2D optics

PROEFSCHRIFT

ter verkrijging van
de graad van Doctor aan de Universiteit Leiden,
op gezag van Rector Magnificus prof. mr. C. J. J. M. Stolker,
volgens besluit van het College voor Promoties
te verdedigen op dinsdag 6 maart 2018
klokke 13:45 uur

door

Flavio Mariani

geboren te Foligno, Italië
in 1983

Promotores:	Prof. dr. M. P. van Exter	Universiteit Leiden
	Prof. dr. E. R. Eliel	Universiteit Leiden
Promotiecommissie:	Prof. dr. M. A. G. J. Orrit	Universiteit Leiden
	Prof. dr. W. L. Vos	Technical University of Twente
	Prof. dr. L. M. Moreno	Universidad de Zaragoza, Spain
	Dr. M. J. A. de Dood	Universiteit Leiden
	Prof. dr. C. U. Keller	Universiteit Leiden

Casimir PhD series, Delft-Leiden 2017-48

ISBN: 978-90-8593-332-8

An electronic version of this dissertation is available at:
https://openaccess.leidenuniv.nl

The research described in this thesis was conducted at the 'Leids Instituut voor Onderzoek in de Natuurkunde' (LION). This work is part of the research program of the Foundation for Fundamental Research on Matter (FOM), which is part of the Netherlands Organization for Scientific Research (NWO).

Cover image: light reflected by a thin-film silicon solar cell illuminated with linearly polarized coherent light. The co-polarized and depolarized reflected intensity are shown in red and green, respectively. A portion of the surface illuminated with incoherent light is visible on the back cover. The width of the name on the cover is equivalent to 10 μm.

Science is more than a body of knowledge, it's a way of thinking.
A way of skeptically interrogating the universe
with a fine understanding of human fallibility.

Carl Sagan

Contents

Chapter 1

Introduction

This chapter introduces the reader to light scattering, the central topic in this thesis, and to its role in the nano-optics structures that we studied. With this purpose in mind, we focus our discussion on two recurring themes: optics in two-dimensional structures and optical scattering in random media.
We end with an overview of the content of the main chapters of this thesis.

1.1 Scattering of light: an intuitive picture

Scattering of light is a phenomenon that belongs to everyday life much more than in a dark optics laboratory [1]. Without light scattering we would only be able to see objects that produce light, like the sun or a lamp, or opaque objects that obstruct our sight of a light source. Scattering allows us to see more. When light from a source hits an objects and reaches the eye after changing direction, hence scatters on it, only then does most of vision begin.

Scattering happens in the presence of a change in the environment or at a discontinuity in the optical path of the incident light. Intuition is again supported by an everyday example: a clear slab of glass doesn't disturb light propagation much and it is thus hardly detectable. On the contrary, the slab can easily be seen if there is a scratch on its surface (the discontinuity), or some dirt.

Similarly to how we rely on scattering to interpret the properties of what surrounds us, in the controlled conditions of an optics experiment scattering is a useful tool to investigate the interaction of light with matter, from the macroscopic scale to the single molecule level. The work collected in this dissertation is a study around different examples of scattering of light in the presence of nano-structured materials, i.e. with features in the order of the wavelength of the light, or smaller.

Before presenting an overview of our work, we will address two key ingredients of our research: the quasi-two-dimensional confinement of the light as an effect of the structuring of the materials, and scattering in random media.

1.2 Two dimensional optics

Apart from freely propagating in space, light can also exist in states confined on quasi two-dimensional structures, with dielectric layers [2, 3, 4] and metal-dielectric interfaces [5] as main examples.

The simplest case of a dielectric layer is a thin membrane, surrounded by a material of lower refractive index. One possible example is a thin film of a dielectric or semiconductor of a thickness in the order of the wavelength of light and air on both sides. Under these conditions, Maxwell's equations have a set of discrete solutions, or guided modes, which describe how the electromagnetic field is localized on the structure in the transverse direction, with in-plane propagation only allowed.

The interface between a metal and a dielectric also yields a confined so-

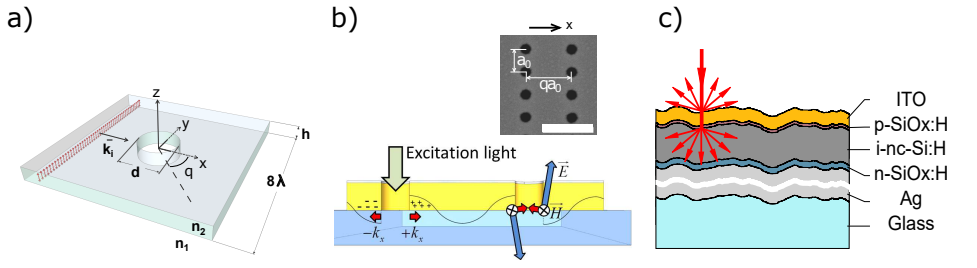

Figure 1.1: The three two-dimensional optical structures studied in this thesis. a) a single hole in a dielectric slab scatters a waveguide mode propagating in the slab (see Chapter 2). b) a regular array of holes in a metal film on a glass substrate enables the excitation and scattering of surface plasmons (SP) that propagate on the metal-glass interface; the symbols in the lower picture indicate the relevant processes; the scale bar in the SEM picture is 1 micrometer (see Chapter 3). c) a rough thin film Si solar cell scatters the incident light into trapped states inside the quasi two-dimensional structure (see Chapter 5)

lution for the electromagnetic field. This solution is the surface plasmon, for which the electromagnetic (EM) field is coupled to free charges oscillating in the metal, and is tightly confined to the interface [6, 7, 8].

The EM field of both waveguide modes and surface plasmons decay exponentially away from the 2D structure on which they are confined. Both modes don't exchange energy with the outside in either direction when unperturbed. A consequence of this is that their creation and detection require particular geometries or the presence of nanostructures. The easiest nanostructures widely used in two-dimensional structures are subwavelength cylindrical holes. In Chapters 2 and 3 we study how light interacts with single holes for a dielectric waveguide (Fig. 1.1 (a)) and for surface plasmons (Fig. 1.1 (b)), respectively.

1.3 Random scattering

Complex media are literally everywhere and comprise materials like paint or fog [9, 10], but also cells and bone tissues [11, 12]. This makes them particularly interesting to study and extensive research exists on the control of light propagation in random scattering media in different fields [13, 14]. Research on scattering finds applications in the technological improvements of devices that emit or absorb light, like LEDs and solar cells [15, 16, 17].

Scattering materials are made of randomly arranged scattering elements. The main effect of this on light is to scramble its propagation direction, making

it impossible to look through them. When illuminated with coherent light, the reflection of random scattering media has a complex structure that depends on the internal structure of the medium and is named speckle-pattern [18].

In Chapters 4 and 5 we present two experimental studies on the reflected speckles from respectively 3D scattering media and a 2D scattering solar cell. Both studies are based on the deterministic nature of random scattering and its linear relation between input and output EM field.

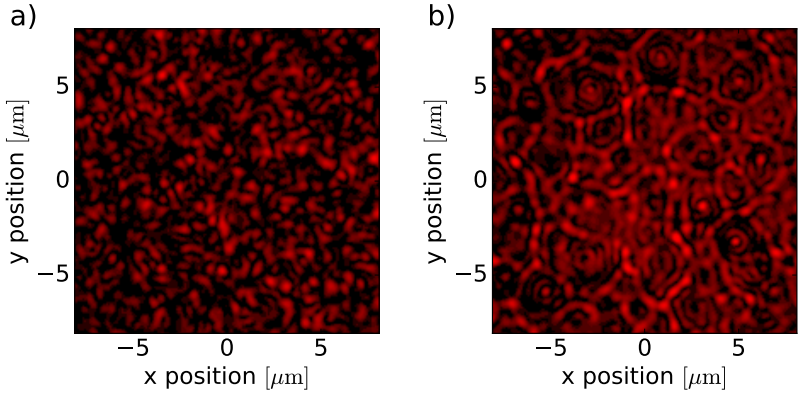

Figure 1.2: Two example of reflected intensity patterns from a 3D scattering medium like (a) a 3D scattering medium in form of white paint and (b) a two-dimensional rough thin film Si solar cell. In both cases the intensity shows a speckle pattern but with a very different structure for the two cases, and with a resemblance of the sample morphology in the case of the solar cell.

1.4 Overview of this thesis

This thesis is divided into four main chapters, and it concludes with a summary of the presented results.

In Chapter 2 we consider the scattering of waveguided light on a single cylindrical hole in a thin dielectric membrane. We use numerical simulation to calculate the properties of the scattering process, separating the in-plane scattering from the radiative loss induced by out-of-plane scattering at the hole.

In Chapter 3 we investigate how surface plasmons scatter on nano-holes in gold. We study this experimentally for extended arrays of holes with spacing in the order of the wavelength of the surface plasmons, and multiples thereof. We exploit interference effects to effectively use the arrays as optical gratings,

and reconstruct the far field profile characteristics of the light scattered by a single hole.

In Chapter 4 we demonstrate a new method to measure scattering and absorption properties of a complex medium like white paint. We employ a wavefront shaping technique to modulate only the optical phase of the illumination on the sample. We record its effect on the reflected speckle pattern and interpret it using a simple diffusion model. This method can be applied to any complex medium for which light transport can be modelled statistically.

In Chapter 5 we study the scattering properties of a rough thin Si solar cell under coherent illumination, i.e. different from the condition under which solar cells usually operate. This experiment provides valuable information on how light enters the cell and reflects from it. Our study brings a nano-photonic approach to the study of thin-film solar cells. Our aim is to provide a physical picture of the processes of light propagation and absorption, up to the point where we can use wavefront-shaping techniques to increase the in-coupling of light in a solar cell and improve its performances. Chapter 5 presents the first steps in that direction.

Bibliography

[1] M. Minnaert, *Light and Color in the Outdoors* (Springer Science & Business Media) (1995).

[2] S. McNab, N. Moll, and Y. Vlasov, *Ultra-low loss photonic integrated circuit with membrane-type photonic crystal waveguides*, Opt. Express **11**, 2927 (2003).

[3] J. L. O'Brien, A. Furusawa, and J. Vučković, *Photonic quantum technologies*, Nat Photon **3**, 687 (2009).

[4] J. D. Joannopoulos, P. R. Villeneuve, and S. Fan, *Photonic crystals: putting a new twist on light*, Nature **386**, 143 (1997).

[5] R. H. Ritchie, *Plasma Losses by Fast Electrons in Thin Films*, Phys. Rev. **106**, 874 (1957).

[6] W. L. Barnes, A. Dereux, and T. W. Ebbesen, *Surface plasmon subwavelength optics*, Nature **424**, 824 (2003).

[7] L. Yin *et al.*, *Subwavelength Focusing and Guiding of Surface Plasmons*, Nano Lett. **5**, 1399 (2005).

[8] D. K. Gramotnev and S. I. Bozhevolnyi, *Plasmonics beyond the diffraction limit*, Nat Photon **4**, 83 (2010).

[9] M. C. W. van Rossum and T. M. Nieuwenhuizen, *Multiple scattering of classical waves: microscopy, mesoscopy, and diffusion*, Rev. Mod. Phys. **71**, 313 (1999).

[10] P. M. Johnson, T. van der Beek, and A. Lagendijk, *Diffuse imaging and radius dependent frequency correlations in strongly scattering media*, Optics Express **22**, 13330 (2014).

[11] T. J. Farrell, M. S. Patterson, and B. Wilson, *A diffusion theory model of spatially resolved, steady-state diffuse reflectance for the noninvasive determination of tissue optical properties invivo*, Medical Physics **19**, 879 (1992).

[12] L. Cortese *et al.*, *Anisotropic Light Transport in White Beetle Scales*, Advanced Optical Materials **3**, 1337 (2015).

[13] I. M. Vellekoop and A. P. Mosk, *Focusing coherent light through opaque strongly scattering media*, Opt. Lett. **32**, 2309 (2007).

[14] J. Bertolotti *et al.*, *Non-invasive imaging through opaque scattering layers*, Nature **491**, 232 (2012).

[15] M. L. Meretska *et al.*, *Analytical modeling of light transport in scattering materials with strong absorption*, Opt. Express **25**, A906 (2017).

[16] M. Burresi *et al.*, *Two-dimensional disorder for broadband, omnidirectional and polarization-insensitive absorption*, Opt. Express **21**, A268 (2013).

[17] M. Zeman *et al.*, *Advanced Light Management Approaches for Thin-Film Silicon Solar Cells*, Vol. 15 of *International Conference on Materials for Advanced Technologies 2011, Symposium O*, Energy Procedia **15**, 189 (2012).

[18] J. W. Goodman, *Speckle phenomena in optics: theory and applications* (Roberts and Company Publishers) (2007).

Scattering of guided light by a single hole in a dielectric slab

We study the scattering of waveguided light by a single hole in a dielectric slab with FDTD simulations and investigate two scattering processes: two dimensional (2D) scattering into slab modes and three-dimensional (3D) scattering into the surroundings. We find that 2D scattering tipically dominates over the 3D losses. We find important quantitative differences between the single hole scattering and the case of scattering from an infinite Mie cylinder. Additionally, we find that a hole cannot be simply modelled as a dipolar object even in the limit of small scatterers (Rayleigh approximation). This is visible from the angular dependence of the 2D scattered intensity. We discuss the relevance of our findings in the modelling of two dimensional random scattering media.

This chapter is published as:
F.Mariani, M.P. van Exter, Optics Express **23**, 17539 (2015).

2.1 2D optics in dielectric slabs

Dielectric membranes are popular substrates for nano-photonic applications [1, 2, 3]. They confine light in two dimensions acting as a waveguide if embedded in a lower refractive index material. Additional spatial control can be achieved by nano-structuring the planar geometry with arrangements of scatterers such as nano-holes. In this way two dimensional photonic crystals [4] are obtained in dielectric membranes and interesting phenomena like photonic bandgaps can appear with proper tuning of the geometry [5, 6], allowing the design of integrated optical circuits with membrane based components like waveguides and cavities [7, 8].

Two dimensional optics is in general subject to losses, caused by material absorption, for instance by defects, or by imperfect nano-structuring of the membrane. Limits in the fabrication process can introduce positional disorder of the scatterers and interface roughness; both of these scatter light outside the waveguide into radiative modes which act as losses for the 2D system. The losses have been calculated by modelling the scattering due to position and shape disorder [9] and roughness via the polarizability of small scatterers [10, 11].

Beside fabrication imperfections, also a geometrically perfect hole gives rise to radiative losses. A hole in a dielectric slab is a discontinuity in the waveguide and can thus scatter light both in the slab (2D scattering) and in the third dimension (3D scattering), determining effective losses. The scattering properties of round holes in dielectric environment have been calculated for simplified geometries, like slits in a slab [12] , infinitely long cylinders [13, 14, 15] and periodic lattices of holes [16, 17], where the first two geometries effectively reduce the dimension of the problem from 3D to 2D.

Although an analytic approach to the scattering from a hole in a layered structure, based on cylindrical mode expansion, is presented in [16], a more descriptive study on the scattering from a single hole in a free standing membrane is still missing. As we will show in the following, a hole in a slab is an interesting system and even for sub-wavelength holes (Rayleigh limit), the radiation profile doesn't resemble that of a radiating dipole in a slab. This finding is in contrast with the result obtained for infinitely long Mie cylinders and the scattering expected for sub-wavelength objects in a uniform 3D medium. Both these scattering processes are dipolar and can be analyzed by treating the scatterer as a polarizable object, even in the case of a hollow

inclusion in an otherwise uniform medium. A similar comparison with a complementary scattering system is less straightforward for the hole in a dielectric slab.

Understanding single hole scattering properties is essential for the description of two dimensional random scattering media. In these systems the field structure is difficult to calculate and it becomes necessary to introduce average transport properties [14, 18] and to use statistical approaches or simulations [19, 20]. The knowledge of the 2D and 3D scattering properties of individual holes could help to simplify the random scattering problem from a full 3D to a 2D problem with effective losses, for a less time consuming calculation of scattering properties.

In this work we use Finite Difference Time Domain (FDTD) simulations to study small holes in a dielectric slab under the excitation of guided light. After introducing our system in Sec. 2.2, we discuss our results for different hole diameters and mode confinements (Sec. 2.3.1) and describe two scattering processes: the 2D scattering in the slab and the 3D scattering in form of freely propagating radiative modes (Sec 2.3.2). We calculate the dependence of the scattering cross section on the hole diameter and the relative role of radiative losses with respect to in-plane scattering. Finally, we examine the angular distribution of the scattered intensity (Sec. 2.3.3) and compare it to the distribution expected for the case of a cylinder in the Rayleigh regime. We apply our results to the calculation of mean free path in random scattering media (Sec. 2.4).

2.2 Simulation method and scattering parameters

We consider the symmetric case of a thin film of dielectric material of real refractive index n_2, surrounded on both sides by a medium with $n_1 < n_2$. The film is oriented with its normal along the z-axis and extends for $-h/2 < z < h/2$, where h is the thickness of the slab. The slab contains a cylindrical hole of diameter d and index n_1 centred at the origin of the Cartesian reference. The problem is described by three relevant physical quantities: the relative refractive index of the material $n = n_2/n_1$, the slab thickness h and the hole diameter d. Without loss of generality, in the rest of the work we set $n_1 = 1$ and express h and d in units of λ_0, the wavelength of the light in vacuum.

Under the condition $n_1 < n_2$, a slab supports guided field modes satisfying the (roundtrip) condition $2h\sqrt{n_2^2 k_0^2 - \beta^2} + 2\phi_\mu(\beta) = 2\pi m$, where k_0 is the

wavevector in vacuum, β is the in-plane component of the wavevector, μ is the field polarization, and $\phi_\mu(\beta)$ is the polarization dependent phase acquired upon total internal reflection at the slab-cladding interface [21]. For the polarization μ we use the convention of indicating with TM (TE) the field with magnetic (electric) field parallel to the plane of the waveguide. The integer modal index m assumes values which depend on the slab geometry: the number of allowed modes increases with slab thickness and in the case of symmetric slabs one TM and one TE mode are always present. We choose the thickness of our slab such that it only supports these two fundamental $m = 0$ modes. This condition simplifies our description and is also the typical situation in membrane-based optics.

We will compare the scattering from a single hole in the waveguide with the Mie theory for scattering of a plane wave from an infinitely long cylinder. In the latter case, the symmetry of problem allows expanding the electromagnetic field in cylindrical harmonics to obtain exact scattering functions [22], but this approach doesn't apply to our geometry. A hole in a slab is also different from a finite size cylinder excited by a plane wave [23, 24]. The main distinctive aspects are: (i) the vertical translational symmetry of the Mie case is missing in a thin film, (ii) the field incident on the hole in the slab is not a plane wave but has a varying amplitude across the hole and an evanescent field portion extending outside the slab, (iii) the hole has end faces that are not present in the Mie cylinder and can contribute to the scattering. Given the peculiar geometry of our problem, we choose a numerical approach.

We describe the scattering processes using the scattering efficiencies Q. These are dimensionless numbers defined as the ratio of scattering cross section and geometrical cross section. Taking into account a portion of length L of an infinitely extended cylinder of diameter d, the scattering efficiency Q_{sca} in the Mie case is:

$$Q_{sca} = \frac{\sigma_{sca}}{d\,L} = \frac{W_s}{I_i\,d\,L} \tag{2.1}$$

where I_i $[W/m^2]$ is the intensity of the incident wave, W_s $[W]$ is the power scattered by the cylinder portion and σ_{sca} $[m^2]$ its scattering cross section. We will modify Eq. (2.1) to account for the two-dimensional confinement of our problem. As for the scattering of surface plasmons from holes in a metal slab [25], we choose the cross section to have dimension of a length and we have:

$$Q_{2D} = \frac{\sigma_{2D}}{d} = \frac{W_{2D}}{\tilde{I}_i\,d} \tag{2.2}$$

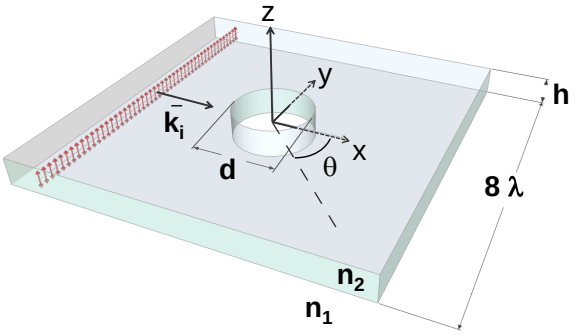

Figure 2.1: The simulation cell is $(8\lambda)^3$ in volume and surrounded by a λ-thick perfectly matching layer.

where $\tilde{I}_i$ $[W/m]$ is the intensity of the incident guided mode per unit length of the wavefront. The same definition holds for radiative losses into free space with the substitution $2D \rightarrow 3D$. Scattering efficiencies are in general polarization dependent but we do not indicate this explicitly in the notation.

2.3 2D scattering in the slab and 3D losses

In this section we present results obtained from simulations performed with the finite-difference time-domain (FDTD) method [26], using the freely available software package MEEP [27]. We simulate the scattering from a hole in a slab with refractive index $n_2 = 1.5$ and hole diameter chosen in the range $0.075 < d < 1.2$. We use slab thicknesses of $h = 0.25, 0.32, 0.40$, all below the cut-off for the appearance of the higher-order TM and TE modes. The simulation cell used for this work is shown in Fig. 2.1; it has side length of 8λ, a grid of 40 points/λ and is surrounded by perfect matching layers of thickness 1λ on each side. More details on the simulations are given in Appendix 2.A.

2.3.1 2D scattering in the small hole approximation

We first consider the 2D scattering process, i.e. the scattering into waveguided modes. An example of cross section of the scattered field in the $z = 0$ plane is shown in Fig. 2.2. Figure Fig. 2.3 shows the calculated scattering efficiencies Q_{2D} for three single-mode slabs of different thickness; these are compared to the scattering efficiency calculated with Mie theory for an infinitely long hollow cylinder (n_1=1) in a volume filled with the same dielectric of the slab waveguide. We report data for both TM_0 and TE_0 modes.

As shown in Fig. 2.3, scattering efficiency for the hole increases with the thickness of the slab, approaching the value for the Mie case for the thicker slab. This behaviour can be understood by looking at the spatial distribution

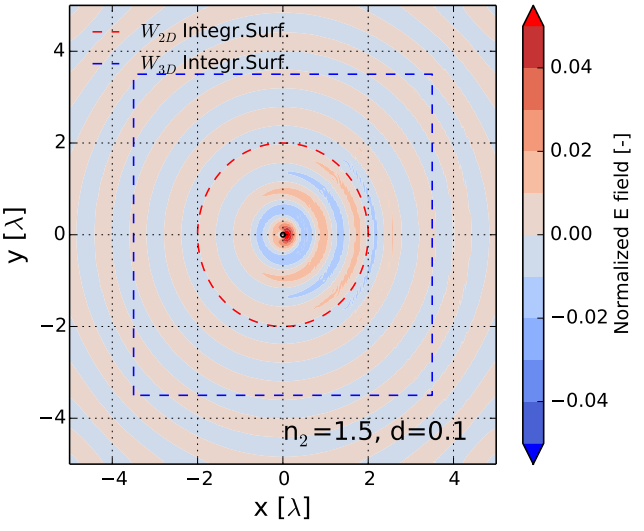

Figure 2.2: The calculated E_z component of the scattered electric field in the $z = 0$ plane for a hole diameter $d = 0.1\lambda$ and a waveguide thickness $h = 0.4\lambda$. The field is normalized to the amplitude of the incident E_z field. The red and blue dashed lines indicate the profiles of the surfaces for Poynting vector integration.

of the field that excites the hole: the fraction of the field that propagates inside the membrane increases with thickness, resulting in a stronger interaction with the dielectric discontinuity in the slab. We can quantify the fraction of the optical power inside the membrane using the confinement factor Γ ($0 < \Gamma < 1$) defined as:

$$\Gamma = \frac{\int_{slab} \vec{S'} \cdot \hat{x}\ dz}{\int \vec{S'} \cdot \hat{x}\ dz} \tag{2.3}$$

where $\vec{S'}$ is the time averaged Poynting vector and $\hat{x}$ the direction of propagation. Values of the confinement factors in our geometries are reported in Table 2.1, where we also report the polarization dependent ratios $R_Q^\mu = Q_{2D}/Q_{sca}$ for calculated scattering efficiency compared to the Mie case. As visible in Fig. 2.4, R_Q^μ shows a strong monotonic dependence on the confinement factor with a steep approach to the value of 1 for $\Gamma \to 1$; even for $\Gamma = 0.83$, $R_Q^\mu = 0.43$ in the TM case. This strong quantitative dependence is often not included when modelling disorder in membrane structures.

To check the dimensionality of our scattering problem, we fitted the calculated scattered efficiencies Q_{2D} with the polynomial dependence:

$$Q_{2D} = A\ r^p \tag{2.4}$$

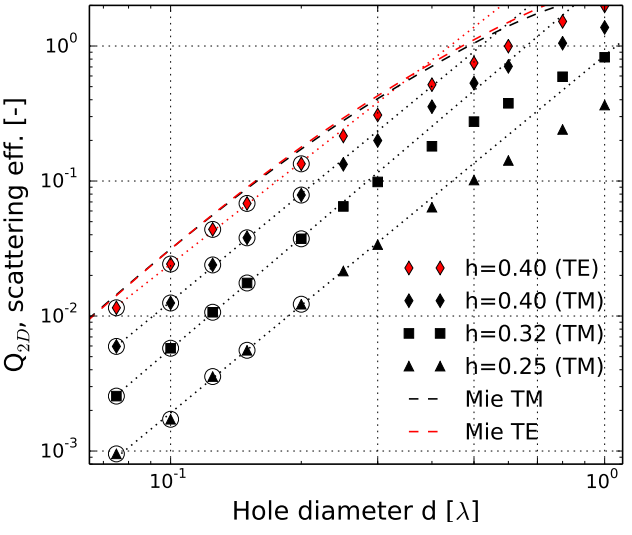

Figure 2.3: Calculated scattering efficiencies Q_{2D} as function of the diameter of the hole, for a slab refractive index of $n_2 = 1.5$. Data for TM_0 (in black) are plotted for three different thicknesses h in the single-mode regime. The TE_0 case (in red) is plotted only for the largest thickness. Polynomial fits $Q_{2D} = Ar^p$ were performed on data for $d \leq 0.2\lambda$ (encircled in the plot) and plotted as dotted lines. The scattering efficiencies of a Mie cylinder for TM and TE polarization, respectively shown in black and red dashed curves, have almost the same values in the examined diameters range.

with A and p as fitting parameters. The fit values reported in Table 2.1 are in the range $2.51 < p < 2.74$. The scattered power scales, in the 2D case, as $W_{2D} \propto r^4$ (induced dipole $\propto r^2 h$) and gives $Q_{2D} \propto r^3$ from Eq. (2.2). This is the 2D equivalent of the 3D scaling expected in the Rayleigh regime for small particles where $Q_{sph} \propto r^4$ ($W_{sphere} \propto r^6$). The results of the fit, giving p close to 3, indicate that a single hole scatters like a two dimensional system. We attribute the deviations of p from the expected value to the fact that the diameters used in the fit ($d < 0.2$) are not strictly in the limit of small-hole.

2.3.2 2D and 3D scattering

Next we report on the calculations of the power W_{3D} emitted outside the slab by the scattering hole. For this we integrate the z component of the time-averaged Poynting vector $\vec{S}'$ on a surface in proximity of the slab and parallel to the interface (see Appendix 2.A for more details). From W_{3D} we obtain the scattering efficiency Q_{3D} using Eq. (2.2).

Figure 2.5 reports the relative strength Q_{3D}/Q_{2D} of the 3D scattering

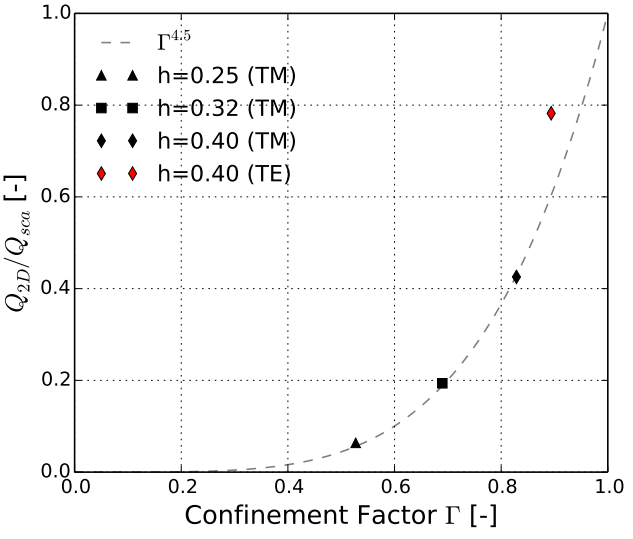

Figure 2.4: The ratio of Q_{2D} and the scattering efficiency of Mie cylinder Q_{sca} for different confinement factors (see text). The dashed line $\Gamma^{4.5}$ is an empirical fit added to guide the eye.

Table 2.1: Fit parameters of Q_{2D} shown in Fig. 2.3. p is the exponent of the polynomial dependence of the 2D scattering efficiency from the diameter of the hole (see Eq. (2.4)). Γ is the confinement factor for the slab mode defined in Eq. (2.3).

	h=0.25 (TM)	h=0.32 (TM)	h=0.40 (TM)	h=0.40 (TE)
p	2.65±0.17	2.74±0.05	2.65±0.06	2.51±0.07
Γ	0.53	0.69	0.83	0.89
R_Q^μ	0.06	0.19	0.43	0.78

process with respect to the 2D scattering process showing that the ratio of the two scattering efficiencies decreases with increasing thickness of the slab. This is expected as the guided light is more confined in a thicker membrane, and as a consequence less field is present at the facets of the cylinder and scattered in 3D. The values for the ratios Q_{3D}/Q_{2D} are relatively constant over the simulated hole diameters, with some variations in the range of hole sizes we investigate. These variations are not expected in the approximation where the hole scatters like a point dipole in the center of the slab [28] and are a first indication that our scattering system might be more complicated than expected.

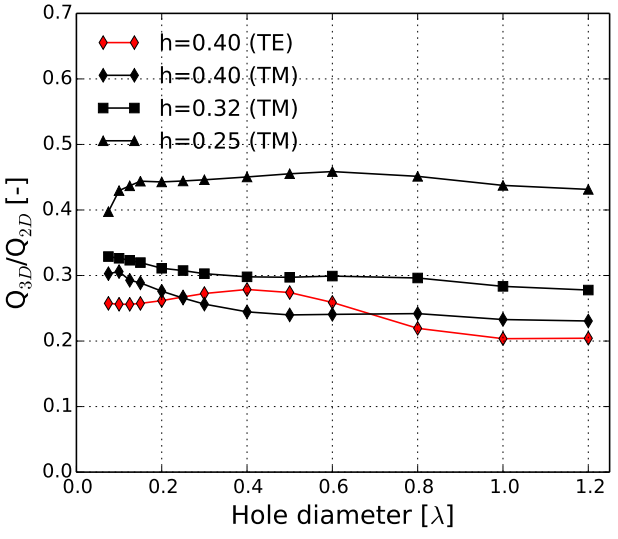

Figure 2.5: Ratio Q_{3D}/Q_{2D}, quantifying the scattering losses out of the slab relative to the scattering into slab modes, as function of the hole diameter d. Results are reported for the TM mode for $h = 0.40, 0.32, 0.25$ and for the TE mode for a slab thickness of $h = 0.40$.

We also simulate scattering from a single hole in slabs of higher refractive index for slab thickness h $= 0.25, 0.4$. The results show that for $n_2 = 3.4$ (typical of GaAs) the ratio of Q_{3D}/Q_{2D} decreases considerably to values $Q_{3D}/Q_{2D} \simeq 0.1$ for $h = 0.25$ and $Q_{3D}/Q_{2D} \simeq 0.03$ for $h = 0.4$, which is a factor 5 to 10 smaller than the ratio shown in Fig. 2.5. This is expected, as the largest refractive index will promote optical emission into the slab and reduce the relative emission to outside modes. We will not discuss these results any further, as they were obtained for thickness where the high-index slab supports multiple guided modes. The simulations for thinner slabs of high-index material proved to be too demanding for now.

2.3.3 Angular dependence of the 2D scattering

In the previous sections we have considered the total scattering cross section for the 2D and 3D scattering process. We now examine the angular properties of the 2D scattering, i.e. the differential scattering cross section $\sigma'(\theta) = d\sigma/d\Omega(\theta)$, with θ the scattering angle between the propagation direction of incident and scattered fields.

We calculate the intensity $I_s(\theta)$ scattered in the slab at a specific

angle and derive the normalized differential scattering cross section as $\hat{\sigma}'(\theta) = I_s(\theta)/\max(I_s(\theta))$. This allows to compare directly the angular dependence of the scattering function for holes of different diameters. We use the infinite Mie cylinder as reference, applying the same normalization to its scattering cross sections.

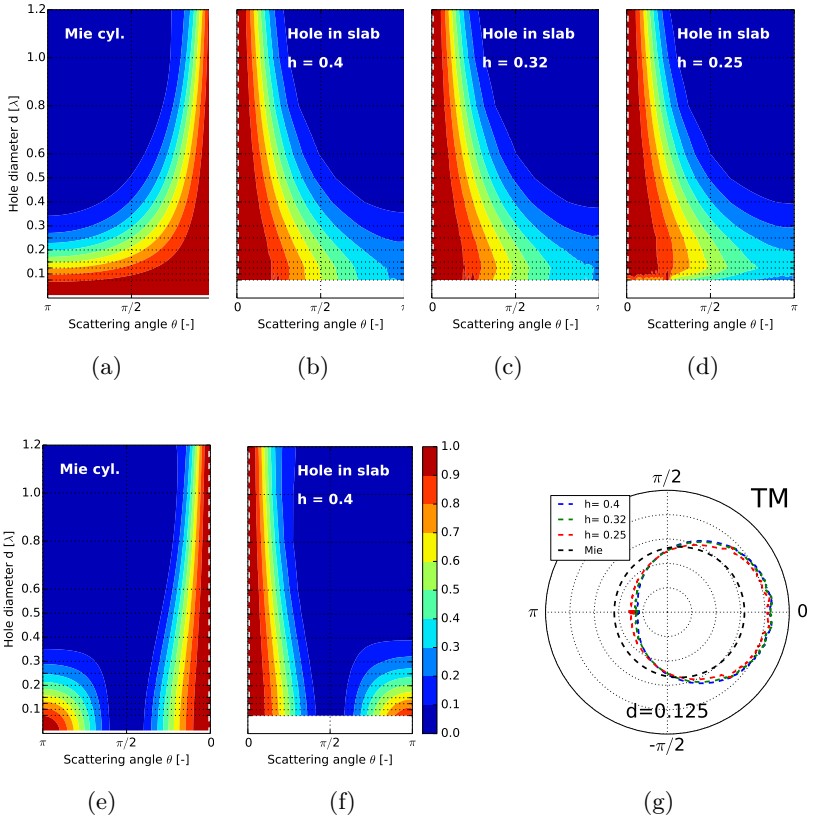

Figure 2.6: Normalized differential scattering cross sections $\sigma'(\theta)$ for TM (a-d) and TE (e-f) polarization, for Mie cylinders (a, e) and holes in slabs with $n_2 = 1.5$ and thickness h. The differential scattering cross section are all normalized to 1 and the colorscale defines ten bands for values from 0 to 1. The grid for the vertical axis indicates the values of hole diameters used in the simulations. $E_z(z = 0)$ for $h = 0.4$, $d = 0.1$ in TM case is shown in Fig. 2.2. In g) we report in polar coordinates the normalized differential scattering cross sections for holes of the same diameter $d = 0.125$ and slabs of three different thickness for TM polarization. The scattering in the slab geometries is more directional as compared to the corresponding Mie cylinder.

Figure 2.6 resumes the findings from the previously discussed simulations. We report on the left side the expected normalized $\sigma'(\theta)$ for a Mie cylinder and on the right the results for single holes in slabs of different thickness. In the TE case the scattered intensity shows two lobes centred around $\theta = 0, \pi$, as one would expect for a dipole oriented in the plane of the slab. We notice a striking difference in TM polarization between the angular scattering of a 2D Mie cylinder and a single hole. For Mie cylinders the normalized $\sigma'(\theta)$ tends to a constant value for $r \ll \lambda$, as expected for the dipole limit in the Rayleigh regime. Instead, for holes in confined geometry $\sigma'(\theta)$ shows a different behaviour, with more forward scattering in the limit of small holes. This surprising results indicates that the hole in a slab is more complex than a simple electric dipole with polarizability proportional to the hole volume. We speculate that the calculated reduced back scattering could originate from a more complicated polarization profile around the hole than one might expect from a first Born approximation of the scattering problem.

2.4 Relevance in modelling 2D random media

Our results have consequences in the calculation of transport properties of two-dimensional random scattering media. The cross sections we calculate for the single hole have direct equivalents for an infinite cylinder: σ_{2D} maps onto the scattering cross section σ_{sca} of the cylinder, whilst our σ_{3D} acts as an effective absorption cross section σ_{abs}, such that the total extinction cross section is $\sigma_{ext} = \sigma_{sca} + \sigma_{abs} = \sigma_{2D} + \sigma_{3D}$.

We suggest that it is possible to use 2D FDTD calculation to approximate the scattering of holes in a slab provided that two effects are accounted for. First, the scattering cross section calculated for Mie cylinder should be reduced by a factor R_Q^μ by rescaling the hole size to a diameter d_r, such that $\sigma_{sca}(d_r) = R_Q^\mu(h)\sigma_{sca}(d)$, where we indicate the dependence of R_Q^μ from the slab thickness which can be calculated with a single full 3D FDTD simulation. Secondly, an absorption cross section must be introduced to account for the out of plane losses. This can be achieved by adding an imaginary component to the refractive index of the material filling the hole $n_r = n_1 + in'$ such that $\sigma_{abs}(d_r, n_r) = \left(\frac{Q_{3D}}{Q_{2D}}\right)(h)\ \sigma_{sca}(d_r)$. The value of n' can be found numerically using analytical theory for Mie scattering. The proposed transformations are intended as approximations hinging on the assumption that a plane wavefront excites the hole. They offer the advantage that holes in a slab of thickness h

can be modelled with one full 3D FDTD simulation and calculations based on Mie scattering. These considerations also apply to the description of scattering in disordered 2D photonic crystal lattices [9].

To calculate the macroscopic transport properties of a 2D scattering medium we need to relate them to the microscopic scattering properties of the single hole. The scattering mean free path ℓ_{sca} can be calculated as $\ell_{sca}^{-1} = \rho\sigma_{sca}$ [9], with ρ the density of scatterers per unit surface. This expression is only valid for isotropic scattering; for anisotropic scattering $\sigma'(\theta)$ is weighted by a factor $(1 - \cos(\theta))$, with θ the usual scattering angle [18]. The inclusion of this correction for our smallest holes to account for the dominant forward scattering gives, for h=0.4, a mean free path 1.3 times longer than for the Mie case.

2.5 Conclusions

In conclusion, we numerically investigate the scattering of light from a hole in a dielectric slab of varying thickness (single-mode) with full 3D FDTD simulations. We find that the 2D scattering process dominates over the 3D radiative losses, and that the relative losses Q_{3D}/Q_{2D} are smaller when the mode is more confined in the waveguide, varying only slightly with hole size. We confirm that the scattering from a hole in a single-mode slab is a two dimensional process, like for an infinite Mie cylinder. Scattering from a hole in a slab differs from Mie scattering for a reduced scattering cross section, effective losses originating from 3D scattering and an unexpected directionality.

By studying the angular dependence of the 2D scattering we also find that, in TM polarization, the hole scatters light predominantly to the forward direction also in the limit of small holes, whereas the dipole approximation predicts a uniform radiation pattern in the slab plane. We thus conclude that a dipole model is insufficient to describe the scattering for small holes in a confined geometry.

Finally, we translate our observations in the consequences they have for the modelling of scattering in 2D random media. Apart from the necessity to include loss in these models, both the reduced scattering efficiency and altered angular dependence of the scattering lead to an effective increase of the scattering mean free path. We suggest a transformation for size and optical properties of the hole allowing, with only one full 3D FDTD simulation, to perform computationally lighter calculations on 2D random structures.

2.A FDTD simulations

The 3D cubic simulation cell used for this work is depicted in Fig. 2.2; it has a side length of 8λ and a grid density of 40 points/λ along each direction. The cell is surrounded by perfect matching layers of thickness 1λ on each side, for a final 3D cell of $(400)^3$ points. Simulations were performed with the FDTD software MEEP on CPU Intel Xeon E5 2603 1.8GHz $\times$ 4, 64 GB of RAM, for a calculation time of approximately one hour for each combination of slab thickness and hole size.

In our simulations the TM mode is excited in the slab with a line-dipole source oriented parallel to the y axis in the symmetry plane of the slab (see Fig. 2.2). This allows us to generate a flat wavefront propagating with in plane wavevector along x. The thickness of the slab is chosen such that only one mode is supported for each polarization. The simulations are run for a number of cycles sufficient for the scattered field to reach the edges of the simulation cell.

The scattered field $\vec{E}_S$ is calculated by complex field subtraction $\vec{E}_S = \vec{E}_T - \vec{E}_I$, where $\vec{E}_T$ is the total field in the presence of the scatterer and $\vec{E}_I$ the total field in absence of a hole. A similar relation applies to the scattered magnetic field $\vec{H}_S$. To calculate the scattering efficiencies we calculate the time averaged energy flux obtained from the real part of Poynting vector $\vec{S}' = \frac{1}{2}\mathrm{Re}\left(\vec{E}_S \times \vec{H}_S^*\right)$.

We obtain the total in-plane scattered intensity by integrating the radial component of $\vec{S}'$ over a cylindrical belt of radius $\tilde{R} = 2\lambda$ and total height of 2λ, which is large enough to contain the full guided mode. The power scattered in the radiative modes is in turn obtained by integrating the component of $\vec{S}'$ normal to the slab over a square centred in the origin, with side 7λ and in close proximity with the slab interface.

The convergence of the simulations was checked by comparison with Mie theory in the case of a long cylindrical air holes in glass, for different radii, and under the excitation of a plane wave created by a two dimensional dipolar source. This simulations showed almost perfect agreement with calculations based on theory. Mie scattering calculations were performed using scripts based on the code available from Bohren-Huffman [22].

2.B Results for higher index contrast (GaAs)

Optical waveguides generally used in real photonic application are obtained out of semiconductors like Si, Si_3N_4 or GaAs for wavelengths in the infrared. These materials have a higher refractive index than glass (with $n \simeq 1.5$), as for instance GaAs with $n_{GaAs} \simeq 3.4$. To explore the scattering properties for a single hole in a situation with a higher refractive index contrast, we also performed simulations for a slab of refractive index $n_2 = 3.4$ in air, comparable to a free standing GaAs membrane. The values for the thickness of the membrane have a lower limit imposed by the grid resolution; the values we used for h determine a waveguide able to support more than one mode. The results in this conditions are more complicated to interpret and hence we only present them in this appendix. In Fig. 2.7 we report the fractional losses Q_{3D}/Q_{2D}; and we note that the obtained values around 3% or lower are much smaller than for the same thicknesses in the case of $n_2 = 1.5$. This is a consequence of the higher index contrast and consequent increased confinement of the field.

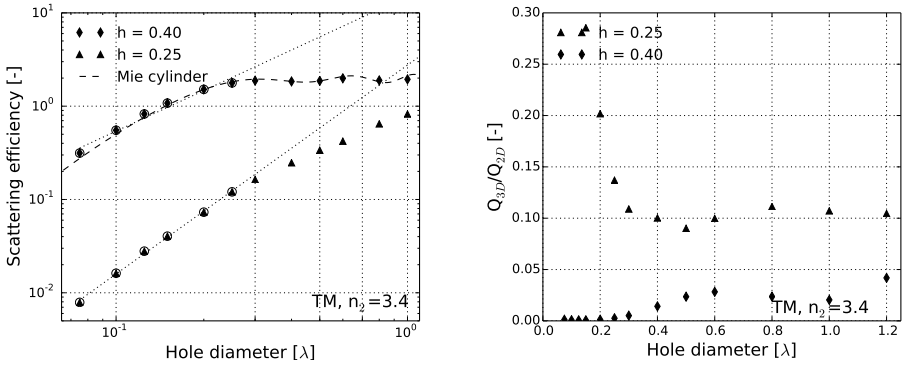

(a) (b)

Figure 2.7: Calculated scattering efficiencies Q_{2D} (left) and fractional loss Q_{3D}/Q_{2D} (right) for the TM_0 mode as function of the diameter of the hole, for a slab refractive index of n_2=3.4 and thickness h=0.25 and 0.4, both in the multi mode regime. Linear fit for datapoints with $d \leq 0.2\lambda$ (circled in the plot) is added in dotted line to highlight the polynomial dependence in the small particle regime. For comparison in dashed line the scattering efficiency of an infinitely long Mie cylinder.

In Fig. 2.8 we show the angular dependence of scattering from a hole in a high index slab. This appears to deviate from the simple dipolar prediction even more than for the case with $n_2 = 1.5$.

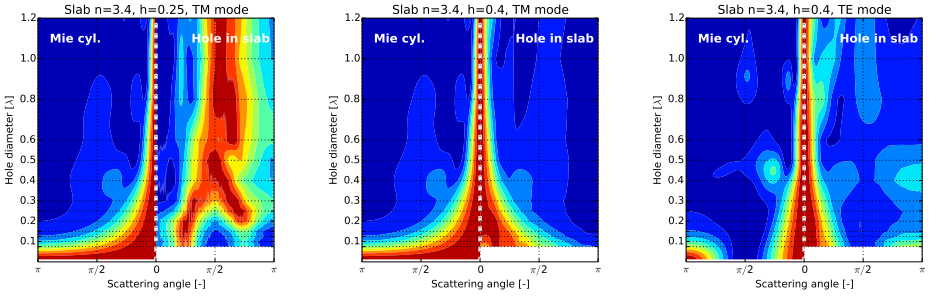

(a) TM, h=0.25 (b) TM, h=0.40 (c) TE, h=0.40

Figure 2.8: Angular dependence of the scattering from single hole in slabs with $n_2 = 3.4$ (GaAs) and different thicknesses. (a) h=0.25, TM case; (b) h=0.4, TM case; (c) h=0.4, TE case. Left side of the plots: normalized differential scattering cross sections of Mie cylinder. Right side of the plots: differential scattering cross sections calculated from FDTD simulations normalized to 1 for each hole diameter. The colorscale defines ten bands for values from 0 to 1. The grid for the vertical axis indicates the values of hole diameters used in the simulations.

Bibliography

[1] S. McNab, N. Moll, and Y. Vlasov, *Ultra-low loss photonic integrated circuit with membrane-type photonic crystal waveguides*, Opt. Express **11**, 2927 (2003).

[2] J. L. O'Brien, A. Furusawa, and J. Vučković, *Photonic quantum technologies*, Nat Photon **3**, 687 (2009).

[3] K. H. Madsen *et al.*, *Efficient out-coupling of high-purity single photons from a coherent quantum dot in a photonic-crystal cavity*, Phys. Rev. B **90**, 155303 (2014).

[4] J. D. Joannopoulos, P. R. Villeneuve, and S. Fan, *Photonic crystals: putting a new twist on light*, Nature **386**, 143 (1997).

[5] E. Yablonovitch, *Photonic band-gap structures*, J. Opt. Soc. Am. B **10**, 283 (1993).

[6] R. D. Meade, K. D. Brommer, A. M. Rappe, and J. D. Joannopoulos, *Existence of a photonic band gap in two dimensions*, Applied Physics Letters **61**, 495 (1992).

[7] S. G. Johnson, P. R. Villeneuve, S. Fan, and J. D. Joannopoulos, *Linear waveguides in photonic-crystal slabs*, Phys. Rev. B **62**, 8212 (2000).

[8] C. Bonato *et al.*, *Far-field emission profiles from L3 photonic crystal cavity modes*, Photonics and Nanostructures - Fundamentals and Applications **11**, 37 (2013).

[9] A. F. Koenderink, A. Lagendijk, and W. L. Vos, *Optical extinction due to intrinsic structural variations of photonic crystals*, Phys. Rev. B **72**, 153102 (2005).

[10] S. G. Johnson *et al.*, *Roughness losses and volume-current methods in photonic-crystal waveguides*, Appl. Phys. B **81**, 283 (2005).

[11] W. Bogaerts, P. Bienstman, and R. Baets, *Scattering at sidewall roughness in photonic crystal slabs*, Opt. Lett. **28**, 689 (2003).

[12] W. Bogaerts *et al.*, *Out-of-plane scattering in 1-D photonic crystal slabs*, Optical and Quantum Electronics **34**, 195 (2002).

[13] H. Zhang *et al.*, *Effective medium theory for two-dimensional random media composed of core-shell cylinders*, Optics Communications **306**, 9 (2013).

[14] A. Kirchner, K. Busch, and C. M. Soukoulis, *Transport properties of random arrays of dielectric cylinders*, Phys. Rev. B **57**, 277 (1998).

[15] L. Labonté, C. Vanneste, and P. Sebbah, *Localized mode hybridization by fine tuning of two-dimensional random media*, Opt. Lett. **37**, 1946 (2012).

[16] S. Boscolo and M. Midrio, *Three-Dimensional Multiple-Scattering Technique for the Analysis of Photonic-Crystal Slabs*, J. Lightwave Technol. **22**, 2778 (2004).

[17] H. Benisty *et al.*, *Radiation losses of waveguide-based two-dimensional photonic crystals: Positive role of the substrate*, Applied Physics Letters **76**, 532 (2000).

[18] G. M. Conley *et al.*, *Light Transport and Localization in Two-Dimensional Correlated Disorder*, Phys. Rev. Lett. **112**, 143901 (2014).

[19] S. F. Liew *et al.*, *Transmission channels for light in absorbing random media: From diffusive to ballistic-like transport*, Phys. Rev. B **89**, 224202 (2014).

[20] K. Vynck, M. Burresi, F. Riboli, and D. S. Wiersma, *Photon management in two-dimensional disordered media*, Nat Mater **11**, 1017 (2012).

[21] J. D. Jackson, *Classical Electrodynamics* (Wiley) (2007).

[22] C. F. Bohren and D. R. Huffman, *Absorption and scattering of light by small particles*, 10 ed. (Wiley) (1983).

[23] J. Venermo and A. Sihvola, *Dielectric polarizability of circular cylinder*, Journal of Electrostatics **63**, 101 (2005).

[24] R. Ruppin, *Electromagnetic scattering from finite dielectric cylinders*, J. Phys. D: Appl. Phys. **23**, 757 (1990).

[25] A. V. Shchegrov, I. V. Novikov, and A. A. Maradudin, *Scattering of Surface Plasmon Polaritons by a Circularly Symmetric Surface Defect*, Phys. Rev. Lett. **78**, 4269 (1997).

[26] A. Taflove, *Computational Electrodynamics: The Finite-difference Time-domain Method* (Artech House) (1995).

[27] A. F. Oskooi *et al.*, *Meep: A flexible free-software package for electromagnetic simulations by the FDTD method*, Computer Physics Communications **181**, 687 (2010).

[28] H. P. Urbach and G. Rikken, *Spontaneous emission from a dielectric slab*, Physical Review A **57**, 3913 (1998).

Angle resolved transmission through sparse metal hole arrays

We present the first angle resolved measurements of extraordinary optical transmission (EOT) through hole array gratings in a gold film. Varying the lattice spacing of the arrays and looking at higher diffraction orders, we retrieve the angular emission pattern of the constituent holes with better signal to noise ratio than with single-hole experiments. We present a method to determine separately the angular dependence of the direct and resonant contribution to EOT by using the spectral features of the diffraction orders together with an established model. The comparison of our results with the known angular transmission of a single hole in a metal film yields a good agreement for s-polarized light. Deviations are found for illumination with p-polarized light and we address the discrepancy with Coupled Mode Model calculations and Finite Difference Time Domain simulations. These measured deviations are currently not fully understood.

This chapter is published as:
F. Mariani, F. de León-Pérez, K. J. A. Vendel, L. Martín-Moreno, and M. P. van Exter, Optics Express **25**, 9061 (2017)

3.1 Introduction

Metal nano-structures can strongly localize optical fields in a charge-field coupled oscillation at the metal-dielectric interface, or surface plasmon (SP). These surface waves are important in several applied fields like photonic devices [1], biosensing [2] or solar cells [3]. The shape of nano-structure defines the character of the SPs, which can be either a resonance localized on nanoparticles [4] or distributed on periodic structures [5].

Nano-holes arrays are a well known class of periodic structures since the discovery of Extraordinary Optical Transmission (EOT) on metal hole gratings [6], an intriguing effect emerging from the collective action of many holes in a lattice structure. Extensive studies were conducted to understand how this phenomeon depends on the material [7], size [8, 9] and shape [10] of the holes and how surface waves propagate and couple to contribute to the spectral features of EOT [11, 12]. The physical picture of EOT is based on transmission of the electromagnetic field through nanoholes aided by resonant surface waves of the patterned structure[13]. These waves can be understood, in metal films, from the multiple scattering of SPs on holes at the flat interfaces; plasmons play the biggest role [14], together with the so called quasi-cylindrical wave (QCW) [15, 16, 17, 18].

Transmission studies on metal hole arrays are generally performed in collinear transmission geometry as the typically used structures have square symmetry with lattice constant which only allows one diffraction order at the wavelength of study. We use here metal hole arrays with a rectangular unit cell, one lattice constant being an integer multiple of a fixed spacing used in the orthogonal direction (see inset of Fig. 3.1(a)). An increasing number of diffraction orders appears for increasing lattice constant and this makes it possible to give a first description of the angular emission properties of EOT in the full scattering plane, by angularly resolving the diffraction orders in transmission.

The information we obtain allows to reconstruct the angular emission profile of a single hole. The scattering properties of single holes in metal have been measured and modelled for excitations from plane waves [19, 20], looking at the angularly resolved transmission. We now show how from transmission measurements of rectangular arrays of holes it is possible to separate the contribution of excitation from plane waves and SPs, employing an established model for EOT. The resulting signal-to-noise ratio in our experiment is better

than in experiments on single holes since more holes contribute to transmission and the intensity is concentrated in well defined directions by interference. In our study we find a polarization dependent deviation of the angular emission profile as compared to existing theory for diffraction from single holes in metal. We report it here and speculate on the possible cause of this unexpected behaviour.

3.2 Hole arrays and setup

Our hole arrays are obtained on a 170 nm thick gold layer, evaporated on a substrate of BK7 glass ($n_d = 1.51$) and are capped by a 20 nm chromium layer to quench SPs at the gold-air interface. The holes, produced with standard e-beam lithography and lift-off techniques, have a diameter of 165 nm and are arranged in chains with a fixed lattice constant $a_0 = 450$ nm. A two-dimensional rectangular hole array is constructed from multiple chains repeated parallel to each other at a spacing of qa_0, with the spacing factor $q = 1 - 14$ identifying each array (see inset in Fig. 3.1(a) for q=2). All the final arrays have the size of a square with side of 400 μm.

The experimental setup is shown in Fig. 3.1(a). We illuminate the sample at normal incidence with a white light source (Energetique LDLS EQ-99) coupled via a multimode fiber (diameter 200 μm) imaged on the sample in a spot of 300 μm diameter. The angle resolved transmission $T(\lambda, \theta)$ of the hole arrays is collected using a computer controlled goniometric stage rotating in the xz plane. The detection optics is mounted on this stage and consists of two lenses in 4f-configuration, imaging a second multimode fiber (diameter 400 μm) on the sample in a spot as large as 1.2 mm; this magnification is chosen to make the setup less sensitive to misalignments during angular scans. The collected light is spectrally analyzed with a fiber-coupled spectrometer (Ocean-Optics USB2000). Polarization resolved measurements are made possible by two polarizers placed in both excitation and detection arms. Hole arrays are always oriented with hole chains along the $\hat{y}$ axis, as shown in the inset of Fig. 3.1(a). We define the scattering angle θ as the angle with the surface normal (see Fig. 3.1(a)) and the p(s)-polarization of the light for the E field oriented along $\hat{x}(\hat{y})$.

The excitation light has a numerical aperture $\mathrm{NA}_{in} = 0.01$; this is small enough to ensure the spatial coherence required in our experiment, but large enough for the total intensity not to be reduced by diffraction. The excitation

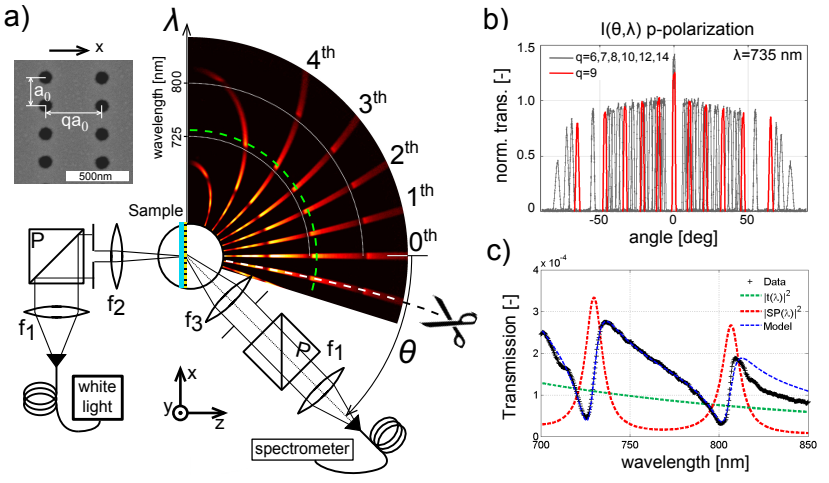

Figure 3.1: (a) The goniometric setup used in the experiments. The sample is illuminated at normal incidence ($\mathrm{NA}_{in} = 0.01$) with a fiber-coupled white-light source. A second telescope ($\mathrm{NA}_{out} = 0.03$) scans, on a rotating stage, a semi-circle in the xz plane and collects the transmitted light at scattering angle θ. Focal lengths are $f_1 = 50$ mm, $f_2 = 75$ mm, $f_3 = 150$ mm. Polarizers allow polarization-resolved study of the transmission. The false color plot reports the transmitted intensity $I(\theta, \lambda)$ for the $q = 9$ array. The inset shows a detail of SEM image of sample with $q = 2$. (b) Cross-cuts of $I(\theta, \lambda)$ at fixed $\lambda = 735$ nm, i.e. along the green dashed arc indicated in a), for all the measured q spacings. (c) Transmission spectrum for the 1^{st} diffraction order of the $9a_0$ array extracted along the white dashed line in a). The data are fitted with the model in Eq. (3.1). From the calculated parameters it is possible to separate the direct transmission $|t|^2$ (green dotted lines) and the resonant contribution $|SP|^2 = \left|s/(u^{-1} - \sigma)\right|^2$ (red dotted lines).

NA also defines the angular width of the diffraction orders. The collection optics has $\mathrm{NA}_{out} = 0.03$, defining an acceptance angle wider than the angular width of the excitation.

3.3 Theoretical model of spectral and angular transmission

With the purpose of experimentally studying the angular dependence of EOT, we use analytical models to interpret both the spectral and angular degrees of freedom of our transmission measurements. We compare our results with existing theories, confirmed by experiments, for the EOT spectra and for the optical diffraction from small holes on metal films.

For the spectral response we use the model presented in [14] which explains the Fano shape of the resonances in the EOT transmission spectrum $T(\lambda)$. This model applies to the case of normal illumination and for polariza-

tion parallel to one of the lattice axes. In the model the array is considered as a one-dimensional grating of chains of holes. The incident light has two effects: a fraction of it is directly transmitted through the holes (non-resonant contribution) and part of it excites SPs propagating over the metal-dielectric interface in the direction of the incident light polarization. The latter scatter at the hole chains, being partially transmitted and reflected, and a SPs resonant field builds up, similarly as in a distributed Fabry-Perot cavity. The SPs field partially leaks through the holes and contributes to the transmission. We indicate with $t(\lambda)$ the transmission amplitude of the non-resonant field, and with $s(\lambda)/(u^{-1}(q) - \sigma)$ the transmission amplitude originating from the resonant SPs field. The expression at the denominator accounts for the multiple roundtrips of SPs over the array and includes a SP-SP scattering coefficient $\sigma \leq 1$ and the phase delay and amplitude loss $u(q) = \exp(ik_{spp}qa_0)$ due to the SPs propagation over the distance between two chains; in particular the function $u(q)$ defines the position of the resonances. The two transmission amplitudes interfere and add up coherently, yielding the intensity transmission spectrum [18]:

$$T(q, \lambda) = q^{-2} \left| t(\lambda) + \frac{s(\lambda)}{u^{-1}(q) - \sigma} \right|^2 \tag{3.1}$$

The pre-factor q^{-2} gives the scaling of the transmission intensity on the holes surface density. We take $t(\lambda)$ real valued and dependent on wavelength as $t(\lambda) \propto \lambda^{-2}$ and $s(\lambda)$ complex valued and proportional to λ^{-4}. This choice for the dependence on wavelength is supported by previous works [19, 5, 14]. We refer the reader to [14] for additional details.

The model in Eq. (3.1) has been used in an experimental study on EOT at 0^{th} diffraction order [18] (our coefficient $s(\lambda)$ is equivalent to the product $2\alpha\beta$ in the original publication). We will extend it to higher diffraction orders by introducing an angular dependence for the coefficients $t(\lambda)$ and $s(\lambda)$; these separately describe the angular emission properties of a single hole chain under the excitation of, respectively, an incident light wave or by a SP wave. As these are two physically distinct excitations, they can in principle manifest different angular emission profiles.

The angular response of an array of coherent emitters can be written as the product of two factors: (i) the structure factor $S(\theta)$ of the hole array (interference) and (ii) the form factor of the individual emitters (diffraction) which in our case are single nano-holes. The structure factor is peaked at the reciprocal lattice sites, as an excitation of wavevector $\vec{k}_{in}$ will only scatter in

directions given by $\vec{k}_{out} = \vec{k}_{in} + \vec{G}$, with $\vec{G}$ a vector of the reciprocal lattice [5]. For the transmission form factor of an individual hole in metal we use an analytical theory developed in the framework of the Coupled Mode Method (CMM) [20] and based on expansion of the field in relevant optical modes. The solutions we use here apply to subwavelength holes, where the transmission is dominated by the fundamental mode TE_{11}. It yields the transmitted intensity from a single hole as function of angle $I_\pi(\theta)$, with θ the scattering angle and $\pi = p, s$ the polarization of the incident electric field. For holes with radius $r \ll \lambda$ the contributions from p and s waves to the normalized scattering cross-section, defined as the power radiated to the far-field per unit of solid angle, normalized to its value for $\theta = 0$ read [20]:

$$\frac{I_p(\theta)}{I_p(0)} = \frac{|1+z_s|^2\cos^2(\theta)}{|\cos(\theta)+z_s|^2}\frac{4{J_1}^2(\Phi)}{\Phi^2} \simeq \frac{|1+z_s|^2\cos^2(\theta)}{|\cos(\theta)+z_s|^2}\left(1-\frac{\Phi^2}{4}\right) \tag{3.2}$$

$$\begin{aligned}\frac{I_s(\theta)}{I_s(0)} = \frac{|1+z_s|^2\cos^2(\theta)}{|1+z_s\cos(\theta)|^2}\frac{4{J_1'}^2(\Phi)}{(1-\Phi^2/u^2)^2} \simeq \\ \frac{|1+z_s|^2\cos^2(\theta)}{|1+z_s\cos(\theta)|^2}\left(1-\left(\frac{3}{4}-\frac{2}{u^2}\right)\Phi^2\right)\end{aligned} \tag{3.3}$$

where we define the ratio of the surface impedances $z_s = \sqrt{\epsilon_d}/\sqrt{\epsilon_{metal}}$, with ϵ_d and ϵ_{metal} permittivities respectively of the dielectric half space and the metal, and where $u \simeq 1.84$ is the first root of the Bessel function $J_1(u) = 0$ and $\Phi = kr\,\sin(\theta)$, with $k = 2\pi/\lambda$ and r the effective radius of the hole, also including field penetration depth in the metal.

The first terms in Eqs. (3.2)–(3.3) describe the angular emission of an infinitesimally small hole in a metal (dipole approximation). For a perfect conductor $\epsilon_{metal} \to -\infty$, the emission profile is that of a magnetic dipole with $I_p(\theta) \simeq 1$ and $I_s(\theta) \simeq \cos^2(\theta)$ [19]. The second term in the equations introduces a (Fraunhofer-like) correction accounting for the shape of the field inside the hole. The added Taylor expansions indicate the order of the correction for small values of Φ.

We have checked the applicability of Eqs. (3.2)–(3.3) by analyzing our system with the Coupled Mode Method (CMM) and by performing finite-difference time domain (FDTD) simulations. The CMM relies on a modal expansion of the EM fields, where the dielectric properties of the metal are approximately treated via the surface impedance boundary conditions [21]. Perfect electric conductor (PEC) boundary conditions have been used at the

lateral walls of the holes for the sake of analytical simplicity. Nevertheless, the real penetration of the field into the metallic walls is taken into account by enlarging the radius of the hole by 1.9δ, where $\delta = \lambda/\left[2\pi \mathrm{Im}(\sqrt{\epsilon_{metal}})\right]$ is the skin depth (an enlargement of 1.5-1.9δ improves the agreement with first principle calculations [20]). Numerical simulations using the CMM are in good agreement with both experimental results and rigorous calculations for the angular diffraction pattern of single holes [20] and the total transmission of hole arrays [22]. For sufficiently small hole diameters, the transmission process is controlled by the fundamental waveguide mode (TE_{11}) alone [22]. Here the dielectric constant of gold has been taken from the experimental data reported in [23].

To understand the energy distribution in the diffraction orders we recall that, for a hole array, the transmission angular intensity distribution is written as $I_\pi^{ARRAY}(\theta) = I_\pi(\theta)S(\theta)$. An array of N rows under uniform illumination has structure factor $S(\theta) = \sin^2(\alpha N \sin(\theta))/\left(N\sin(\alpha\sin(\theta))\right)^2$ with $\alpha = kn_d q a_0/2$. The angular positions of the diffraction maxima θ_m are obtained at the zeros of the denominator of $S(\theta)$, i.e. for $\alpha\sin(\theta_m) = m\pi$ (Bragg condition at normal incidence). A diffraction peak has a width $\Delta(\theta_m)$, which we approximate as half the distance between the two closest minima; these occur for $\alpha\sin(\theta) = (m \pm N^{-1})\pi$, giving $\Delta(\theta_m) \simeq \pi/(\alpha N\cos(\theta_m))$. The peak width increases with diffraction angle as $1/\cos(\theta_m)$ and consequently also the power emitted in each diffraction maxima $P_\pi(\theta_m) \approx I_\pi^{ARRAY}(\theta_m)\Delta(\theta_m)$ retains the factor $1/\cos(\theta_m)$ and scales accordingly.

3.4 Experimental results

We measured the transmission of the hole arrays on both the glass and the air side, with both p and s polarizations. Measurements with crossed polarizers show that no depolarization occurs in our system within experimental error. We don't show here results for the transmission on the glass side: the measured intensities in this case need to be corrected for Fresnel transmittance coefficients for passage of transmitted light through the glass-air interface, but most importantly total internal reflection (TIR) limits the accessible angular range to the critical angle $\theta_{TIR} = \arcsin(1/n_d) = 41.4°$ for transmission in the glass (for $n_d = 1.51$). This makes the experimental dataset incomplete and less useful when compared to the model in Eqs. (3.2)–(3.3).

The two main ways of studying the transmission function $T(\lambda, \theta)$ are indi-

cated by the two dashed curves in the false-color plot in Fig. 3.1(a). The first way is looking at $T(\lambda, \theta)$ at constant wavelength (dashed green semi-circle); the angular response of the system results in multiple peaks corresponding to the different diffraction orders, as shown in Fig. 3.1(b) for different values of the spacing factor q. Diffraction orders for different lattice constant spacings are located at different angular positions, thus providing an angular sampling of the transmission. From Fig. 3.1(b) one notices an excess of measured intensity for the diffraction order at $\theta = 0$: this is caused by light transmitted through the metal film, as also confirmed from FDTD calculations. In order to correctly compare different arrays, we normalize $T(\lambda, \theta)$ by $T(\lambda, 0)$ but by the average value for the $\pm 1^{st}$ orders.

The second way to study the transmission function is by cross-cutting it along the m^{th} diffraction order using the Bragg condition at normal incidence $\sin(\theta_m(\lambda)) = m\lambda/(qa_0)$, as indicated in Fig. 3.1(a) in white dashed line. This highlights the spectral response of the array, which contains characteristic Fano-type resonance peaks of EOT [14], as shown in Fig. 3.1(c).

p-polarization. When illuminating the array with p-polarized light the resulting SPs mainly propagate along $\hat{x}$, being this the direction of the electric field. A resonance is obtained for the optical frequency that satisfies the condition $q\lambda_{SP} = qa_0$, with λ_{SP} the SP wavelength at the metal-glass interface. This is the SP resonance we focus on in this work, shown in Fig. 3.1(c). It is centred at $\lambda \simeq 726$ nm and its spectral position is almost independent on the value of q. The additional resonance at longer wavelengths satisfies instead the condition $(q-1)\lambda_{SP} = qa_0$ and its position is red-shifted with increasing q.

We analyse the transmission spectra of each diffraction order using the model in Eq. (3.1), in a wavelength interval around 726 nm that includes the steep edges of the neighbouring resonances. For faster convergence we fix the value of σ, which quantifies the effect of SP scattering and only depends on the size of the hole, to an averaged value obtained when fits are run with it as a free parameter. An example of the results of the fits is included in Fig. 3.1(c) with separate plots for the direct and the resonant contributions; we note that the transmission spectra only show SPs resonances at the metal-glass interface. Resonant contributions from SPs at Cr-air interface are not visible, as expected. The parameters interesting for our study are the calculated fit parameters $t(\theta)$ and $s(\theta)$ which we normalize, for each array, by their values for the 1^{st} diffraction order. We report the result in Fig. 3.2 for all measured

diffraction orders of a set arrays of different spacing.

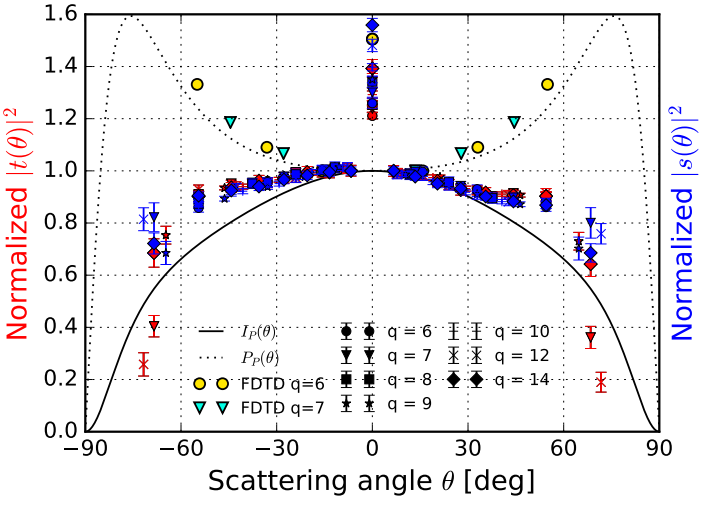

Figure 3.2: Angular dependence of the parameters $|t(\theta)|^2$ (red symbols) and $|s(\theta)|^2$ (blue symbols), derived by fitting the model in Eq. (3.1) to the transmission diffraction orders measured for p-polarization on the air side of hole-arrays. Data from different arrays are normalized to the value for first orders; note the excellent consistency of parameters from arrays of different q-values. The excess intensity at $\theta = 0$ is due to incomplete absorption of light passing through the gold film. We report for comparison $I_p(\theta)$ curve from Eq. (3.2) in solid line and, in dotted line, the curve including the correction with factor $\cos(\theta)^{-1}$ computed in Sec. 3.3 and discussed in Sec. 3.5. The latter is in excellent agreement with FDTD calculations, shown with yellow and cyan symbols, for the power in each diffraction order.

Two important observations can be done on Fig. 3.2. First, all the normalized values of the fit parameters $|t(\theta)|^2$ and $|s(\theta)|^2$ obtained from different arrays are in excellent agreement and consistently show the same angle dependence. This confirms the adopted experimental method and the relevance of the obtained angular emission profile after the analysis with the EOT model. Second, the calculated data points for $|t(\theta)|^2$ and $|s(\theta)|^2$ are superimposed on each other. We thus find that the angular emission profile is the same for excitation by either resonant SPs or by direct non-resonant optical transmission through the holes. The two parameters are not superimposed at the largest scattering angles because the angle dispersion deforms the transmission curve for the longest wavelengths of the fitting interval, reducing agreement with the model.

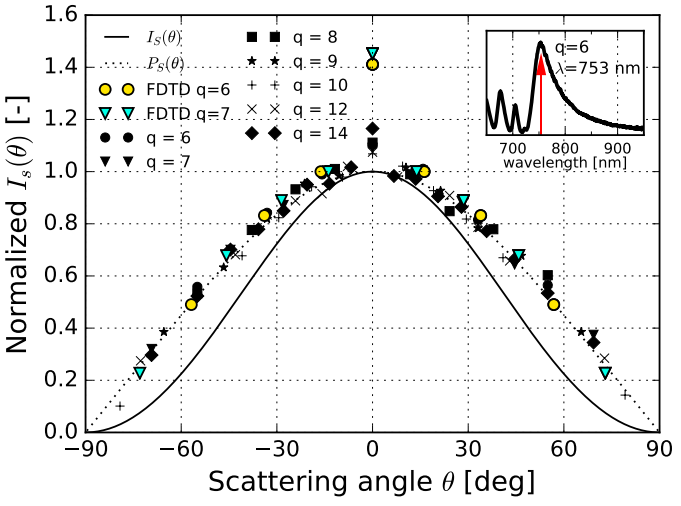

Figure 3.3: Peak values for the resonance in the transmission spectra at different diffraction orders obtained with illumination with s-polarized light (peak position around 750 nm, shown in the inset) for detection on the air side. The solid curve shows the single-hole diffraction obtained with Eq. (3.3), while the dotted curve shows this result after correction by a factor $\cos(\theta)^{-1}$ computed in Sec. 3.3 and discussed in Sec. 3.5.
The latter curve overlaps with both the experimental data, as expected, and with the results of FDTD calculations of the power in each diffraction order, shown with yellow and cyan symbols.

s-polarization. In Fig. 3.3 we report the normalized transmission data for s-polarization. Illumination with s-polarized light generates SPs waves propagating mainly along the $\hat{y}$ direction, i.e. along the chains. These SPs scatter frequently on holes belonging to the same chain and generate a distinct resonance, visible in the inset in Fig. 3.3. Holes belonging to the same chain are close enough for quasi-cylindrical waves to play a role in the hole-hole interaction [18], with possible effects on the transmission spectrum. The inset also shows additional resonances at shorter wavelengths very close to the main resonance, originating from SPs propagating at a small angle with respect to $\hat{y}$. These additional resonances make an analytical model more complicated in the case of s-polarization; we thus study the angular dependence of s-polarized light by taking the peak value of the transmission intensity. This is justified as the main resonance peak dominates the transmission spectrum.

3.5 Discussion

We explain the almost perfect match of the angular behaviour of the fit parameters $|t(\theta)|^2$ and $|s(\theta)|^2$ as follows: for detection on the air side both excitation sources, incident plane wave (direct transmission) and SP field on the glass side, first need to couple to the fundamental TE_{11} mode of the hole before being transmitted at the air side. As a result, the final angular behaviour is only dictated by the way the fundamental hole mode couples to the radiating modes on the detector side. This restriction applies also to the contribution of the quasi-cylindrical wave propagating on the glass side which is expected, at a specific wavelength, to show the same transmission angular dependence.

For a correct comparison of experiment and theory, we note that our setup measures an angular intensity integrated over the detection angle, i.e. an optical power $P(\theta)$. The width of each diffraction orders is determined by the excitation NA and increases with diffraction angle by a factor $1/\cos(\theta)$, as calculated in Sec. 3.3. For our geometry ($NA_{in} = 0.01$, $NA_{out} = 0.03$) diffraction maxima at $\theta < \arccos(NA_{out}/NA_{in}) \simeq 70^\circ$ are completely collected by the detection aperture; for higher scattering angles the detection optics partially crops the transmitted light and the measured optical power is slightly underestimated.

Measurements for s and p polarization show very different agreements to intensity and power curves calculated with single hole diffraction theory. For s-polarization, the experimental data shown in Fig. 3.3 perfectly overlap with the angular profile calculated for a single hole: while the angular dependence for $I_s(\theta)$ has an approximate $\cos^2(\theta)$ profile (dashed curve in Fig. 3.3), our data follow closely the optical power curve $P_s(\theta) \simeq \cos(\theta)$, also plotted in figure as dotted curve. At large angles we note that the expected underestimation of the power is barely noticeable. The good agreement between our measurements and the theoretical curves for the single-hole transmission indicates that we can reconstruct the scattering characteristics of a nano-hole by looking at the collective emission of a series of arrays.

The comparison with theory is not as good for measurements for p-polarization, as Fig. 3.2 shows. In this case the experimental data lie well below the expected curve for the power $P_p(\theta)$, while almost coinciding with the intensity curve $I_p(\theta)$ predicted by Eq. (3.2). The mild shoulders visible in the experimental data around $\theta = 60^\circ$ might still be a remnant of the huge

shoulders predicted for $P_p(\theta)$, which lie outside the figure and occur around $\theta \simeq 75^\circ$ at a value $P(\theta) \simeq 1.86$, but this is highly speculative. The observed discrepancy is not limited to this array: a similar angular profile for transmission in p-polarization was found for a previous sample with the same design but produced independently.

It must be stressed that the CMM expressions are in excellent agreement with full FDTD numerical calculations, but that the theoretical predictions for $p-$polarization also overestimate the radiation at large angles in the case of a *single* hole [20] with a diameter almost twice the one considered in this work. As the radiation in $p-$polarization is more sensitive to the characteristics of SPs, and thus to the properties of the surface, it would be interesting to estimate how the radiation depends on the modification of these properties. One

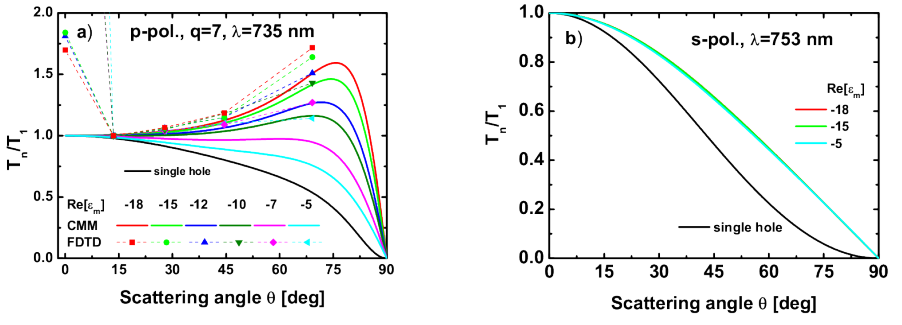

Figure 3.4: Distribution of the transmitted power as a function of angle for different values of Re(ϵ_m), calculated with both CMM model and FDTD; for the latter we show T_n/T_1, transmission per diffraction order normalized by the first diffraction order. Panel (a) is for p-polarization, while panel (b) renders the results for s-polarization.

possibility to explain the discrepancy is a Cr layer thicker than planned. However, our FDTD calculations show that the normalized transmittance remain virtually unchanged even when the thickness of the Cr layer is varied between the values of 5 nm and 25 nm (as a representative example, the intensity of the third order of the q=6 array is reduced by only 2%). Another possibility is that the presence of grains and/or crystal lattice defects in the metal reduces the absolute value of its dielectric constant. Eqs. (3.2)–(3.3) show that a reduction of $|\epsilon_{metal}|$ strongly reduces the p-polarized emission for larger angle with much smaller effects for the s-polarization. We have performed calculations of the radiation pattern as a function of the dielectric constant in the metal (see Fig. 3.4). These simulations show that, in order to reproduce

the experimental pattern, a value $Re(\epsilon_{metal}) \approx -5$ should be used instead of the expected value $Re(\epsilon_{metal}) = -18$. We find that this large modification of the parameters is unrealistic. Similarly, we have performed additional FDTD simulations in which we varied the geometrical parameters of the hole arrays. Some simulations yield a better agreement with the experimental data, but no realistic geometry gave a good fit of the observed anomalous angular profile. Hence, the radiation pattern for p-polarized light is not completely understood.

3.6 Conclusions

In this chapter we have presented the first measurements of the angle-resolved transmission of a set of hole array gratings. We extract the multiple diffraction orders and show how to separate the angular emission profiles of the holes under the excitation of either surface plasmons or normally incident light by applying a known model for extraordinary optical transmission, that we extend describing how to introduce the angular dependence of its coefficients. From the data for hole arrays of different lattice constant, we reconstruct the angular emission properties of a single hole. We compare the experimental results with numerical simulations and an analytical theory for the emission of individual nano-holes in a metal film. While our data for s-polarized excitation are in agreement with the emission profile expected for a single hole, for p-polarized excitation our experiment shows a different profile than theory predicts. We find as possible reason a change of the optical properties of the metal surface inside the hole. Nevertheless the values found for the dielectric constant are not fully satisfactory and an explanation for the observed angular emission requires further study.

We conclude with an outlook and a comment on the use of the EOT model in Eq. (3.1) for the separation of the angular emission properties of the holes subjected to both direct excitation and lateral SP polarization. The separation of the two emission mechanisms was not achievable in our experiment as the complete emission angle on the SP propagation side was not accessible due to total internal reflection at the glass substrate. A future extension of the experiment, with application of the method that we introduced, should thus be performed on SPs propagating at the air side in absence of chromium, or should allow for observation over a larger angular range on the glass side with the use, for instance, of solid immersion lenses. Furthermore, the excitation

of the array at $\theta_{in} \neq 0$ will prevent symmetry from removing interesting contributions to emission via destructive interference of fields from counter propagating SPs.

Acknowledgments

The CMM and FDTD calculations shown in Fig. 3.4 were performed by F. de León-Pérez. FM and MvE are grateful to prof. Eric Eliel and prof. Gert 't Hooft for fruitful discussion and to the AMOLF Institute (Amsterdam) and Dimitry Lamers for support provided in the sample fabrication.

Bibliography

[1] W. L. Barnes, A. Dereux, and T. W. Ebbesen, *Surface Plasmon Subwavelength Optics*, Nature **424**, 824 (2003).

[2] A. A. Yanik *et al.*, *An Optofluidic Nanoplasmonic Biosensor for Direct Detection of Live Viruses from Biological Media*, Nano Letters **10**, 4962 (2010).

[3] H. A. Atwater and A. Polman, *Plasmonics for Improved Photovoltaic Devices*, Nature Materials **9**, 205 (2010).

[4] P. Zijlstra and M. Orrit, *Single Metal Nanoparticles: Optical Detection, Spectroscopy and Applications*, Reports on Progress in Physics **74**, 106401 (2011).

[5] F. J. Garcia-Vidal, L. Martin-Moreno, T. W. Ebbesen, and L. Kuipers, *Light Passing through Subwavelength Apertures*, Reviews of Modern Physics **82**, 729 (2010).

[6] T. W. Ebbesen *et al.*, *Extraordinary Optical Transmission through Sub-Wavelength Hole Arrays*, Nature **391**, 667 (1998).

[7] D. E. Grupp *et al.*, *Crucial Role of Metal Surface in Enhanced Transmission through Subwavelength Apertures*, Applied Physics Letters **77**, 1569 (2000).

[8] A. Degiron, H. J. Lezec, W. L. Barnes, and T. W. Ebbesen, *Effects of Hole Depth on Enhanced Light Transmission through Subwavelength Hole Arrays*, Applied Physics Letters **81**, 4327 (2002).

[9] K. L. van der Molen, F. B. Segerink, N. F. van Hulst, and L. Kuipers, *Influence of Hole Size on the Extraordinary Transmission through Subwavelength Hole Arrays*, Applied Physics Letters **85**, 4316 (2004).

[10] K. J. K. Koerkamp *et al.*, *Strong Influence of Hole Shape on Extraordinary Transmission through Periodic Arrays of Subwavelength Holes*, Physical Review Letters **92**, 183901 (2004).

[11] C. Billaudeau *et al.*, *Angle-Resolved Transmission Measurements through Anisotropic Two-Dimensional Plasmonic Crystals*, Optics Letters **33**, 165 (2008).

[12] M. J. A. de Dood, E. F. C. Driessen, D. Stolwijk, and M. P. van Exter, *Observation of Coupling between Surface Plasmons in Index-Matched Hole Arrays*, Physical Review B **77**, 115437 (2008).

[13] L. Martín-Moreno *et al.*, *Theory of Extraordinary Optical Transmission through Subwavelength Hole Arrays*, Physical Review Letters **86**, 1114 (2001).

[14] H. T. Liu and P. Lalanne, *Microscopic Theory of the Extraordinary Optical Transmission*, Nature **452**, 728 (2008).

[15] G. Gay *et al.*, *The Optical Response of Nanostructured Surfaces and the Composite Diffracted Evanescent Wave Model*, Nature Physics **2**, 262 (2006).

[16] N. Rotenberg *et al.*, *Plasmon Scattering from Single Subwavelength Holes*, Physical Review Letters **108**, 127402 (2012).

[17] H. Liu and P. Lalanne, *Comprehensive Microscopic Model of the Extraordinary Optical Transmission*, Journal of the Optical Society of America A **27**, 2542 (2010).

[18] F. van Beijnum *et al.*, *Quasi-Cylindrical Wave Contribution in Experiments on Extraordinary Optical Transmission*, Nature **492**, 411 (2012).

[19] H. A. Bethe, *Theory of Diffraction by Small Holes*, Physical Review Online Archive (Prola) **66**, 163 (1944).

[20] J. M. Yi *et al.*, *Diffraction Regimes of Single Holes*, Physical Review Letters **109**, 023901+ (2012).

[21] F. de León-Pérez, G. Brucoli, F. J. García-Vidal, and L. Martín-Moreno, *Theory on the Scattering of Light and Surface Plasmon Polaritons by Arrays of Holes and Dimples in a Metal Film*, New Journal of Physics **10**, 105017 (2008).

[22] F. Przybilla *et al.*, *Efficiency and Finite Size Effects in Enhanced Transmission through Subwavelength Apertures*, Optics Express **16**, 9571 (2008).

[23] P. B. Johnson and R. W. Christy, *Optical Constants of the Noble Metals*, Physical Review B **6**, 4370 (1972).

Chapter 4

Scattering media characterization with phase-only wavefront modulation

A new approach for probing the scattering properties of complex media is proven experimentally. Using phase-only modulation of the light illuminating a random scattering sample, we induce and record fluctuations in the reflected speckle patterns. Using predictions from diffusion theory, we obtain the scattering and absorption coefficients of the sample from the average change in the speckle amplitude. Our approach, which is based on interference, is in principle able to give better signal to noise ratio as compared to an intensity modulation approach. We compare our results with those obtained from a knife-edge illumination method and enhanced back-scattering cone. Our work can find application in the non-invasive study of biological specimens as well as the study of light propagation in random scattering devices like solar cells or LEDs.

This chapter is submitter for publication as:
F. Mariani, W. Loeffler, M. Aas, O. S. Ojambati, P. Hong, W. L. Vos and M. P. van Exter, Optics Express (2017)

4.1 Complex scattering media

Complex scattering media are ubiquitous, spanning from artifical ones like white paint or paper to biological forms like cellular tissue or bones. In all these materials the light propagation is scrambled by multiple scattering events [1], with the effect of a reduced overall transmission when the sample thickness is larger than the transport mean free path, i.e. the average distance before a change in propagation direction occurs. The complexity of the processes happening in scattering media makes these materials challenging and fascinating to study.

Different techniques have been used to characterize optical properties of complex media. Some methods approximate light propagation as a diffusion process, thus neglecting the wave nature of light and the associated interference phenomena; examples of diffusion-based techniques are total transmission measurement [2, 3, 4] and diffuse imaging analysis [5, 6]. Other methods are based on interference and require the light to be treated as a wave. This is the case for the enhanced back-scattering (EBS) technique [7, 8, 9], the analysis of speckles statistics [10] to measure diffusion parameters [11, 12, 13], and the measurements of the transmission matrix [14, 15].

Being able to study the properties of complex media is interesting for fundamental reasons as well as for those applications that require controlling light propagation within the scattering material. Recently, wavefront-shaping techniques have been employed to control the propagation of light in complex media [16, 17] or even produce images of objects positioned beyond opaque screens [18]. Studying how light transport is affected by structural and compositional properties of a medium if of great interest in materials diagnostic and analysis of biological specimens [19], where non-invasive methods are particularly relevant.

In this work we demonstrate a new non-invasive method to measure transport and absorption parameters in three dimensional random scattering media. We spatially modulate the phase of the light illuminating a sample and analyze the intensity variations in the reflected speckle patterns. We interpret the results using an analytic solution of the diffusion equation applied to a semi-infinite complex scattering medium. Compared to diffuse imaging with point-like illumination [6], where transport is studied by measuring diffusion profile, our technique is promising in studying fields that propagate deeper into the sample, is not affected by the direct backscattered light, and does not

require a very large detection dynamic range.

4.2 From diffusion theory to speckles fluctuations

The interaction of coherent light with a random scattering medium produces speckle patterns; these appear to have a random structure [20] which is nonetheless deterministically defined by the structure of the medium. In a linear optical process, such as elastic scattering, the relation between the input field $\mathbf{E}_{\text{in}}(x', y')$ and the reflected field $\mathbf{E}_R(x, y)$ is described by the Green's tensor $\mathbf{G}(x, y, x', y')$:

$$\begin{aligned} \mathbf{E}_R(x,y) &= \mathbf{G}(x,y,x',y') \otimes \mathbf{E}_{\text{in}}(x',y') \equiv \\ &\equiv \iint \mathbf{G}(x,y,x',y')\ \mathbf{E}_{\text{in}}(x',y')\ dx'dy' \end{aligned} \tag{4.1}$$

The method that we introduce in this work is based on optical phase modulation and uses the properties of Eq. (4.1), without requiring any direct knowledge of the Green's function $\mathbf{G}(x, y, x', y')$. We consider the field incident on the sample $\mathbf{E}_{\text{in}}(x', y')$ and divide it into two halves around $x = 0$. By making use of the linearity of Eq. (4.1), we rewrite the reflected field as the sum of two components $\mathbf{E}_R(x, y) = \mathbf{E}_-(x, y) + \mathbf{E}_+(x, y)$, each given by:

$$\mathbf{E}_\pm(x,y) = \mathbf{G}(x,y,x',y') \otimes \left[H(\pm x')\ \mathbf{E}_{\text{in}}(x',y')\right] \tag{4.2}$$

where $H(\pm x')$ is the Heaviside step-function. The functions $\mathbf{E}_{+/-}(x, y)$ represent the field reflected, after propagation, upon illumination with light on only half of the illumination beam for $x > 0$ ("+" case) or $x < 0$ ("-" case); this is sketched in the inset in Fig. 4.1. In the following we consider only one polarization component of $\mathbf{E}_{+/-}$ and write the fields as $E_{+/-}$.

If we introduce an arbitrary phase retardation $\Delta\phi$ in the input beam for e.g. only the half $x < 0$, the field propagation is not affected, but the only results is a phase shift for the output field $E_-(x, y)$ as compared to $E_+(x, y)$. The total reflected field becomes $E_R = e^{i\Delta\phi}E_- + E_+$, with the phase shift $\Delta\phi$ modifying the interference between the two components. The reflected intensity $I_R(x, y) \propto |E_R(x, y)|^2$ at the scattering medium surface is obtained by substituting the expression for $E_R(x, y)$, including the phase retardation $\Delta\phi$:

$$I_R(x,y;\Delta\phi) \propto I_C(x,y) + I_A(x,y)\cos(\Delta\phi + \psi) \tag{4.3}$$

where $I_C = |E_-|^2 + |E_+|^2$, $I_A = 2|E_-^* E_+|$ and $\psi = \arg(E_+/E_-)$, with $E_{+/-}$ complex field amplitudes. The central idea of this work is resumed by Eq. (4.3):

the reflected intensity is locally modified by interference when $\Delta\phi$ is varied in a $[0, 2\pi]$ interval. By recording the intensity variations we can determine both the product of the reflected fields amplitudes and their relative phase. Since scattering and absorption properties of the medium influence the amplitudes of the reflected fields $E_{\pm}(x, y)$, they also determine the profile of $I_A(x, y)$.

To attain a practical use the interference principle in Eq. (4.3) we need to relate the field amplitudes to the scattering and absorption properties of our medium. This is possible looking at averaged results for the reflected intensity, a quantity we can directly measure. The ensemble-averaged reflected intensity $\langle I_{R\pm}(x, y)\rangle$ corresponds to the mean square value for the reflected fields amplitude, hence we can write $\langle |E_{\pm}(x, y)|\rangle \propto \sqrt{\langle I_{R\pm}(x, y)\rangle}$.

While the measured speckle-like reflected intensity $I_R(x, y)$ strongly depends on the precise positions of the scatterers, $\langle I_R(x, y)\rangle$ can be calculated by using a diffusion approximation to describe the transport of optical energy in the medium. This approximation is valid when the transport mean free path l_{tr} for the light in the medium is much smaller than the absorption mean free path l_a and light is backscattered after multiple scattering events [1, 21]. These conditions are fulfilled in our experiment.

The diffusion equation has an analytical solution for a point like source in an infinite scattering medium. This can be used to solve the case for a point-like illumination incident at $x = y = 0$ on the interface of a semi-infinite medium, which yields the radial profile of the diffuse reflected intensity $R(\rho)$ at the interface, with $\rho = \sqrt{x^2 + y^2}$. We use here the expression for $R(\rho)$ from Ref. [5] for a random medium of effective refractive index n_{eff} surrounded by air ($n_{\text{out}} = 1$).

We model the diffuse light as coming from two isotropic point sources [5, 6]: the first is located inside the medium at a depth $z_0 = (\mu_a + \mu_s')^{-1}$, with $\mu_s' = l_{tr}^{-1}$ and $\mu_a = l_a^{-1}$. The second source is an image source, necessary to fulfill the boundary condition, and it is located outside the medium at a distance $d = z_0 + 2z_b$, with the extrapolation length $z_b = (2/3)\, z_0\, A$ and A a constant that depends on the relative refractive index (e.g. $A(n_{eff}) = 4.22$, for $n_{eff} = 1.5$) [5, 22, 23]. The resulting $R(\rho)$ has the form:

$$\begin{aligned} R(\rho) \propto \frac{1}{4\pi}\Big(z_0(\mu_{\text{eff}} + \frac{1}{r_1})\frac{\exp(-\mu_{\text{eff}} r_1)}{r_1^2} \\ +(z_0 + 2z_b)(\mu_{\text{eff}} + \frac{1}{r_2})\frac{\exp(-\mu_{\text{eff}} r_2)}{r_2^2}\Big) \end{aligned} \tag{4.4}$$

where $r_1 = \sqrt{\rho^2 + z_0^2}$, $r_2 = \sqrt{\rho^2 + (z_0 + 2\ z_b)^2}$, and $\mu_{\text{eff}} = [3\mu_a(\mu_a + \mu_s')]^{1/2}$ is introduced as an effective attenuation coefficient, describing the joint effect of scattering and absorption [19].

The coefficients μ_s' and μ_a are combined in the constants z_0 and μ_{eff} defined above. Their effect on $R(\rho)$ is different: μ_s' determines the curvature and slope of $R(\rho)$ for short distances from the excitation point, whereas μ_a mainly affects the long range behavior of the reflected intensity.

The function $R(\rho)$ is the Green's function for intensity transport and allows to calculate the average reflected intensity function $\langle I_R(x,y)\rangle$ for an arbitrary illumination profile. Considering an illumination in the shape of a half-Gaussian beam, one obtains:

$$\begin{aligned}\langle I_{R\pm}(x,y)\rangle &= R(\rho) \otimes I_{\text{in}}(x',y') \equiv \\ &\equiv \iint R(\rho)\ H(\pm x')\ \exp(-\rho^2/w_{\text{in}}^2)\ dx'\ dy'\end{aligned} \tag{4.5}$$

where $H(\pm x')$ is the Heaviside step-function and w_{in} is the waist of the illumination beam. Equation (4.5) describes the knife-edge method we use later in this work, where incident light is provided in the shape of a half-Gaussian profile; for this case the two cross sections $\langle I_{R\pm}(x,y)\rangle$ and $I_{\text{in}}(x',y')$ are shown in Fig. 4.2 (a).

With the results in Eq. (4.5) we can now calculate the expected value for the speckles intensity variations $I_A(x,y)$:

$$I_A(x,y) \propto \langle |E_+(x,y)|\rangle\langle |E_-(x,y)|\rangle = \sqrt{\langle I_{R+}(x,y)\rangle\langle I_{R+}(-x,y)\rangle} \tag{4.6}$$

where we use the symmetry in our problem such that $\langle I_{R-}(x,y)\rangle = \langle I_{R+}(-x,y)\rangle$. The expression in Eq. (4.6) models the quantity $I_A(x,y)$ defined in Eq. (4.3), emerging from the interference of two fields, using the diffusion model for light transport in complex media. This equation is valid under the reasonable assumptions that the two fields $E_\pm(x,y)$ are uncorrelated and that the longitudinal coherence of the incident light is much longer than the diffuse optical path.

4.3 Experimental setup and samples

Setup description

A schematic of our experimental setup is shown in Fig. 4.1. Light from a HeNe laser (wavelength $\lambda = 632.8$nm) is delivered to the setup with a

single-mode fiber (not shown in Fig.4.3) and collimated for a beam waist of w_0 =1.6 mm. The beam is polarized in the x direction by polarizer P_0 and then reflected at normal incidence on a liquid crystal phase-only spatial light modulator (SLM) (Holoeye Pluto-VIS). The polarizer P_1 placed afterwards removes any minor depolarization introduced by SLM. In quasi-contact with the SLM we mount a knife-edge which can be moved into the optical path to block half of the beam.

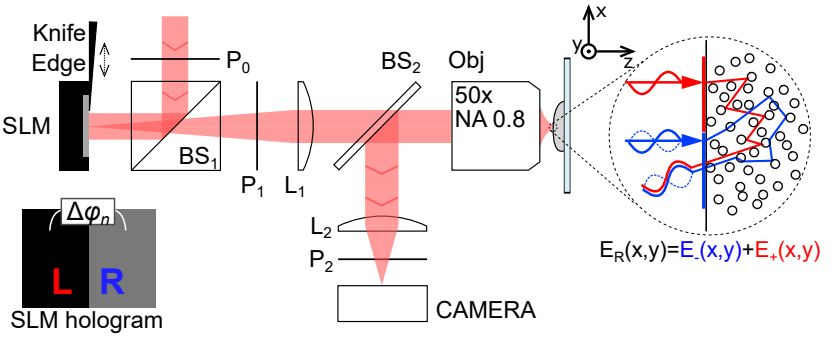

Figure 4.1: The experimental setup: a collimated laser (wavelength 633 nm) illuminates the spatial light modulator (SLM) after passing through the polarizer P_0. The wavefront-shaped light is polarized again with the polarizer P_1 and imaged on the sample with a telescope consisting of a tube lens L_1 (f=20 cm) and a 50x microscope objective.
The reflected light is collected with the same objective and its polarization is selected with the analyser P_2. A second tube lens L_2 (f = 20 cm) images the sample on a CCD camera. Bottom left: a scheme of the phase-step hologram projected on the SLM. Right: the interference between the light coming from the two halves of the SLM (red and blue lines) and exiting the sample at the same point.

The SLM surface is imaged onto the sample with a combination of a tube lens L_1 (focal length f = 20 cm) and a microscope objective (Nikon Epi Plan Fluor 50x, NA = 0.8) obtaining a final illumination spot with beam waist at the sample $w_{\text{in}} \simeq 31$ μm. This configuration allows to spatially define the phase over the incident wavefront. For convenience we choose the origin of the *(x,y)* coordinate system coincident with the center of the illumination spot. We image the sample in back-scattering geometry using the same objective and a second tube lens L_2 (f = 20 cm). We finally record an image of the sample with a CCD camera (Apogee Alta) after the analyser P_2 selects the measured linear polarization.

The sample is mounted on a 3-axis piezo stage for accurate positioning. A filtered halogen lamp provides the incoherent illumination used to focus

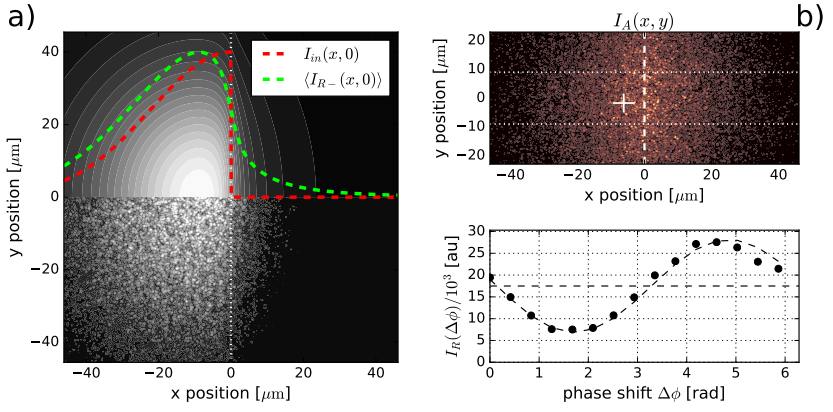

Figure 4.2: (a) Knife-edge method: the spatial speckles measured in reflection upon illumination with half a Gaussian beam (bottom part) are compared with the average speckle intensity pattern calculated with diffusion theory (top part). The two cross sections $I_{\rm in}(x,0)$ (red dashed line) and $\langle I_R(x,0)\rangle_\pm$ (green dashed line) from Eq. (4.5) are also shown. (b) Phase-step method: (Top) an example of measured speckle intensity variations $I_A(x,y)$ under phase-modulated illumination, with indicated the rectangular region used for ensemble averaging; (Bottom) the intensity as a function of the phase delay $\Delta\phi$ for the pixel pixel highlighted by a cross in the upper panel.

the sample; this avoids the appearance of speckles and allows to find regions where the sample appears flat and homogeneous within the field of view. We calculate the spatial resolution of the imaging system using the full width at half maximum of the spatial autocorrelation peak for the reflected speckle pattern, resulting in a value of $0.44\,\mu$m; this value is close to the expected diffraction limit of $0.40\,\mu$m and provides a resolution sufficient to resolve the spatial scale at which the reflected intensity decreases as an effect of diffusion.

Sample preparation

For our experiments we use three different scattering materials: dried liquid corrector (brand: Tipp-Ex) (sample 1), white paint (sample 2), and a disordered aggregate of polydisperse silica spheres (sample 3). Both samples 1 and 2 were stirred in form of suspension and deposited on a cleaned microscope slide and left to dry overnight at the room temperature. To prepare sample 3, we mixed thoroughly a suspension of silica micro-spheres (Sigma-Aldrich S5631) and deposited a few drops of the suspension on a cleaned objective substrate. The sample was then dried in an oven at 80 degrees for 30 minutes. The thickness of the samples are determined using with the microscope of our setup and have values, in the measurement regions, $h_1 = 640 \pm 6\ \mu$m, $h_2 = 290 \pm 4\ \mu$m,

$h_3 = 170 \pm 2$ μm, respectively. The overall thickness tolerance is estimated as 10%.

Experiment

We perform three different experiments (phase-step, knife edge and EBS) on each of the three samples and measure over multiple regions to verify consistency of the results. For the phase-step method, we project a phase-step hologram on the SLM with the step aligned at $x = 0$ on the sample. The projected hologram introduces a phase difference $\Delta\phi$ between the right and left side of the illumination spot. We image the reflected intensity $I_R(x, y, \Delta\phi_i)$ while applying $N = 15$ discrete phase-steps $\Delta\phi_i = i\frac{2\pi}{N}$ with $i = 0, \ldots, N-1$. By fitting Eq. (4.3) to the measured intensity as a function of $\Delta\phi_i$ for each pixel, we obtain the experimental values for the speckle intensity variations $I_A(x, y)$. The bottom plot in Fig. 4.2(b) shows $I_R(x, y, \Delta\phi_i)$ for a single pixel as a function of $\Delta\phi_i$.

The second approach is the knife-edge method, a diffuse imaging measurement. In this case half of the incident intensity profile is blocked with a knife-edge (see Fig. 4.1) obstructing the beam for $x > 0$, as described in Eq. (4.5). A typical intensity profile measured with sample 1 is shown in Fig. 4.2(a), where it is compared to the prediction obtained by numerically integrating Eq. (4.5). Note that the measurements show a speckle pattern, because we measure only for one specific realization of the random medium, whereas the diffusion theory only describes a smooth average intensity.

In the third method we measure the EBS cone of the samples using the setup described previously in Ref. [9]. The EBS cone appears on top of the diffuse reflection from the scattering media because of interference in the far field of counter-propagating optical paths in the medium. Experimental and theoretical work shows that the maximum intensity of the EBS cone is exactly two times the value of the diffuse reflected intensity and that the angular width of the cone depends on the transport mean free path of the scattering medium [8, 7].

To compare our measurements with both the models for phase-step and knife-edge methods we first average $I_A(x, y)$ and $I_-(x, y)$ along the y direction over a rectangular region, centred with the beam, spanning the full width of the images and limited to a band of $\Delta y = 18$ μm in the vertical direction (see Fig. 4.2(c)). In this region the diffuse reflected intensity modelled in Eq. (4.5) has almost no dependence on y. Since Δy is about $M = 40$ times wider

than the average speckles size, it is safe to assume that the average values $I_-(x) \equiv \langle I_-(x,y)\rangle_y$ and $I_A(x) \equiv \langle I_A(x,y)\rangle_y$ are equivalent to an ensemble average over different realizations of the scattering medium. The averaging also reduces the relative error on $I_-(x)$ and $I_A(x)$ by a factor $M^{-1/2}$.

The results we present for phase-step and knife-edge experiments are obtained detecting only the crossed-polarized backscattered light. This choice offers the advantage of removing the specular reflection of the sample surface, which conserves the incident linear polarization and is not accounted for by the diffusion model. Additionally, this also removes the stray light, originating from reflections from the optical components, in particular the microscope objective. We note that for all samples the reflected intensity in parallel and orthogonal polarization has about the same value, indicating that we are in the regime of nearly complete depolarization.

4.4 Results

The execution of the three experiments and subsequent data analysis are identical for all three samples: here we present the procedure applied to sample 2 (white paint) and only summarize the results for the other samples. The results for sample 2 are based on an average over $n = 4$ different positions. Ensemble averaging is further assured by the averaging along the y direction, as previously mentioned. For the EBS measurements we only present the final results.

To determine the transport and absorption mean free path it is necessary to know the effective refractive index n_{eff}. The values we use for n_{eff} for our three samples are approximate values and are listed in Table4.1. These value for n_{eff} are only parameter and are not critical when comparing three different methods. Real values can be measured with transmission measurements [24] or approximated with the effective medium theory [25].

In the phase-step experiment we measure $I_A(x,y)$, the speckle amplitude modulation defined in Eq. (4.6). In Fig. 4.3(a) we show the experimental curve $I_A(x) = \langle I_A(x,y)\rangle_y$ for sample 2, after averaging over four position on the sample surface and normalized to its values in proximity of $x = 0$. The measured $I_A(x)$ is symmetric around a maximum at $x = 0$, decaying almost exponentially with increasing distance form the phase step.

Using non-linear least-squares method, we fit the experimental data with the model in Eq. (4.6). The values of transport and absorption mean

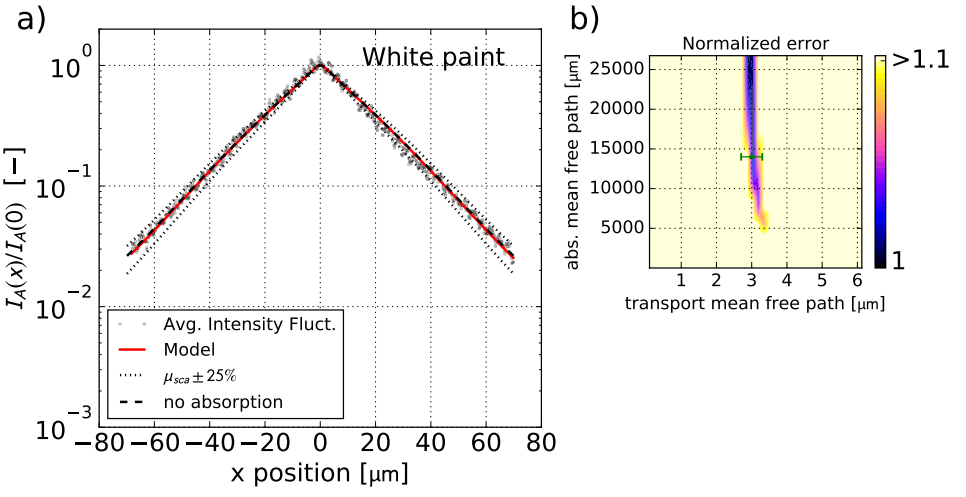

Figure 4.3: Phase-step results for the white paint. (a) Average speckle intensity modulation $I_A(x)$, normalized to its value at $x = 0$, for illumination with the phase-step positioned at $x = 0$. The red solid line shows the best fit curve with $l_{\mathrm{tr}} = 3.0$ μm and $l_a = 14$ μm. In the plot we also indicate the model with a transport coefficient altered by ±25% (dotted lines) and the model without absorption (dashed line). (b) The normalized error function in the parameter space (l_{tr}, l_a), calculated as defined in the text, with indication of the error minimum identifying the best fit parameters for the fit curve in panel (a), with the error bar for l_{tr}.

free path that fit the experimental data best are $l_{\mathrm{tr}} = 3.0 \pm 0.3$ μm and $l_a = 14.0 \pm 9$ mm, where the errorbars are given by the standard deviation calculated from the covariance matrix

The results of the knife-edge method are shown in Fig. 4.4(a), in the form of a typical average intensity profile $I_-(x) = \langle I_-(x, y)\rangle_y$ normalized to its value at $x = 0$. The measured curve shows a nearly half-Gaussian profile with a rounded top on the illuminated side and a diffuse intensity on the non-illuminated side, with its value decaying wit the distance from the knife edge.

We use Eq. (4.5) as model for the least square method; for sample 2 ($n_{\mathrm{eff}} = 1.4$) the best values for the transport and absorption mean free paths with this method are $l_{tr} = 2.6 \pm 0.1$ μm and $l_a = 19 \pm 6$ mm.

In Fig. 4.4(a) we also show, for comparison, the diffuse intensity profile of point-like illumination, instead of step-like, calculated with Eq. (4.4) using the best-fit parameters obtained from the knife-edge experiment. Fig. 4.4(a) clearly shows how the knife-edge illumination provides a more accurate view

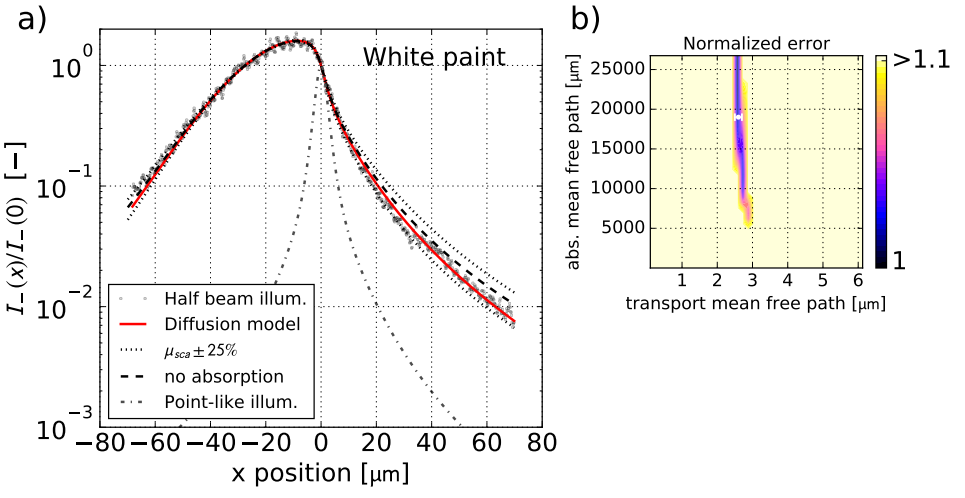

Figure 4.4: Knife-edge results for the white paint. (a) The average reflected intensity with half of the illumination spot blocked by the knife-edge. The intensity is averaged over the y direction over a $18\ \mu$m strip around the center of the illumination spot. Experimental data are fitted with the diffusion model in Eq. (4.5) to obtain the best fit parameters $l_{\rm tr}$ and l_a (in red). In the plot we also indicate the same model with a transport coefficient altered by $\pm 25\%$ (dotted lines), and the model without absorption (dashed line). The intensity profile for point-like illumination is plotted for comparison. (b) The normalized error function in the parameter space ($l_{\rm tr}$, l_a), calculated as defined in the text, with indication of the error minimum identifying the best fit parameters for the fit curve in panel (a), with the error bar for l_{tr}.

on the diffusion as a result of the dimensionality of the problem. For point illumination the intensity drops rapidly as it diffuses in two dimensions with average circular symmetry, whereas the knife-edge case has approximately a half-plane source and the intensity drops less steep as light diffuses only in one main direction.

The values of $l_{\rm tr}$ obtained from the two methods for Sample 2 are compatible within the error bars. In both cases, l_a is almost four orders of magnitude larger than $l_{\rm tr}$. In Table 4.1 we summarize the results for scattering and absorption parameters (for $\lambda = 632.8\,$nm) obtained from both methods on the three samples, and compare them to the EBS method. All samples show very low absorption and different scattering strengths, ranging from $l_{\rm tr} \simeq 0.75\ \mu$m for liquid corrector, to $l_{\rm tr} \simeq 5.0\ \mu$m for the aggregates of SiO_2 micro-spheres.

		Phase Step	Knife Edge	EBS
Sample 1 (Tipp-Ex)	$l_{\mathrm{tr}}[\mu\mathrm{m}]$	1.0 ± 0.4	0.75 ± 0.05	0.95±0.1
(n_{eff}=1.6)	l_a[mm]	5.3 ± 2.8	5.3 ± 1.1	
Sample 2 (white-paint)	$l_{\mathrm{tr}}[\mu\mathrm{m}]$	3.0 ± 0.3	2.6 ± 0.1	1.7±0.2
(n_{eff}=1.4)	l_a[mm]	14 ± 9	19 ± 6	
Sample 3 (SiO_2)	$l_{\mathrm{tr}}[\mu\mathrm{m}]$	5.0 ± 1.5	4.2 ± 0.5	2.9±0.3
(n_{eff}=1.4)	l_a[mm]	1±1	1 ± 0.4	

Table 4.1: Transport and absorption mean free paths l_{tr} and l_a for $\lambda = 632.8$ nm as determined from fits for three different measurement techniques: phase-step method, knife-edge method and enhanced back-scattering (EBS), with indicated n_{eff} assumed in the three methods for each sample.

4.5 Discussion

The phase-step method that we introduce to study the properties of a diffusive medium proves able to measure the transport mean free path for the three samples under study. We obtain values for l_{tr} that are similar to those calculated with the knife-edge experiment.

The results from the phase-step and knife-edge experiments agree within their error bars for all three samples. In the case of Tippex, the agreement extends also to the results of EBS, whereas for samples 1 and 2 the EBS yields lower values for l_{tr} than the other methods. The origin of this difference might be the different relative weights for long and short scattering paths in the (angular resolved) EBS measurements as compared to (spatially resolved) knife-edge and phase-step experiments.

The very low absorption in our samples, with l_a orders of magnitude higher than l_{tr}, makes it difficult to determine the absorption mean free path accurately, and it is only possible to give an upper limit for absorption. To visualize this, we report in Figs. 4.4(b) and 4.3(b) the error function between the model and the measurements in the parameter space (l_{tr},l_a), calculated as the sum of the squared residues for the logarithms of both model and experimental data $Err = \sum \left(ln(I_{fit}) - ln(I_{exp})\right))^2$ and normalized to its minimum value.

The two false-color plots show the normalized error function up to a value of $1 + 1/\sqrt{n \cdot M}$, with $n = 4$ number of averaged measured positions and M number of speckles over which averaging is performed. The error function plots indicate that, in our case, we can only determine a lower bound to l_a.

To help to understand how sensitive both methods are to l_{tr} and l_a, we also plot in Figs.4.4(a) and Fig.4.3(a) the models with virtually no absorption ($l_a = 10^6 \mu$m) and with l_{tr} modified by 25%.

One aspect that limits the accuracy of the calculation of transport and absorption mean free path with the phase-step method is, in our case, the size of the illumination spot. In our setup $w_0 \mu_{\text{eff}} \simeq 1 - 10$ and as a consequence illumination and diffused reflected light decay on the same spatial scale, making it more difficult to separate the two dynamics. By calculating the case of a half-plane illumination, obtained as the limit case of a Gaussian illumination with $w_0 \to \infty$, we noticed that the function $I_A(x)$ shows a more prominent dependence on the values of l_{tr} and l_a. This suggests that the use of high magnification objectives is not necessarily optimal for the phase-step method, as a larger illumination area might instead be preferred. We also note that a reduction of the collection NA increases the visibility of the spatial speckles, and thus the absolute value of $I_A(x)$ together with the signal to noise ratio, but at the price of a reduced resolution.

For both knife-edge and phase-step experiments we use results from the diffusion model, but the two techniques measure different quantities, the diffuse intensity and the speckle intensity modulation amplitude, respectively. This difference offers a potential advantages for the phase-step method over intensity modulation. First the dynamic range: the intensity observed in the knife-edge experiment depends on the square of the field $I_-(x) \propto |E_-(x)|^2$, and therefore decays faster away from $x = 0$ than the speckle intensity modulation $I_A(x)$, which depends linearly on the field $E_-(x, y)$. Weak fields are therefore easier to measure, similarly as in homodyne-detection schemes, as visible from the curves in Figs. 4.4 and 4.3. The second advantage of the phase-step method is that it is insensitive to a constant incoherent background, allowing for instance conventional microscopy images taken simultaneously. Finally, both our knife-edge and phase-step technique have an advantage over the more common diffuse imaging with spot-like illumination: by avoiding concentrating the input intensity in a focused spot they prevent the presence of non-linear optical effects and therefore also produce useful results while measuring the scattering properties of non-linear optical media.

We conclude our discussion with a technical remark on the use of the SLM. In many SLM-based experiments it is crucial to apply a position dependent phase correction to the SLM prior to the experiment in order to control the wavefront curvature. This is not necessary in our experiment, since the SLM is in the image plane of the sample and the measurements are based only on relative phase shifts rather than absolute phase value. Our experiment can even be performed without an SLM, using only a phase-step $\lambda/4$ plate on the image plane of the sample, centred with respect to the beam: rotating the plate by 180^0 around its axis produces an effective phase change of $\Delta\phi = \pi$ between the two halves of the beam. This is sufficient to measure the average amplitude variation of spatial speckles, although with a loss of signal-to-noise ratio of factor $\langle cos^2(\phi)\rangle^{-1} = 1/2$ with respect to our implementation. Finally, although we use a wavelength calibration for our SLM, this is also not strictly necessary as it can be calculated after the experiment from the intensity fluctuation of even a single pixel.

4.6 Conclusions

We have shown a new method to measure optical transport properties of a random scattering medium via illumination with phase-only modulated light. From the position dependence of the intensity modulation of the spatial speckle in reflection we are able to determine the transport mean free path and the absorption length. Better estimations would be possible in samples with shorter absorption mean free path but still in the diffusion regime, as for instance in biological tissues. All this is possible thanks to the linearity of the field transport and by implementing a numerical integration of the known diffusion model for light transport in random media.

The phase-modulation method has potential advantages over diffused imaging: it is not sensitive to incoherent background and offers the ability to investigate longer propagation lengths. Our method can be implemented in standard optical microscopes also without a SLM and is a viable non-invasive technique for studying materials and biological tissues.

Bibliography

[1] M. C. W. van Rossum and T. M. Nieuwenhuizen, *Multiple scattering of classical waves: microscopy, mesoscopy, and diffusion*, Rev. Mod. Phys. **71**, 313 (1999).

[2] R. H. J. Kop, P. de Vries, R. Sprik, and A. Lagendijk, *Observation of Anomalous Transport of Strongly Multiple Scattered Light in Thin Disordered Slabs*, Phys. Rev. Lett. **79**, 4369 (1997).

[3] J. G. Rivas *et al.*, *Optical transmission through strong scattering and highly polydisperse media*, EPL **48**, 22 (1999).

[4] P. M. Johnson *et al.*, *Time-resolved pulse propagation in a strongly scattering material*, Phys. Rev. E **68**, 016604 (2003).

[5] T. J. Farrell, M. S. Patterson, and B. Wilson, *A diffusion theory model of spatially resolved, steady-state diffuse reflectance for the noninvasive determination of tissue optical properties invivo*, Medical Physics **19**, 879 (1992).

[6] P. M. Johnson, T. van der Beek, and A. Lagendijk, *Diffuse imaging and radius dependent frequency correlations in strongly scattering media*, Optics Express **22**, 13330 (2014).

[7] P.-E. Wolf and G. Maret, *Weak Localization and Coherent Backscattering of Photons in Disordered Media*, Phys. Rev. Lett. **55**, 2696 (1985).

[8] M. P. V. Albada and A. Lagendijk, *Observation of Weak Localization of Light in a Random Medium*, Phys. Rev. Lett. **55**, 2692 (1985).

[9] O. L. Muskens and A. Lagendijk, *Broadband enhanced backscattering spectroscopy of strongly scattering media*, Optics Express **16**, 1222 (2008).

[10] J. W. Goodman, *Speckle phenomena in optics: theory and applications* (Roberts and Company Publishers) (2007).

[11] C. A. Thompson, K. J. Webb, and A. M. Weiner, *Diffusive media characterization with laser speckle*, Applied Optics **36**, 3726 (1997).

[12] J. D. McKinney, M. A. Webster, K. J. Webb, and A. M. Weiner, *Characterization and imaging in optically scattering media by use of laser speckle and a variable-coherence source*, Optics Letters **25**, 4 (2000).

[13] N. Curry *et al.*, *Direct determination of diffusion properties of random media from speckle contrast*, Optics Letters **36**, 3332 (2011).

[14] S. M. Popoff *et al.*, *Measuring the Transmission Matrix in Optics: An Approach to the Study and Control of Light Propagation in Disordered Media*, Phys. Rev. Lett. **104**, 100601 (2010).

[15] D. Akbulut *et al.*, *Optical transmission matrix as a probe of the photonic strength*, Phys. Rev. A **94**, 043817 (2016).

[16] I. M. Vellekoop, E. G. van Putten, A. Lagendijk, and A. P. Mosk, *Demixing light paths inside disordered metamaterials*, Optics Express **16**, 67 (2008).

[17] O. S. Ojambati *et al.*, *Coupling of energy into the fundamental diffusion mode of a complex nanophotonic medium*, New J. Phys. **18**, 043032 (2016).

[18] J. Bertolotti *et al.*, *Non-invasive imaging through opaque scattering layers*, Nature **491**, 232 (2012).

[19] A. Kienle *et al.*, *Spatially resolved absolute diffuse reflectance measurements for noninvasive determination of the optical scattering and absorption coefficients of biological tissue*, Applied Optics **35**, 2304 (1996).

[20] J. C. Dainty, in *Progress in Optics*, Vol. 14, edited by E. Wolf (Elsevier) (1977)

[21] A. Lagendijk, R. Vreeker, and P. De Vries, *Influence of internal reflection on diffusive transport in strongly scattering media*, Physics Letters A **136**, 81 (1989).

[22] R. C. Haskell *et al.*, *Boundary conditions for the diffusion equation in radiative transfer*, Journal of the Optical Society of America A **11**, 2727 (1994).

[23] R. Aronson, *Boundary conditions for diffusion of light*, Journal of the Optical Society of America A **12**, 2532 (1995).

[24] J. Gómez Rivas *et al.*, *Experimental determination of the effective refractive index in strongly scattering media*, Optics Communications **220**, 17 (2003).

[25] P. Chýlek *et al.*, *Light Scattering by Nonspherical Particles : Theory, Measurements, and Applications* (Academic Press) (2000).

Chapter 5

Light propagation in rough thin-film solar cells

We investigate scattering and propagation of light in rough thin-film Silicon solar cells, a quasi two dimensional absorbing random scattering medium. We use various techniques where we image the cell under structured coherent illumination with both intensity and phase-step function, or measure the angular distribution of the scattered light. By combining these measurements with polarization selection, and comparing them with a reference sample, we study the depolarization properties of the solar cell and obtain information on the transport and absorption of light in our sample. We model the results in terms of the guided modes of the structure and of the reflection at the skewed surfaces of the rough structure. Understanding light transport and photon management is a step towards the improvement of the performances of solar cells.

5.1 Introduction

In the quest for clean sources of energy, photovoltaic technologies play a prominent role and much research effort is thus devoted to optimize the performance of solar cells. Improvements can involve various aspects: the production process, the absorbing material, the structure of the cell [1], and the light collection and trapping strategy [2, 3, 4]. Of all the possible forms of photovoltaic devices, thin-film silicon single-junction solar cells are the simplest and most widespread, for the simplicity of their structure and the modest cost of production.

The performance of a thin-film solar cell depends on many parameters, the thickness being one of them. The thickness affects both the probability for light to generate charge carriers, and the efficiency of carriers collection at the electrodes. For instance in nano-crystalline silicon (nc-Si), the absorption length for light with $\lambda = 633$ nm is 2.5 μm: a much thinner layer of Si gives a reduced optical path in the absorbing medium for light at this wavelength, and thus fewer charge carriers generated. On the other hand, a thinner absorber reduces the losses during charge transport to the electrodes of the cell, allowing a more efficient collection of the photovoltaic current. A compromise between these two aspects leads, for single junction cells, to a typical thickness of the order of 1-10 μm, also varying on the type of Si used.

One way to increase the coupling of light to a semiconductor device is to introduce scattering, e.g. by employing patterned interfaces [5, 6, 7]. Compared to a flat interface, a structured one scatters light at high angles inside the solar cell, also beyond the angle of total internal reflection. This effectively traps the light and allows to achieve higher external efficiency in cells with a thickness smaller than the typical absorption length.

Several patterning strategies can be used: plasmonic particles [3], periodic dielectric structures [8, 9] or optimized random patterns [10, 11]. The latter offer the advantage of having a truly broad spectral response [12]; also, these can be relatively easily fabricated, for instance by chemically etching the substrate. For some configurations the increase in light absorption can be up to one order of magnitude relative to similar flat structures [13], and beat conventional limits for absorption enhancement [2].

Randomly patterned thin solar cells are quasi-2D random scattering medium. Extensive research already exists for the control of light in truly three dimensional random scattering media [14]. In that case it was demon-

strated that light propagation can be controlled with the use of wavefront shaping techniques to achieve tight localization in a focus spot [15, 16], to image through a scattering medium [17], and to maximize the amount of fluorescence generated by a weakly absorbing medium [18]. These techniques rely on the linear properties of the scattering process and the transmission matrix [19] and have not yet been applied to quasi-2D samples involving scattering thin layers, in particular in the presence of absorption. This raises the question of to what extent wavefront shaping techniques can be used to enhance absorption also in very thin textured silicon solar cells.

The concept of achieving high absorption in 3D random scattering media was theoretically and numerically explored by Chong et al. [20] and named Coherent Enhanced Absorption (CEA). The increase of absorption is theoretically possible in random media in a broad range of wavelengths [20]. A first attempt of the use of wavefront shaping in an organic solar cell has shown the possibility to localize the light absorption near the electrodes of the cell to reduce the electron transport losses and thus increase the cell external quantum efficiency [21]. Nevertheless, CEA is physically different from an optimization of the carrier collection, so its potential in thin-Si solar cells remains to be demonstrated.

The possibility of using wavefront shaping to control the light distribution in random media requires light to propagate in the medium and produce interference phenomena, which can be advantageously exploited. In this work we investigate light transport within a solar cell, in order to quantify the potential for CEA in single thin nano-crystalline silicon (nc-Si) textured cells. In particular, we investigate which fraction of the incident field penetrates inside the Si layer, escapes from the cell, and is scattered back outside.

We perform our experiments using coherent illumination and studying the backscattering properties of the sample. Depolarization properties of the solar cell play an important role in our study; despite being a minor effect with little relevance for studies of electronic performances, they provide additional insight on the scattering and transport mechanisms. Moreover, by looking at depolarized light we are able to minimize the effect of stray-light in our measurements.

After introducing in Sec. 5.2 and 5.3 the sample we use and the experimental setup, we present in Sec. 5.4 our studies of polarization-resolved reflection, identifying both the positions from where reflected light originates and its angular properties. Further, we investigate the transport properties of the

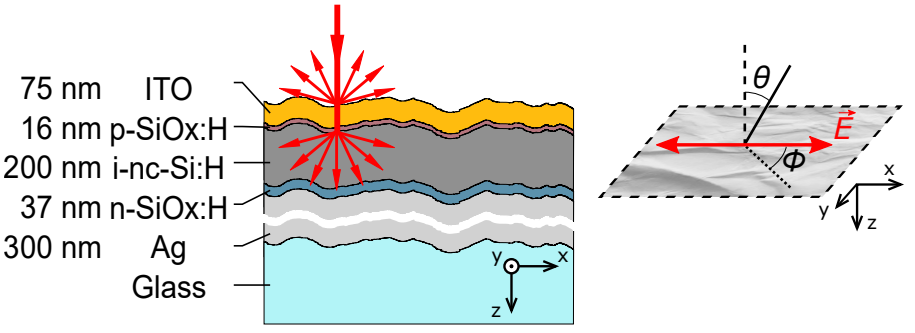

Figure 5.1: Left: a cross section of the rough thin-film solar cell used in the experiments including the nominal thickness of each layer. The roughness of the cell is defined by the glass substrate, on top of which the other layers are deposited. The roughness depth and profile are on scale, and extracted from AFM measurements. The relative thickness of all layers is also on scale. Right: definition of the polar angles used in the remainder of the text, defined with respect to the normal to the average sample plane (dashed line) and to the direction of the incident polarization (electric field in red)

layered structure by using knife-edge illumination and report the results in Sec. 5.6. In Sec. 5.7 we model the light-guiding properties of our structure. A general discussion on the results is given in Sec. 5.9.

5.2 Thin-film Si solar cell

The solar cell used in our experiment was fabricated in the department of Electrical Sustainable Energy, led by Prof. M. Zeman at the Technical University of Delft. A scheme of the solar cell is shown in Fig. 5.1. This cell is composed of several layers deposited on a nano-patterned glass substrate, located at the back of the cell. The glass surface defines the roughness of the cell as each layer reproduces the morphology of the underlying one. The first material deposited on the glass substrate is a 300 nm thick Silver layer. This serves two purposes: it reflects the incoming radiation back into the layers above, thereby doubling its optical path in the absorbing material, and it acts as back contact. The presence of the Ag reflector makes it impossible to perform transmission measurements on our solar cell. The absorptive layers are evaporated on top of the Ag reflector in the form of a three-layer p-i-n structure, with nominal thickness of 16 nm (p-SiOx:H), 200 nm (i-nc-Si:H) and 37 nm (n-SiOx:H). A 75 nm layer of transparent conductive tin oxide (ITO) is deposited as a front contact for the cell.

Our sample is similar to commercially available solar cells but much thin-

ner; this does not maximize the generation of photo current but simplifies the study of light transport by reducing the number of allowed guided modes propagating in the solar cell. Figure 5.2 shows part of the morphology of our solar cell with the roughness characterized by atomic force microscopy (AFM). From the topographic profile we can determine the root mean square (rms) roughness σ_{rms} and its lateral correlation length l_c. For our sample we obtain $\sigma_{rms} = 165$ nm and $l_c \simeq 1.2$ μm.

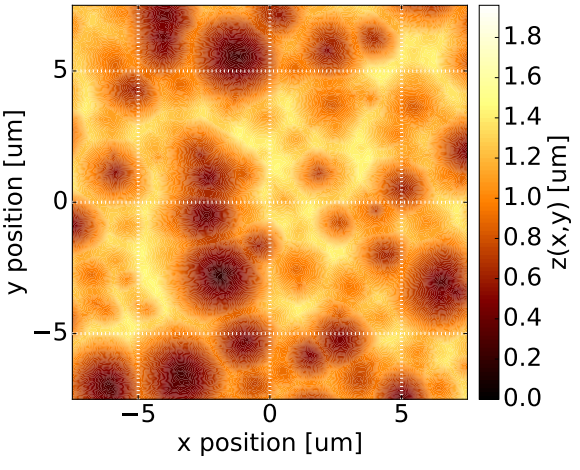

Figure 5.2: AFM profile of a portion of the surface of the solar cell used in our study shows that the structure is organized in *valleys* and ridges with average size of $l_c \simeq 1.2$ μm.

5.3 Experimental Setup

We study the scattering properties of our solar cell with the backscattering microscope setup depicted in Fig. 5.3. Light from a He-Ne laser ($\lambda = 632.8$ nm) is routed through a single-mode fiber and collimated in a Gaussian beam of diameter 3.3 mm; its polarization is set horizontal with the polarizer P_0. The beam is reflected by a phase-only reflective spatial light modulator (SLM) which is imaged on the sample surface using a telescope composed of a tube lens L_1 ($f = 200$ mm) and a microscope objective (100x, NA $= 0.9$). Possible spurious depolarization effects from the SLM are removed with an additional polarizer P_1. The polarization of the light incident on the sample is oriented along x. In front of the SLM we mount a knife edge that can be moved in the beam to obscure half of it.

The light reflected from the solar cell is collected through the same objective and imaged on a CCD camera after passing through a second tube lens L_2

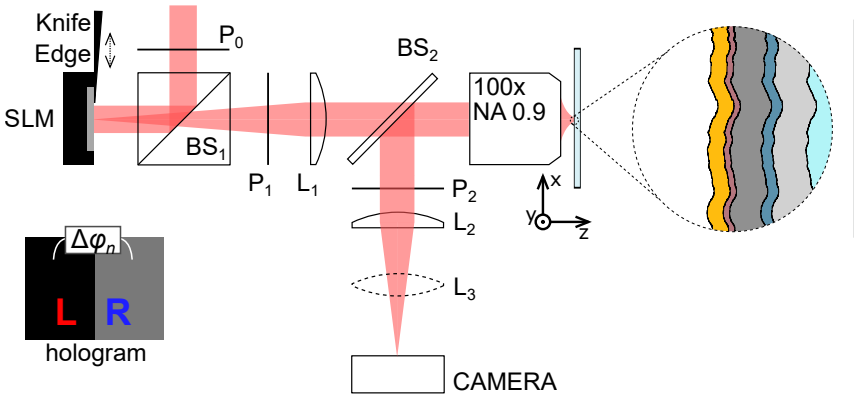

Figure 5.3: The experimental setup: a collimated laser beam illuminates the spatial light modulator (SLM) after passing through polarizer P_0. The light reflected by the SLM is polarized again with polarizer P_1 and imaged on the sample with microscope optics comprising of a tube lens L_1 (f = 20 cm) and a 100x microscope objective (NA=0.9). The reflected light is collected with the same objective. The sample is imaged with a second tube lens L_2 (f = 20 cm) on a CCD camera, after passing through the analyser P_2 which selects the polarization of the detected light. In the encircled inset a magnified view of the rough solar cell. The bottom left inset shows a scheme of the hologram projected on the SLM for the phase-step method.

($f = 200$ mm). The analyser P_2, mounted on a computer controlled rotating stage, selects the linear polarization of the reflected light to be either parallel or orthogonal to the incident polarization. Our setup also employs a flip-lens L_3 ($f = 100$ mm) which allows to obtain information on the far field of the light reflected by the sample.

The sample is mounted on a 3-axis piezo-stage for precise positioning. We correct our data for the polarization dependent reflectance of the beam-splitter BS_2 and for the incident intensity, adjusted using neutral density filters (not shown in Fig. 5.3) to use the full dynamic range of our camera in the different measurement configurations.

Although the wavelength we use falls within the band of the anti-reflection coating of the optics, residual interfacial reflection are the most prominent nuisance in our setup. These originate in particular from the microscope objective and affect the signal for measurements where P_2 is set to detect the polarization parallel to the incident one. A small shift of the objective off the optical axis reduces this unwanted intensity component by almost factor 10, although still leaving unwanted residuals (see Appendix 5.B). Also for this rea-

son we focus our analysis on the depolarized component of the backscattered light.

5.4 Polarization resolved reflection

Incident light interacts with the solar cell in a complex way and the reflected field carries information on the scattering occurring within the layered structure. We report the results on the overall reflectivity of our solar cell, on the position dependence of the reflected light on the sample surface, and on the angular distribution of the backscattered light. In particular, we look at the depolarization properties of the solar cell.

We use the setup shown in Fig. 5.3 without the knife edge. A flat bulk silicon wafer serves as a reference sample to measure the response of the instrument, and provides a comparison with the solar cell. This also allows a relative intensity calibration, by assuming the reflectance of silicon to be $\mathrm{R} = |r_{Si}|^2 = 0.347$, with r_{Si} the Fresnel coefficient for $\lambda = 0.633\,\mu$m for normal incidence. With the value for R we determine the signal expected at the camera for the incident intensity $I_{in}(x, y)$.

5.4.1 Total reflectance measurements

We first determine the total reflection from both the reference sample and the solar cell. The light backscattered from the solar cell has a speckle-like structure with a Gaussian envelope; we average the data recorded at ten different positions on the sample surface to obtain a smoother ensemble-averaged profile $\bar{I}_{\parallel/\perp}(x, y)$

We first examine the results for the Si reference sample. While for the parallel polarization we have $\bar{I}_{\parallel}/\bar{I}_{in} = 0.347$ by definition, for the orthogonal polarization we measure $\bar{I}_{\perp}/\bar{I}_{in} = 5.5 \cdot 10^{-5}$. We define the depolarization ρ as the ratio between the total intensity reflected in the orthogonal polarization with respect to the one in parallel polarization. For the reference sample we find $\rho = I_{\perp}/I_{\parallel} \simeq 1/6500$. This result is comparable to the extinction ratio specified for the analyser P_2 (1:10000) and suggests that $\bar{I}_{\perp}(x)$ for the reference sample is the remaining of the specularly reflected light.

The solar cell reflectance is measured with the same approach. The cell yields $\bar{I}_{\parallel}(x)/\bar{I}_{in}(x) = 0.43$ in parallel polarization and $\bar{I}_{\perp}(x)/\bar{I}_{in}(x) = 8.9 \cdot 10^{-3}$ for the orthogonal polarization, giving a depolarization ratio $\rho = I_{\perp}/I_{\parallel} = 1/48$.

For parallel polarization the solar cell reflects more than the silicon by a factor 1.24 (see Fig. 5.9). We attribute this to the presence of the Ag back-reflector. More important, our sample shows a much stronger signal for light backscattered in the orthogonal polarization (200 times more than the reference), indicating that scattering by surface texturing plays a role in depolarization properties of our structure.

We note that the higher reflectance values for the rough solar cell are underestimations of the real values, because the light collection is limited by the numerical aperture of the setup.

Despite a clear depolarization effect, the solar cell reflection with $\rho \simeq 0.02$ is still surprisingly polarized as compared, for instance, to a volume scatterer such as white paint, for which $\rho \simeq 0.89$ (see Ch. 4). Although relatively weak, depolarized light is interesting because it has potentially undergone multiple scattering events. We examine this polarization component more closely.

5.4.2 Polarized imaging

We investigate depolarization happening at the solar cell by imaging the reflected intensity in parallel polarization $I_{\parallel}(x, y)$, as well as the intensity $I_{\perp}(x, y)$ reflected at orthogonal polarization. The results are shown in Fig. 5.4 for a small region of the sample, in a single position. To highlight the effect of coherence in the backscattering of the cell, we also show an image of the solar cell under incoherent illumination, obtained by illuminating the sample with light from a halogen lamp, filtered in the spectral band $625 \pm 15\,\mathrm{nm}$ to avoid chromatic aberrations.

In the case of reflection from coherent illumination detected in parallel polarization, shown in Fig. 5.4 (a), light is mainly organized in ring-like structures which are reminiscence of the rims and valleys of the roughness topology shown in Fig. 5.2. This intensity distribution is accompanied by concentric rings towards the center of the valleys, which is also frequently a bright spot.

For orthogonal polarization, shown in Fig. 5.4 (b), the distribution of the intensity appears to be complementary to the one observed under parallel polarization: it is mostly localized in spots that hardly scatter in parallel polarization and hence is also correlated with the morphology.

The patterns in Fig. 5.4 are not a novelty: reflected intensity distribution similar to the one we measure have also been observed in transmission on rough ZnO interfaces [22, 23, 24]. In this case, bright rim-like structures were measured with near-field techniques. These were attributed to guided modes

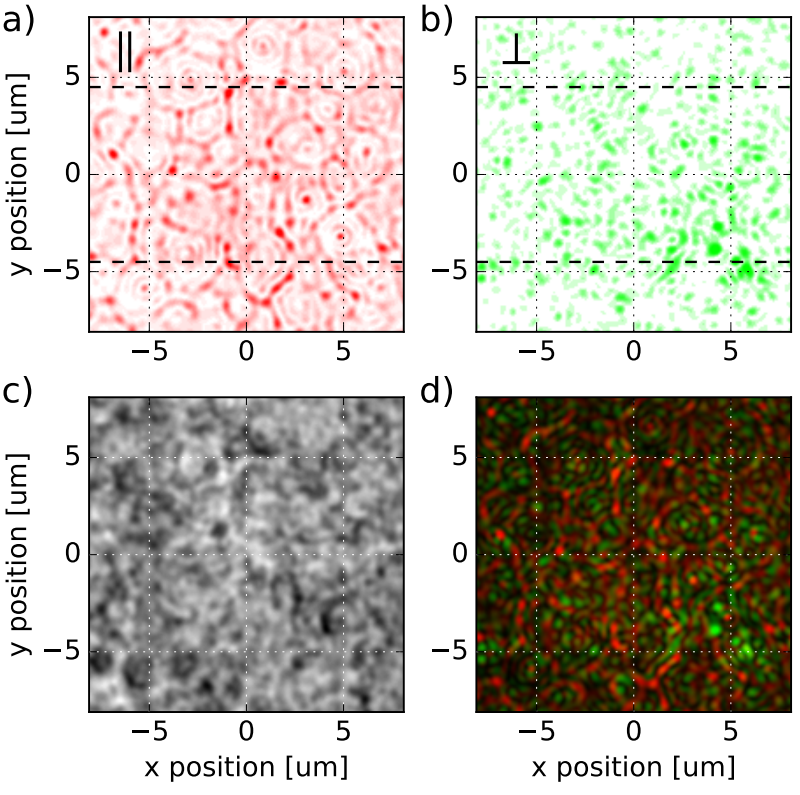

Figure 5.4: Images of the surface of the solar cell under different conditions: a,b) coherent illumination with horizontally polarized laser light (633 nm), observed for polarization respectively parallel (a) and perpendicular (b) to the incident one; c) incoherent illumination from spectrally filtered halogen lamp (625 ± 15 nm), where bright areas correspond to locations with higher reflectivity; d) overlay of panels a) and b) for direct comparison. The brightness of the two color scales are not proportional to the reflected intensities, which in orthogonal polarization is on average a factor 1/48 weaker than the intensity reflected in parallel polarization. The dashed lines in panels (a-b) indicate the strip considered in Sec. 5.6 for data averaging along y.

propagating in the structure and to standing waves which preferentially occupy the rims of the surface topology. The brighter areas were also identified as the spots of highest absorption enhancement with respect to an unstructured sample [23].

The similarity between our results and these earlier works is surprising for several reasons. First, for the measurement technique: the previous studies were based on near-field detection techniques, with access to the full angu-

lar spectrum of the emission, whereas our detection is necessarily limited by the numerical aperture of the objective. Secondly, for the sample structure: the ZnO layers were deposited on flat glass, rough only on the upper side, whereas our sample has a stratified structure. Finally the textured ZnO was illuminated through the substrate, whilst our reflection measurements include contributions from multiple surfaces, including the Ag reflector. The observed analogies indicate that the distribution of intensity in parallel polarization is partially determined by the topology of the sample.

We also calculate the intensity probability distribution $P_{\parallel/\perp}(I)$ for the intensity profiles $I_{\parallel/\perp}(x, y)$ shown in Fig. 5.4 (a-b). The calculated $P_{\parallel/\perp}(I)$ show an exponential dependence, characteristic of fully developed speckles, for both parallel and perpendicular polarization. Hence, the intensity statistics of our patterns resembles that of speckles despite the possibility of recognizing in the patterns a correlation to sample morphology.

5.5 Angular reflection properties

We obtain additional information on the scattering processes at the solar cell by studying the angular properties of the backscattered light. We collect the reflection far-field profiles by introducing the additional flip lens L_3 ($f = 100$ mm) between the tube lens L_2 and the camera. We measure the reflected intensity in both polarizations $I_{\parallel/\perp}(\theta, \phi)$, with θ and ϕ respectively the polar and azimuthal spherical coordinates (see Fig. 5.1).

In Fig. 5.5 we show $\bar{I}_{\parallel}(\theta, \phi)$ and $\bar{I}_{\perp}(\theta, \phi)$, the average far fields obtained from measurements over 10 different positions on the solar cell. A sample of white paint serves as a comparison and as control for the instrumental response: this is a volume scatterer reflecting nearly equal amount of power in both polarizations (see Ch. 4). The backscattered far fields of the white paint are almost uniform profiles with little differences between the two polarization. For the solar cell, instead, the far fields show far more structure.

The angular profile $\bar{I}_{\parallel}(\theta, \phi)$ depicted in Fig. 5.5 (a) contains two main features: a diffuse component spread over a wide angle, and a bright spot centered at polar angle $\theta = 0$. These components are expected in the reflectance of a textured solar cell [25]. The interfacial reflections from the optics show up as a minor contribution to the specular reflection.

Both the diffuse and specular components are visible in the cross section in Fig. 5.5 (e). The diffuse part, with a maximum at $\theta = 0$, monotonically

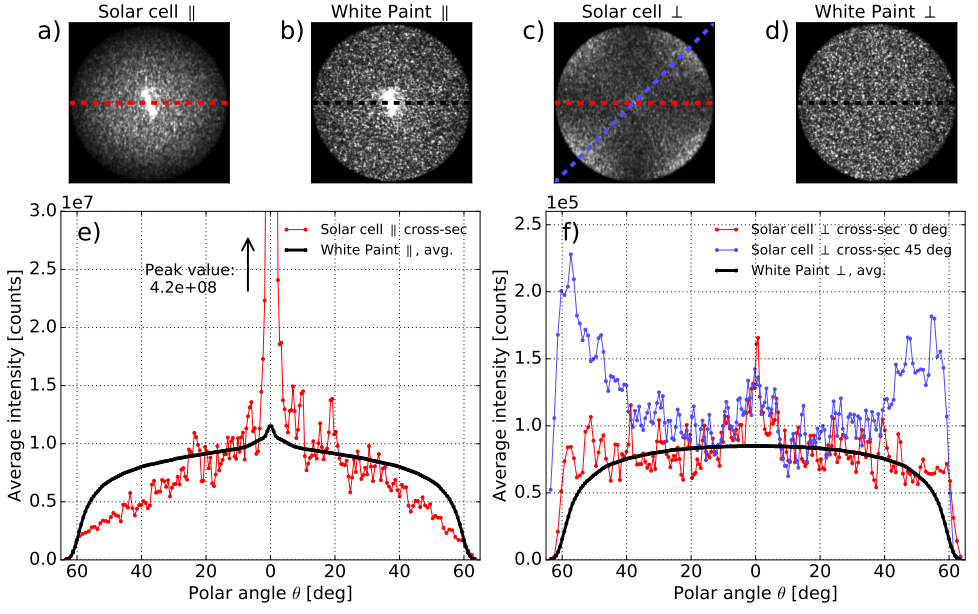

Figure 5.5: Far field reflection patterns from the solar cell and a sample of white paint, used as a comparison. Top panels (a-d): far field profiles for both parallel and orthogonal polarizations for the two samples. Bottom plots (e-f): reflected intensity profiles for parallel (left) and orthogonal (right) polarization. For the solar cell we report cross sections of the far field intensities (red and blue lines), obtained along the dashed lines in the upper panels, whilst for the white paint we show the azimuthally averaged profiles (black dashed line), conveniently rescaled for comparison purposes.

decreases with increasing polar angle and reduces to one fourth of its shoulder value at $\theta \simeq 60°$. The specular reflection instead has the form of a bright peak centred also at $\theta = 0$, with a full width half maximum of $1.2\,°$, which accounts for a fraction of 0.11 of the total collected reflected power. The attribution of this peak to the specular component is confirmed by the data for the flat-Si reference sample.

The depolarized component of the reflection $\bar{I}_\perp(\theta, \phi)$ is pictured in Fig. 5.5 (c). Differently from the parallel polarization case, this shows no specular peak and has a clear dependence on the azimuthally angle in the shape of four lobes peaked at the positions $\phi = (2n + 1)\pi/4$. The two cross sections of $\bar{I}_\perp(\theta, \phi)$ for $\phi = 0, \pi/4$, shown in Fig. 5.5 (f), help to see the relevance of the four peaks in the far field profile.

In order to understand the features of $\bar{I}_\perp(\theta, \phi)$ we write it as the sum of two components $I_C(\theta)$ and $I_A(\theta, \phi)$, the second describing the four-lobed

oscillation with ϕ:

$$I_{\perp}^{fit}(\theta,\phi) = I_A(\theta,\phi) + I_C(\theta,\phi) = A_{\perp}(\theta)\,\sin^2(2\phi) + C_{\perp}(\theta) \tag{5.1}$$

We use Eq. (5.1) to fit the measured far field $\bar{I}_{\perp}(\theta,\phi)$. In Fig. 5.6 (b) we show the calculated best values for the functions $C_{\perp}(\theta)$ and $A_{\perp}(\theta)$, together with the averaged profile for the diffuse reflection in parallel polarization $\left\langle \bar{I}_{\parallel}(\theta,\phi)\right\rangle_{\phi}$.

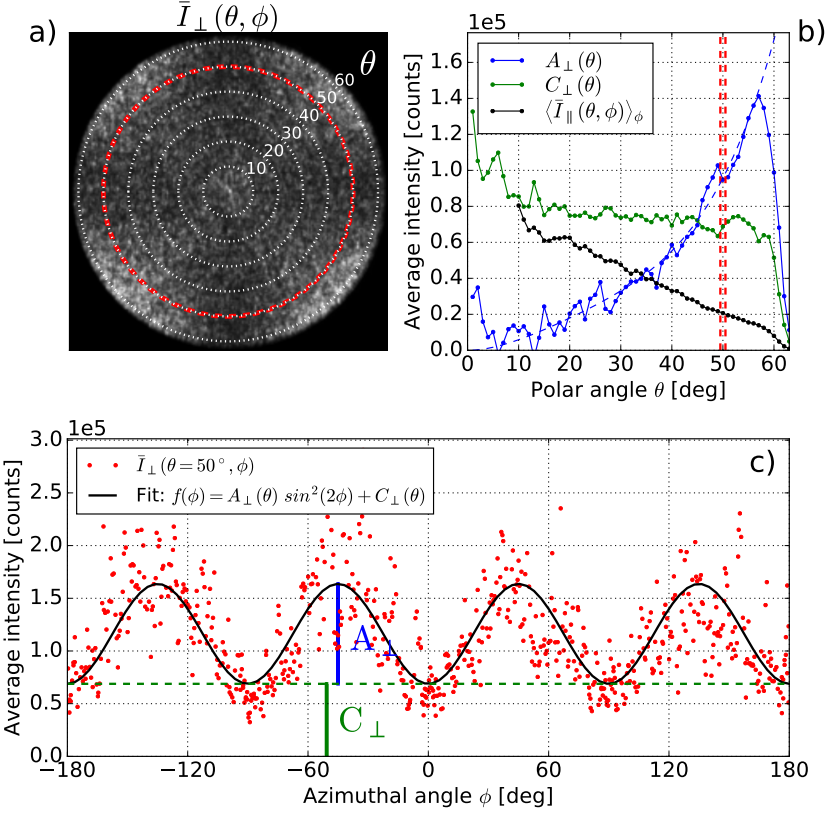

Figure 5.6: Analysis of the far field for the depolarized component of the solar cell reflection. (a) Average far field pattern $\bar{I}_{\perp}(\theta,\phi)$ with lines indicating constant polar angle values. The two red dashed circles highlight the region $\theta = (50 \pm 1)°$; (b) fit parameter $A_{\perp}(\theta)$ and $C_{\perp}(\theta)$ for the fit function from Eq. (5.1). The azimuthally average $\left\langle \bar{I}_{\parallel}(\theta,\phi)\right\rangle_{\phi}$ is shown, rescaled, for comparison. The red dashed lines indicate the region highlighted in a), while the dashed blue line is a 4^{th} order polynomial fit used later in the text. (c) Reflected intensity as function of azimuthal angle ϕ for the polar angle region $\theta = (50 \pm 1)°$ highlighted in a), with the best fit function.

The two functions $A_{\perp}(\theta)$ and $C_{\perp}(\theta)$ show no resemblance with each other

or with $\left\langle \bar{I}_{\parallel}(\theta,\phi) \right\rangle_{\phi}$. The coefficient $C_{\perp}(\theta)$ is almost constant in the accessible angular range, except for a peak located at $\theta < 10°$. The function $A_{\perp}(\theta)$, instead, tends to zero at $\theta = 0$ and increases continuously with θ, reaching a peak at the edge of the detection angle, with a value even two times higher than $C(\theta)$ at the same polar angle.

A possible origin for the four-lobed structure of $\bar{I}_{\perp}(\theta,\phi)$ is the polarization dependence of the Fresnel reflection coefficients. This explanation, detailed by the facets model in Appendix 5.A and formalized in Eqs. (5.13-5.14), captures both the $\sin^2(2\phi)$ dependence of the far field intensity as well as the shape of $A(\theta)$ profile, but not the presence of the azimuthally constant coefficient $C_{\perp}(\theta)$.

The facets model also predicts a weak two-lobed structure for the parallel polarization case. We check this in our data for $\bar{I}_{\parallel}(\theta,\phi)$ by fitting the measured far field with the model derived from Eqs. Eqs. (5.12) and (5.14):

$$I_{\parallel}^{fit}(\theta,\phi) = A_{\parallel}(\theta)\,\cos(2\phi) + C_{\parallel}(\theta) + \frac{A_{\parallel}^2(\theta)}{4\,C_{\parallel}(\theta)}\cos^2(2\phi) \tag{5.2}$$

The results of the fit, shown in Fig. 5.7, confirms that $\bar{I}_{\parallel}(\theta,\phi)$ oscillates twice along the azimuthal angle as predicted by the facets model. The values we find for $A_{\parallel}(\theta)$ and $C_{\parallel}(\theta)$ make the third term in Eq. (5.2) relatively small.

The results of this simple analysis for far fields patterns suggest that some of the features can be explained by a flat-interface reflection approximation applied to a rough interface. Nevertheless, we note that the ratio between the lobes amplitude and the constant signal for parallel polarization is $A_{\perp}(\theta)/\,C_{\parallel}(\theta) \simeq 0.03$ at $\theta = 50°$, while a similar calculation for a air-Si interface considered in appendix 5.A leads to a value about 10 times lower. We attribute the discrepancy between data and calculations to the simplification of the model, which doesn't account for the layered structure of the sample and thus neglects refraction and multiple scattering involving the Ag back-reflector.

The second contribution to the far field in orthogonal polarization is the diffuse component $I_C(\theta,\phi)$. This accounts for a fraction of the reflected power $P_C/(P_A + P_C) = 0.67$, with the optical powers calculated as $P_{A/C} = \int\int I_{A/C}(\theta,\phi)\,\theta\,d\theta d\phi$; this is equivalent to about 1% of the total power reflected by the solar cell. It is reasonable to assume that a far field component similar to $I_C(\theta,\phi)$ exists also for the reflection in parallel polarization,

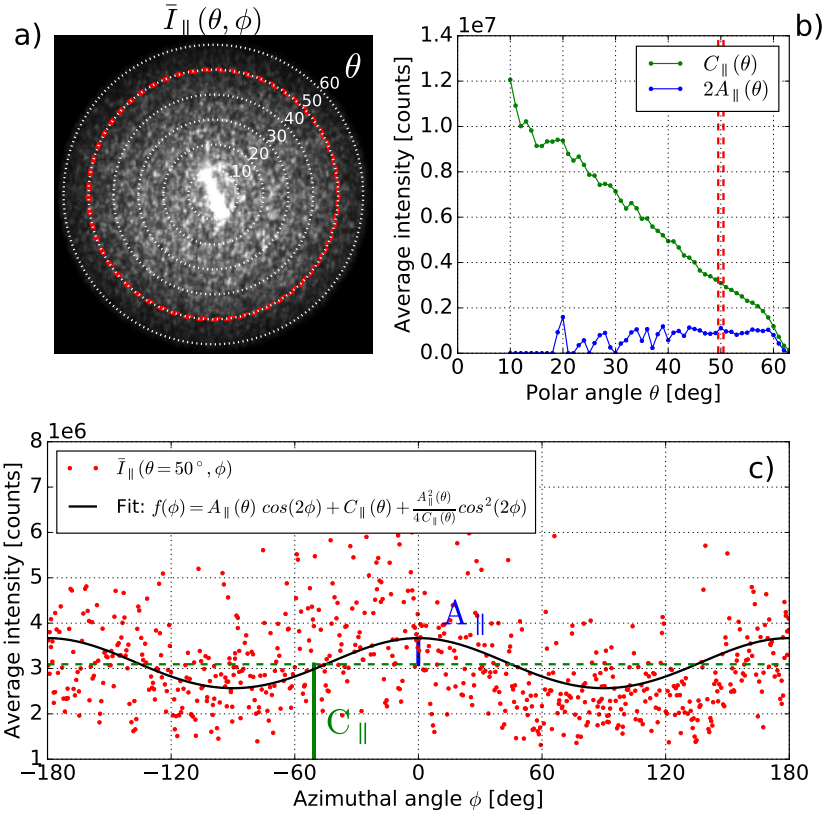

Figure 5.7: Cell reflection in parallel polarization, analysis of the far field. (a) average far field pattern $\bar{I}_{\perp}(\theta,\phi)$ with lines indicating constant polar angle values. The two red dashed circles highlight the region $\theta = (50 \pm 1)°$; (b) fit parameter $A_{\parallel}(\theta)$ and $C_{\parallel}(\theta)$ from the fit function in Eq. (5.2). The red dashed lines indicate the region highlighted in a). (c) reflected intensity as function of azimuthal angle ϕ for the polar angle region $\theta = (50 \pm 1)°$ highlighted in a), with the best fit function.

but this is not detectable as it would be much weaker than the much stronger diffuse signal (see Fig. 5.5 (e)).

It remains to specify the physical origin of $I_C(\theta,\phi)$. We attribute this to the fraction of the field, trapped in the waveguide-like structure, which escape from the solar cell after multiple scattering events. A confirmation for this interpretation comes from the shape of $I_C(\theta,\phi)$ which shows an additional peak centred at $\theta = 0$, which we attribute to coherent enhanced backscattering (EBS).

The origin of EBS is interference: this is a robust effect present in random scattering media [26, 27, 28], including rough interfaces, both metallic or

dielectric [29, 30]. In EBS reciprocal scattering paths interfere constructively and result in a peak centred at the backscattering direction with intensity up to two times the diffuse background. The backscattering cone can be obtained for both the co-polarized and depolarized light, with non-trivial differences between the two cases[31, 32, 33], and its width is Fourier related to the average propagation distance of the light in the scattering medium.

Figure 5.8 shows the details of the peak that we observe in $I_C(\theta)$. This is obtained by subtracting from $\bar{I}_\perp(\theta,\phi)$ the four-lobed component calculated as $\tilde{A}_\perp(\theta)\sin^2(2\phi)$, with $\tilde{A}_\perp(\theta)$ the 4^{th} order best fit polynomial for $A_\perp(\theta)$, obtained imposing $\tilde{A}_\perp(0)=0$ and $\tilde{A}'_\perp(0)=0$ and shown in Fig. 5.6.

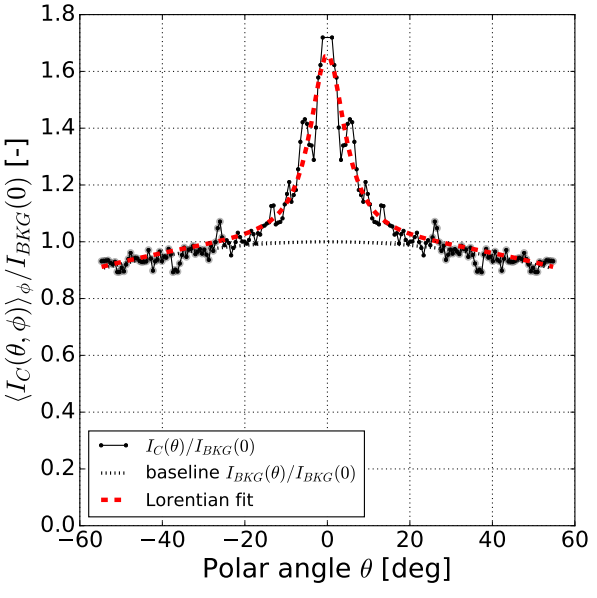

Figure 5.8: Result for the function $\langle I_C(\theta,\phi)\rangle_\phi$ calculated as explained in the text, highlighting the back scattering cone. Data are mirrored to negative θ to give a better impression of the peak. A 2^{nd} order polynomial is used to fit the background diffuse intensity $I_{BKG}(\theta)$ (dashed line). All intensities are divided by $I_{BKG}(0)$.

The exact shape of the enhanced backscattering peak requires a more detailed description; in absence of a theory for optical transport in our absorbing 2D scattering medium, we fit $I_C(\theta)$ with the sum of a phenomenological parabolic baseline function $I_{BKG}(\theta) = (-7.8\,\theta^2 + 76)\cdot 10^3$ and a Lorentian curve for the peak. The result yields an enhancement factor value $I_C(0)/I_{BKG}(0) = 1.6$.

For the full width at half maximum of the Lorentian peak we find $\Delta\theta_{EBS} \simeq 10$ deg. This corresponds to a transport mean free path of $l_t = 0.4\,\mu$m, that we obtain by using the standard relation $\Delta\theta_{EBS} = K_{EBS}\frac{\lambda_0}{2\pi l_t}$, with $K_{EBS} = 0.7$. This result is dictated by the value of the pre-factor K_{EBS}, which depends on different aspects of the scattering experiment. The value we use is valid for 3D scattering media and accounts also for long propagation paths contributions [34]. This is a case different from ours, nevertheless in our solar cell the scattering medium lower dimensionality and the presence of absorption tend to respectively reduce and increase the value of the pre-factor, balancing potential deviations. Since a detailed investigation on the EBS effect in our sample is beyond the scope of this work, we consider the calculated value for transport mean free path a satisfactory approximation.

5.6 Light-transport measurement

The results shown so far do not give information on the optical transport of light entering the solar cell. This is an important aspect to evaluate the potential for coherent enhanced absorption (CEA) in our structure is the presence of light transport in the structure. In this section we study the propagation of light trapped inside the solar cell by placing a knife edge immediately in front of the SLM to block half of the incident beam. The resulting light distribution is imaged on the sample surface providing a diffraction limited intensity step.

On the illuminated side, light is scattered into the absorbing layer by the features of the surface morphology, and is guided in the layer stack. This field also diffuses into the dark region, where part of it scatters again on the rough interface. The result is the presence of backscattered light originating also from the non-illuminated area. We study the spatial decay profile of this component of the reflected intensity distribution to obtain information on the light-transport process inside the solar cell.

While illuminating the sample with light polarized along x, i.e. perpendicular to the direction of the knife edge (see Fig. 5.3), we separately detect the two polarization components of the reflected light. We look at a selected area of the image and average over the speckle-like pattern. This area is indicated in Fig. 5.4: it is centred on the beam center, spans the full image in the x direction and 9 μm (100 pixels) in the y direction. The incident intensity in this region is almost independent of y, and by averaging in this direction we obtain the average reflected intensities for both polarizations $\bar{I}_{\parallel}(x)$ and $\bar{I}_{\perp}(x)$,

with that the knife edge positioned at $x = 0$.

Figure 5.9 shows the averaged intensity profiles for the solar cell and the flat silicon sample for both polarization directions $\bar{I}_{\parallel/\perp}(x)$, after normalization to the maximum of the incident intensity $I_{in}(0,0)$. The reflected light originating from the non-illuminated area is the combined result of diffraction effects, light propagation and in and out-of-plan scattering. This *light in the darkness* is most easily observable in the data for orthogonal polarization.

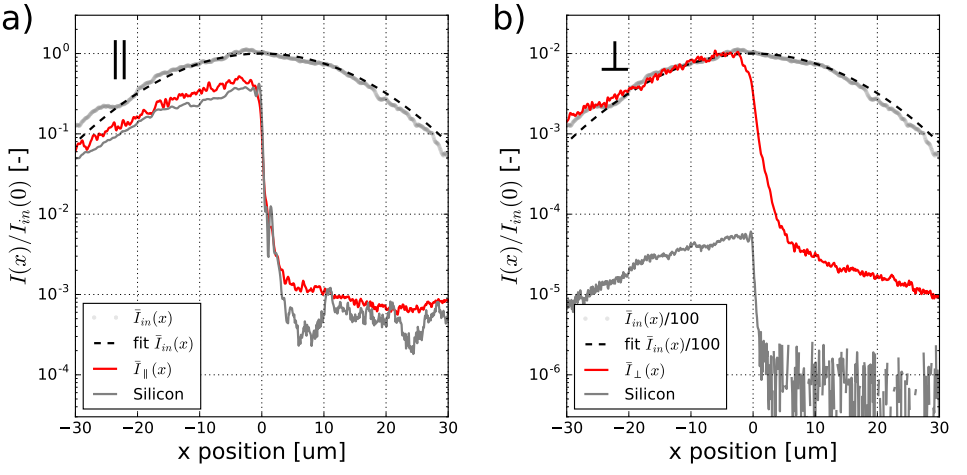

Figure 5.9: Measured average intensities (a) $\bar{I}_{\parallel}(x)$ and (b) $\bar{I}_{\perp}(x)$ normalized to $I_{in}(0,0)$. We show the results for both the solar cell (red) and the flat silicon wafer used as a reference (gray). Both panels also show the incident beam profile in the absence of the knife edge, with the best Gaussian fit, for shape comparison.

5.6.1 Effects of diffraction (reference sample)

As a first step, we study the effect of diffraction. For simplicity, we consider a source in the shape of a half-plane homogeneous illumination positioned at the SLM plane and aligned with the knife edge. The source is described by the field $E_{in}(x) = E_0\,(\frac{1}{2} + \frac{1}{2}\,sign(x))$. The inclusion of the effects of the limited numerical aperture of our optical system yields the following expression for the field incident on the solar cell:

$$E_{out}(x) = \frac{1}{2\pi}\int_{-k_M}^{k_M} e^{ikx}\int_{-\infty}^{\infty} E_{in}(x)\,e^{-ikx}dxdk = E_0\left(\frac{1}{2} + \frac{Si(x\,k_{max})}{\pi}\right) \quad (5.3)$$

with $k_M = 2\pi/\lambda_0$ NA and $Si(y)$ the *sine integral* function defined as $Si(y) = \int_0^y \frac{\sin(t)}{t}dt$.

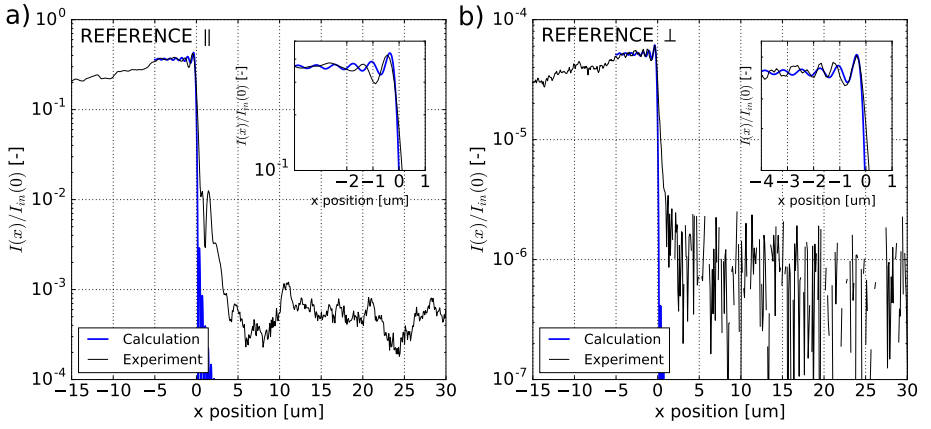

Figure 5.10: Detail of the reflected intensity curves in Fig. 5.9 for (a) parallel and (b) orthogonal polarization for the flat silicon (black line) compared to the model for the diffraction limited image of a half-plane illumination in Eq. (5.3) (blue line). The insets show the detail of the region around $x = 0$.

In Fig. 5.10 we show the results of this calculation for $I_k(x) = |E_{out}(x)|^2$ together with our experimental data. With the peak signal amplitude as the only adjustable parameter, the calculated curve approximately yields the steepness of the knife edge reflection for the reference sample. It also reproduces both amplitude and spatial period of the diffraction fringes in the high intensity region, as highlighted in the insets in Fig. 5.10 (b). The nice agreement between experimental data and theory shows that the spatial resolution in our setup is limited by diffraction. The profile $\bar{I}_{\parallel}(x)$ for the reference sample contains a spurious signal for $x \gtrsim 0$ μm. As mentioned previously, we attribute this to light reflected off the microscope objective. This spurious signal is less visible in $\bar{I}_{\perp}(x)$ as it is much weaker there, having a strength comparable to the noise.

5.6.2 Effects of 2D transport (solar cell sample)

The reflected intensity profiles for the knife edge illumination experiment on the solar cell are reported in Fig. 5.11. These show slower intensity decay for $x > 0$ and a rounded feature in the region $-3\,\mu\text{m} < x < 0\,\mu\text{m}$, in place of the sharp kink at $x = 0$ visible for the reference sample. These are both signatures of light diffusion becoming apparent at the light-dark boundary, similarly to the results for the white paint random medium in Ch. 4. The shape of these profiles provide information on the diffusion process.

To model the effect of 2D transport on the reflected intensities $I_{\parallel/\perp}(x)$ we simplify the symmetry of the problem and consider the case of a homo-

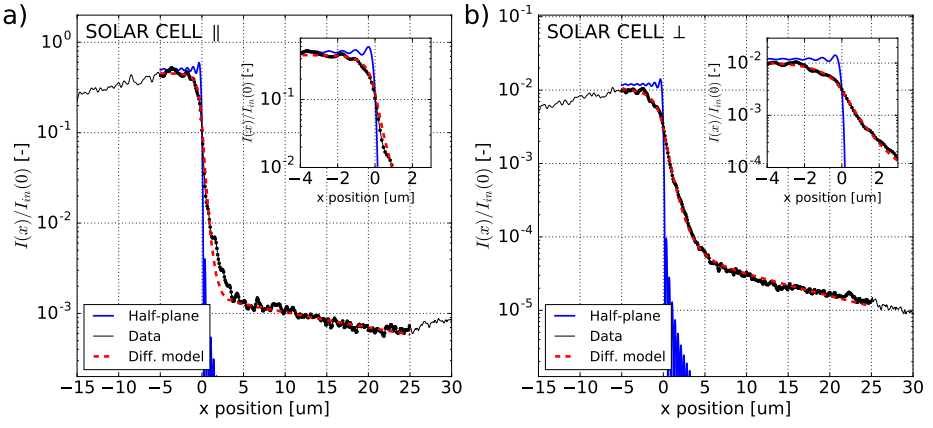

Figure 5.11: Reflected intensity curves for parallel and orthogonal polarization for the solar cell (black lines) with fit curves (dashed red line) from the model (Eq. (5.5)), and the profile for the diffraction limited image of an illuminated half plane in the absence of diffusion (blue line). The insets show the detail of the region around $x = 0$ highlighting the effect of diffusion. The data range used for the fits extends from $x = -5\,\mu$m to $x = 25\,\mu$m.

geneously illuminated half plane; under these conditions the diffusion can be considered a 1D process. For the field diffusion Green's function $G_{1D}(x, x')$ we use the general Ansatz:

$$G_{1D}^{(N)}(x, x') = G_{1D}^{(N)}(x - x') = \sum_{i}^{N} w_i \frac{1}{2\xi_i} e^{-|x-x'|/\xi_i} \tag{5.4}$$

with relative weights $\sum_i^N w_i = 1$, where ξ_i are the field decay lengths of the relevant decay components and $\int_\infty^\infty \frac{1}{2\xi_i} e^{-|x|/\xi_i}\, dx = 1$.

The combined effect of diffraction and field diffusion can be calculated from the convolution of Eqs. (5.3) and (5.4). We use $N = 2$ to allow two separate spatial decay processes and obtain for the intensity profile function:

$$I_{1D}^{(2)}(x) = \left| G_{1D}^{(2)}(x) * E_{out}(x) \right|^2 \tag{5.5}$$

We calculate Eq. (5.5) numerically and fit it to the measured intensity profiles $I_{\parallel/\perp}(x)$ for the solar cell. The results are also shown in Fig. 5.11.

For the orthogonal polarization (panel Fig. 5.11 (b)) this analysis yields a strong fast decay component with $\xi_1^\perp = 1.26 \pm 0.02\,\mu$m and relative weight $w_1^\perp = 0.85 \pm 0.01$, and a slow decay component with $\xi_2^\perp = 25 \pm 2\,\mu$m. For the parallel polarization (panel Fig. 5.11 (a)) the fit yields $\xi_1^\parallel = 0.55 \pm 0.01\,\mu$m

with a relative weight $w_1^{\parallel} = 0.89 \pm 0.01$ and a slowly decaying component with $\xi_2^{\parallel} = 41 \pm 7\,\mu$m.

The features of the reflected intensity profiles for knife edge illumination on the solar cell are nicely captured by the model in Eq. (5.5) and yield well-defined values for $\xi_i^{\parallel/\perp}$ and w_i. For parallel polarization the observed signal contains direct reflections from the microscope objective that are not included in Eq. (5.5). On the contrary, the intensity for orthogonally polarized light $\bar{I}_{\perp}(x)$ originates dominantly from depolarization effects caused by the sample structure, as emerges from the comparison with the reference sample. This makes the orthogonal polarization case more reliable and of particular interest; we hence examine this component closely.

The best-fit curve for $\bar{I}_{\perp}(x)$ shows that two spatial decay rates for 1D field diffusion are sufficient to describe the shape of the experimental data. We attribute the value of $\xi_1^{\perp} = 1.26 \pm 0.02\,\mu$m to the actual spatial decay of the light guided inside the layered structure. This decay is very fast and results from the combination of absorption and in-plane scattering in the Si layer, together with the losses due to light escaping the rough structure. By considering only these three processes, we implicitly assume that light trapped in the slab is equally distributed between modes that couple to either parallel or orthogonal polarization components in the far field. Without this assumption, an additional scattering-mediated exchange of energy between two sets of modes should be considered.

The decay at longer scale with $\xi_2^{\perp} = 25 \pm 2\,\mu$m is more difficult to interpret. We identify two possible mechanisms giving rise to such a feature. The first is the presence of guided modes that experience weak absorption and propagate for longer distances in the structure. The second mechanism is light that propagates at the solar cell surface close to grazing angle and scatters over roughness features towards the objective. We examine in more detail the first hypothesis in Sec. 5.7.

5.6.3 Phase-step method applied to solar cells

An alternative approach for measuring the transport properties of a scattering medium is the phase-step method, explained in Ch. 4. In our setup we implement this method by using the SLM positioned at an image plane of the sample. A set of n holograms is displayed on the SLM, with different values of the phase difference $\Delta\Phi_n$ between the two regions indicated with L and R in the inset in Fig. 5.3. In the regions close to the phase-step, the combination

of transport and interference produces a sinusoidal oscillation of the local intensity as a function of $\Delta\Phi_n$. The amplitude of this oscillation $A_{\parallel,\perp}(x,y)$ is a function of the position over the sample and depends on the optical transport in the sample.

We calculate $A_{\parallel,\perp}(x,y)$ from the same region considered for the knife edge experiment, indicated in Fig. 5.4 (a-b). By averaging $A_{\parallel,\perp}(x,y)$ along y we calculate $A_\perp(x)$, shown in Fig. 5.12, which we rescale by the incident intensity to obtain a relative amplitude oscillation. We don't present the results for the reflection in parallel polarization as these are again affected by the interfacial reflections from the microscope objective.

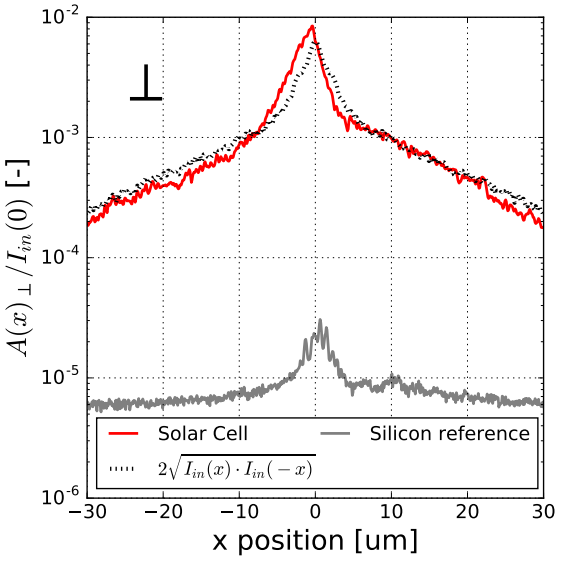

Figure 5.12: Results of the phase-step method applied on the solar cell. The average amplitude of the intensity oscillation $A_\perp(x)$ for the solar cell (red line) is compared with the same quantity measured on the flat Si (light gray). The dashed curve shows the equivalent curve $f(x) = 2\sqrt{\bar{I}_\perp(x)\,\bar{I}_\perp(-x)}$ calculated using the results from the knife experiment.

Figure 5.12 shows that the signal $A_\perp(x)$ is much stronger for the solar cell than for the reference and hence is a reliable signal. The shape of $A_\perp(x)$ provides information on the transport and scattering properties of the solar cell: it shows two main regions for $|x| \lesssim 5\,\mu$m and $|x| \gtrsim 5\,\mu$m, with respectively a faster and slower decay of the function value.

In chapter 4 we noted that the phase-step and knife-edge experiments yield similar information. We highlight this by comparing $A_\perp(x)$ with the equivalent curve obtained from the knife-edge data $f(x) = 2\sqrt{\bar{I}_\perp(x)\,\bar{I}_\perp(-x)}$, to obtain good quantitative agreement (see Fig. 5.12). The only difference between the two cases is the larger amplitude of the phase-step signal as compared to the knife edge measurements.

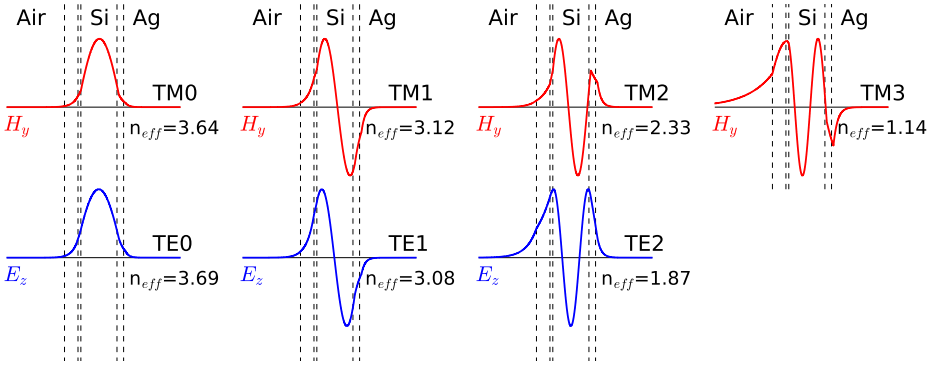

Figure 5.13: Field profiles for (Top) the (in-plane) magnetic field component for the TM guided modes and (Bottom) the (in-plane) electric field component for TE modes supported by the flat layered structure.

5.7 Guided modes in the layered structure

The structure of our solar cell supports guided modes, but their free propagation is affected by roughness-induced scattering. The supported guided modes and their properties can be determined using the *transfer matrices technique*, a standard method in stratified media, considering a smooth layered waveguide in place of our rough structure. This allows to calculate typical propagation lengths of the eigenmodes of the structure in the absence of scattering but in presence of absorption.

Transfer matrices are generally used to model reflection and transmission of plane waves in multilayer structures. These 2×2 matrices relate the amplitudes of forward and backward propagating plane waves components within the different layers of the structure. The overall transfer matrix M^π of the layer stack is obtained, for each polarization $\pi = TM/TE$, by multiplications of the matrices $T^\pi_{i,j}$ and P^π_i describing respectively the refraction at the i-j interface and propagation in the i-th layer.

Here we calculate the transfer matrices for our system $M^\pi(k_\parallel)$ as functions of the in-plane component of the wavevector. For the optical properties of the materials we use the complex valued permittivities $\epsilon = \epsilon' + i\epsilon''$, indicated in Tab. 5.1. Real valued ϵ are considered only for the doped SiO_x layers, which are very thin and hence have little influence. The guided modes supported by a stack correspond to the minima of the matrix element $M^\pi_{1,1}(k_\parallel)$ in the range for $k_\parallel > 2\pi/\lambda_0$ where modes have field evanescent in air. More details on the

method we use are available in Ref. [38]. The field profiles for the allowed modes are shown in Fig. 5.13.

	ϵ_r	thickness [nm]
Air	1.00	-
ITO	3.18+j0.01	75
p-SiO_x-H	7.29	16
i-Si-H	15.07+j0.15	200
n-SiO_x-H	4.84	37
Ag	-18.29+j0.48	300

Table 5.1: Values of the relative permittivity of the materials of the solar cell layers. Values for the thicker layers are obtained from literature for $\lambda = 633$ nm (ITO [35], Si [36], Ag [37]). For the p and n doped regions we use the refractive index for $\lambda = 800$ nm specified by the producer of the sample (TU Delft, Prof. M. Zeman Group): the precise value of these refractive indices is less important due to the very small thickness of the doped layers.

Guided light is mainly absorbed in the Si layer, where most of the field is localized, and partially in the metallic reflector. We can calculate the absorption decay rate in the stack by considering the absorption as a weak perturbation to a non-absorbing system. This approximation is justified when the complex refractive indices $n = n' + in''$ of the absorbing media are such that $n'' \ll n'$, as for the case of Si with $n_{Si}(\lambda = 633\,\mathrm{nm}) = 3.88 + j0.02$.

Given the values for $k_{\|}$ for each of the allowed modes it is possible to also calculate the imaginary part of the effective refractive index $n_{eff} = n'_{eff} + i\, n''_{eff}$, where $n'_{eff} \equiv k_{\|}/k_0$. We use the results from [39] which read:

$$\text{TE modes}: \quad n''_{eff} = \frac{k_0}{2\, n_{eff}} \frac{\int_\infty^\infty \epsilon''_r |E_y|^2\, dz}{\int_\infty^\infty |E_y|^2\, dz} \tag{5.6}$$

$$\text{TM modes}: \quad n''_{eff} = \frac{n_{eff} k_0}{2} \frac{\int_\infty^\infty \epsilon''_r |E_z|^2\, dz}{\int_\infty^\infty \epsilon'_r |E_z|^2\, dz} \tag{5.7}$$

where the expression for the TM modes is an approximation based on the assumption $E_x \ll E_z$ [39].

The results for the effective refractive indices of the allowed guided modes are reported in Table 5.2, where we also calculate the absorption length $L_{abs} = \lambda/(4\pi\, n''_{eff})$. All calculated absorption propagation lengths L_{abs} are larger than the measured diffusion length for the field reported in Sec. 5.6.

	n'_{eff}	n''_{eff}	L_{abs} [μm]
TE0	3.69	0.018	2.7
TE1	3.08	0.015	3.4
TE2	1.87	0.008	6.1
TM0	3.64	0.018	2.8
TM1	3.12	0.008	6.1
TM2	2.33	0.010	5.2
TM3	1.14	0.002	31.8

Table 5.2: Calculated values for the real and imaginary parts of the effective refractive indices n_{eff} of the modes supported by the plane layered structure, together with the absorption propagation lengths L_{abs}.

This is expected as, in the real sample, light transported in the slab is slowed down by scattering in the layer and is subject to losses due to scattering to free space. We can estimate the scattering mean free path l_{sca} using our experimental value for the field decay length for orthogonal polarization $\xi^{\perp}$ and the modelled values for L_{abs} using the relation for the extinction mean free path:

$$l_{ex} = \left(L_{abs}^{-1} + l_{sca}^{-1}\right)^{-1} \tag{5.8}$$

substituting $l_{ex} = \xi_1^{\perp}/2$.

This value accounts for both the scattering within the solar cell as well as the scattering to the outside in the form of backscattered light. This is meant as an estimation and hints to the fact that in our system scattering happens on a scale very similar to absorption.

From table 5.2 we also note that among the modes supported by the slab, the TM3 has a very long absorption length, even longer than the extinction mean free path obtained from the measured slow decay constant for the field $l_{ex} = \xi_2^{\perp}/2 \simeq 12.5\,\mu$m. This supports the hypothesis that the slow intensity decay observed in the knife edge experiment could be caused by a weakly absorbed mode supported by the structure. This mode is bound to also experience less scattering than the other eigenmodes of the structure, but this can only be calculated with a more detailed analysis of 2D scattering.

5.8 Summary

We have studied the scattering of coherent polarized light on a rough solar cell, with the goal to determine the scattering properties of the thin Si film

and the propagation of light trapped in the cell.

We found that the observed light backscattered by our solar cell mostly retains the incident polarization, with only a small fraction (about 2%) of it reflected in the orthogonal polarization. This suggests that the backscattering is dominated by direct reflection from the different layers of the solar cell with a sizeable contribution from the Ag back reflector. Moreover, the reflected signal in both polarization shows correlations with the surface morphology, with the parallel polarization signal coming mostly from the ridges of the roughness profiles.

We studied the backscattered light both as a function of its scattering angle and as a function of the position where it originates on the sample. The spatially resolved measurements with the phase-step method confirmed the result of the knife-edge method.

The depolarization effect is particularly interesting as it provides important information on the scattering process. The angular distribution of the depolarized scattering comprises a four-lobed structure and a azimuthally symmetric (diffuse) component. We attribute the four-lobed component to the effect of the polarization dependence of the Fresnel coefficients upon direct reflection. By modelling the backscattered light from a rough interface with a facets model we explain the four lobes and also a two-lobed feature of the far field in parallel polarization.

The second (diffuse) component of orthogonally polarized backscattering, accounting for about 1% of the total reflection, has possible origin in the field trapped in the solar cells escaping to free space after several scattering events. This component shows a central peak that we attribute to coherent backscattering and that allows us to calculate a value for the transport mean free path of light in the solar cell $l_t \simeq 0.4\,\mu$m.

After studying the angular profile of the scattered light, we investigated its spatial propagation. We illuminated the solar cell with a sharp intensity step, and measured the diffusion into the non-illuminated region of light trapped in the absorbing layer. In this experiment, we again look at the depolarized fraction of the signal, a component not affected by straylight effects. Although transport effects are clearly visible, short propagation distances make it difficult the capture the finest details. We find two different typical extinctions lengths: $l_{ex}^{(1)} = \xi_1^{\perp}/2 = 0.63 \pm 0.01\,\mu$m, and a much longer $l_{ex}^{(2)} = \xi_2^{\perp}/2 = 12 \pm 1\,\mu$m. The value for $l_{ex}^{(1)}t$ is comparable with the value for $l_t \simeq 0.4\,\mu$m calculated from the backscattering cone.

To interpret the observed extinctions lengths we calculate the guided modes supported in a layered structure with plane interfaces instead of roughness, and calculate the absorption lengths in this simplified structure. Despite being very thin, our structure is able to support seven guided modes, including both polarizations. This complicates the analysis, as each mode can experience different scattering mean free path. We find that the most confined modes have an absorption length compatible with the measured shorter extinction length; combining this result with the measurements we calculate a transport mean free path for the most confined modes of $l_t = 0.8\,\mu$m. Additionally, we find that the TM3 mode is weakly absorbed and this might explain the longer extinction length resulting from the measurements.

5.9 Concluding discussion

The experimental investigation we conducted allows to draw some general considerations on the results of our investigation, the possibility of enhancing absorption in our thin-film silicon solar cell, and possible extension of this work.

We were able to measure the extinction mean free path of light in the cell with two methods and to calculate absorption mean free paths, but the number of guided modes involved in optical propagation complicates the interpretation of the experimental parameters. It is probably technologically unrealistic to produce thinner cells supporting fewer eigenmodes, so other approaches need to be followed.

A complete description of the scattering in the solar cell would require two aspects which were not covered in this work: (i) the separation of light scattered within the solar cell structure from the scattering to outside, and (ii) the evaluation of scattering parameters for each of the guided modes separately. Numerical simulations are probably required to achieve this, or (analytic) models that quantify radiative losses on curved two-dimensional waveguides. This would also allow to address the question of how much optical power propagates in each of the guided modes.

The success of wavefront shaping techniques applied to 3D scattering media hinges on their relatively long propagation lengths and low absorption; in our 2D absorbing medium the conditions are very different. Nevertheless, it remains theoretically possible to use wavefront shaping to increase absorption. Follow-up experiments, conducted after this work was completed, indicate

that the light reflected by the solar cell in the orthogonal polarization can be reduced with wavefront shaping techniques by 50%, within the detection cone. This amounts to only 0.5% of the power incident on the cell at 633 nm for our sample and it is probably close to how much more power can be directed to *"absorptive channels"* of the structure, per polarization degrees of freedom.

One natural extension of this work, addressing several of the aspects mentioned above, includes the repetition of the same experiments at longer wavelengths. This would imply a reduction of the absorption in silicon, hence a longer extinction length, and would also reduce the number of eigenmodes in the structure, simplifying the analysis of the experimental data. Longer wavelengths are also of bigger interest in terms of applications: the absorption of silicon decreases for $\lambda > 650\,\text{nm}$, light energy becomes more difficult to harvest.

5.10 Acknowledgments

We are grateful to the group of Electrical Sustainable Energy led by Prof. M. Zeman at the Technical University of Delft, and in particular to Fai Tong Si, for the production, electronic and structural characterization of the sample we used, and to him and Dr. Olindo Isabella for their knowledge and insight in solar cell devices and help in scientific discussion. We also thank the Complex Photonics group of Twente University, and in particular to prof. Willem Vos and Dr. Oluwafemi Ojambati, for scientific discussions.

5.A Depolarization for specular reflections

Reflection from a flat surface can change the polarization state of light as a consequence of the polarization dependence of Fresnel coefficients. This doesn't only happen when the incident light is in the form of a strongly focused spot, as reported in [40], but also when a collimated beam illuminates a tilted surface. We investigate this effect to evaluate the role it can play in the depolarization properties of our solar cell.

We consider a flat surface with its normal tilted by the incidence angle angle θ_{in} with respect to the propagation direction of the incoming light and with azimuthal orientation ϕ. The electric field of the incident light is oriented along the direction $\phi = 0$. For $\phi \neq n\pi/2$ the field incident on the interface is a combination of p and s polarization:

$$E_{in}^{(p)} = E_0 \cos(\phi), \quad E_{in}^{(s)} = E_0 \sin(\phi) \tag{5.9}$$

with E_0 the amplitude of the incident field. After reflection and projection to the far field, one obtains the amplitude of the field reflected for polarization both parallel and orthogonal to the incident one as a function of the reflection angles θ and ϕ:

$$\frac{E_{r,\parallel}(\theta,\phi)}{E_0} = \frac{1}{2}(r_s + r_p) + \frac{1}{2}(r_p - r_s)\cos(2\phi) \tag{5.10}$$

$$\frac{E_{r,\perp}(\theta,\phi)}{E_0} = \frac{1}{2}(r_p - r_s)\sin(2\phi) \tag{5.11}$$

where $r_{s/p} = r_{s/p}(\theta_{in})$ are the Fresnel amplitude reflection coefficients, functions of the incidence angle, with $\theta = 2\,\theta_{in}$ the polar angle for the reflected light collection. We write the associated normalized intensities as:

$$I_\perp(\theta,\phi)/I_0 = a_\perp(\theta)\,\sin^2(2\phi) \tag{5.12}$$

$$I_\parallel(\theta,\phi)/I_0 = a_\parallel(\theta)\,\cos(2\phi) + c_\parallel(\theta) + \frac{a_\parallel^2(\theta)}{4\,c_\parallel(\theta)}\cos^2(2\phi) \tag{5.13}$$

with $I_0 = |E_0|^2$ and $a_\parallel(\theta) = \frac{1}{4}(r_p^2 + r_s^2)$, $c_\parallel(\theta) = \frac{1}{4}(r_p + r_s)^2$, and $a_\perp(\theta) = \frac{1}{4}(r_p - r_s)^2$.

We use an air-Si interface as case study to evaluate the depolarization effect introduced by Fresnel reflection at a tilted interface. In Fig. 5.14 we

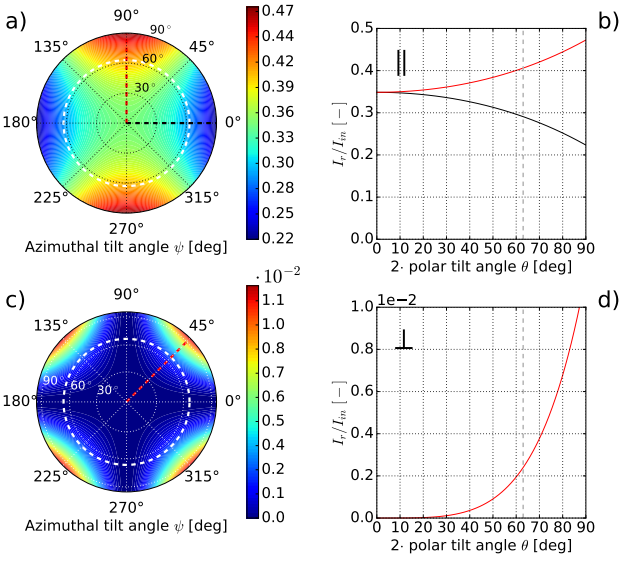

Figure 5.14: Angle dependent reflectivity for a flat surface of Si in air calculated from the models in Eqs. (5.10) and (5.11). (a,c) Reflectivity for (a) parallel and orthogonal (c) polarization $R_{\parallel/\perp}(\theta, \phi)$; (b,d) Values of $R_{\parallel/\perp}(\theta, \phi)$ at relevant azimuthal angles: for parallel polarization (b) for $\phi = 0°$ (black) and $\phi = 90°$ (red) as indicated by dashed lines in (a), and for orthogonal polarization (d) in the direction set by the lobes position $\phi = 45°$. The white dashed lines in (a) and (c) indicate the edge of the acceptance angle in our experiment.

show the calculated $R_{\parallel/\perp}(\theta, \phi) = I_{\parallel/\perp}(\theta, \phi)/I_0$ for a flat Si interface in air. The reflected intensity for parallel polarization shows two maxima and two minima as function of the azimuthal tilt. Most important, the case for orthogonal polarization yields four maxima positioned at tilt angles $\psi = (n + \pi/2)/2$.

Next, we consider the reflection from a rough surface. We interpret the structured interface as an ensemble of flat facets approximating the surface profile [41]. This ray-optics approximation neglects diffraction and interference effects, but could still describe the reflection properties of interfaces with roughness with scale $l_c > \lambda$ and $\sigma_{rms} < \lambda$. To estimate the average far fields expected for a specific interface profile we weight $R_{\parallel/\perp}(\theta, \phi)$ with the probability distributions for the tilt angles $P(\theta_{in}, \phi)$. We obtain the ensemble-averaged far field pattern for reflection:

$$\tilde{I}_{\parallel/\perp}(\theta, \phi) = P(\theta/2, \phi)\, R_{\parallel,\perp}(\theta, \phi) \tag{5.14}$$

The final far field intensity functions have the same form as in Eqs. (5.12-5.13) with the only substitution of the lowercase coefficients with the uppercase version $A_{\parallel}(\theta) = P(\theta/2, \phi)\, a_{\parallel}(\theta)$, $C_{\parallel}(\theta) = P(\theta/2, \phi)\, c_{\parallel}(\theta)$, and $A_{\perp}(\theta) = P(\theta/2, \phi)\, a_{\perp}(\theta)$.

For our sample we calculate $P(\theta_{in}, \phi)$ from the AFM profile after low-pass filtering of the spatial Fourier components of the topology, to remove features smaller than $0.1\,\mu$m (see Fig. 5.2 for a typical AFM profile of a portion of the sample). Since we find no dependence in ϕ, in Fig. 5.15 we show only $P(\theta_{in}) = 2\pi\, sin(\theta_{in})\, P(\theta_{in}, \phi)$.

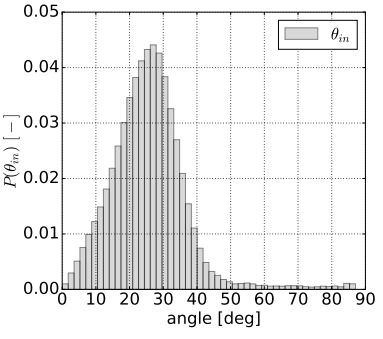

Figure 5.15: Probability density of the polar angle for the local surface normal $P(\theta_{in})$ calculated with respect to the direction of the average plane of the sample.

In Fig. 5.16 we show the far field intensity reflection, calculated from Eq. (5.14) using the function $P(\theta_{in})$ calculated for our sample and applying it to an air-Si interface.

5.B Objective shift to reduce interfacial reflection

To minimize the amount of interfacial reflections from the microscope objective reaching the camera, we shift the objective (100x, $f = 2$ mm) by about $20\,\mu$m along y. This is sufficient to reduce the intensity of the reflection from the objective on the camera by one order of magnitude, as shown from the comparison of the curves in Fig. 5.17. This shift doesn't appear to affect the steepness of the intensity step. However, it does introduce an unwanted reflection close to the intensity step ($0 < x < 2\,\mu$m).

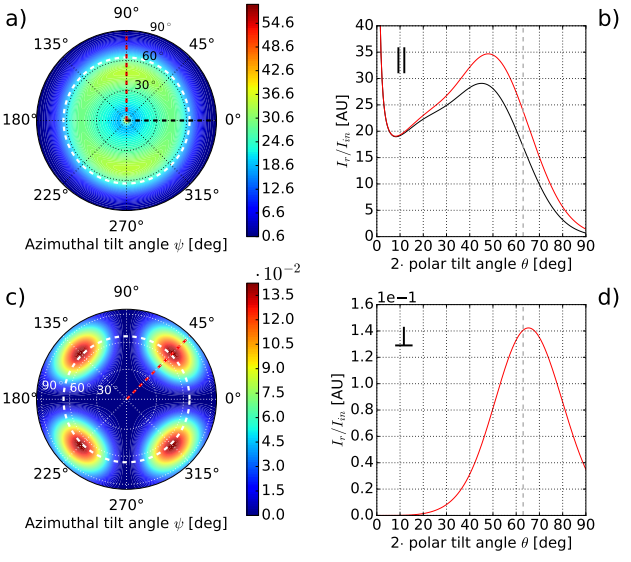

Figure 5.16: Far field reflected intensities from an air-Si interface with morphology similar to our sample, calculated from the models in Eq. (5.14) and based on the AFM data of Fig. 5.2. a) Reflected intensity $\tilde{I}_{\parallel}(\theta, \phi)$. b) Cross sections $\tilde{I}_{\parallel}(\theta)$ for $\phi = 0°$ (black) and $\phi = 90°$ (red), indicated by dashed lines in (a). c) Reflected intensity $\tilde{I}_{\perp}(\theta, \phi)$. d) Cross section $\tilde{I}_{\perp}(\theta)$ for $\phi = 45°$. The white dashed lines in (a) and (c) indicate the edge of the detection angle in our experiment.

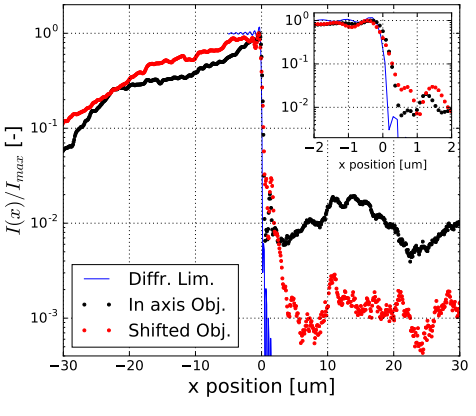

Figure 5.17: Comparison of the curves for the intensity reflected by the reference sample when measured with the microscope objective aligned with the optical axis (black) or shifted by $\Delta y \simeq 20\,\mu\mathrm{m}$ (in black). The light reflected by the objective to the camera is 10 times weaker in the case of a shifted objective. The curve for the diffraction limited image of the knife edge in Eq. (5.3) is also reported for comparison. The inset shows the detail of the curves around $x = 0$.

Bibliography

[1] F. T. Si *et al.*, *Quadruple-junction thin-film silicon-based solar cells with high open-circuit voltage*, Applied Physics Letters **105**, 063902 (2014).

[2] Z. Yu, A. Raman, and S. Fan, *Fundamental limit of nanophotonic light trapping in solar cells*, PNAS **107**, 17491 (2010).

[3] A. Polman and H. A. Atwater, *Photonic design principles for ultrahigh-efficiency photovoltaics*, Nat Mater **11**, 174 (2012).

[4] M. B. Dühring, N. A. Mortensen, and O. Sigmund, *Plasmonic versus dielectric enhancement in thin-film solar cells*, Applied Physics Letters **100**, 211914 (2012).

[5] E. Yablonovitch and G. Cody, *Intensity enhancement in textured optical sheets for solar cells*, IEEE Transactions on Electron Devices **29**, 300 (1982), bibtex: yablonovitch_intensity_1982.

[6] I. Schnitzer *et al.*, *30% external quantum efficiency from surface textured, thin-film light-emitting diodes*, Applied Physics Letters **63**, 2174 (1993).

[7] L. C. Andreani, A. Bozzola, P. Kowalczewski, and M. Liscidini, *Photonic light trapping and electrical transport in thin-film silicon solar cells*, Vol. 135 of *EMRS 2014 Spring Meeting-Advanced materials and characterization techniques for solar cells II*, Solar Energy Materials and Solar Cells **135**, 78 (2015).

[8] M. Zeman *et al.*, *Advanced Light Management Approaches for Thin-Film Silicon Solar Cells*, Vol. 15 of *International Conference on Materials for Advanced Technologies 2011, Symposium O*, Energy Procedia **15**, 189 (2012).

[9] C. van Lare, F. Lenzmann, M. A. Verschuuren, and A. Polman, *Dielectric Scattering Patterns for Efficient Light Trapping in Thin-Film Solar Cells*, Nano Lett. **15**, 4846 (2015).

[10] O. Isabella, J. Krč, and M. Zeman, *Modulated surface textures for enhanced light trapping in thin-film silicon solar cells*, Applied Physics Letters **97**, 101106 (2010).

[11] K. Jäger, M. Fischer, R. A. van Swaaij, and M. Zeman, *Designing optimized nano textures for thin-film silicon solar cells*, Opt. Express **21**, A656 (2013).

[12] M. Burresi *et al.*, *Two-dimensional disorder for broadband, omnidirectional and polarization-insensitive absorption*, Opt. Express, OE **21**, A268 (2013).

[13] C. Rockstuhl *et al.*, *Local versus global absorption in thin-film solar cells with randomly textured surfaces*, Appl. Phys. Lett. **93**, 061105 (2008).

[14] S. Rotter and S. Gigan, *Light fields in complex media: Mesoscopic scattering meets wave control*, Rev. Mod. Phys. **89**, 015005 (2017).

[15] I. M. Vellekoop and A. P. Mosk, *Focusing coherent light through opaque strongly scattering media*, Opt. Lett., OL **32**, 2309 (2007).

[16] I. M. Vellekoop and A. P. Mosk, *Universal Optimal Transmission of Light Through Disordered Materials*, Phys. Rev. Lett. **101**, 120601 (2008).

[17] J. Bertolotti *et al.*, *Non-invasive imaging through opaque scattering layers*, Nature **491**, 232 (2012).

[18] I. M. Vellekoop, E. G. van Putten, A. Lagendijk, and A. P. Mosk, *Demixing light paths inside disordered metamaterials*, Optics Express **16**, 67 (2008).

[19] S. M. Popoff *et al.*, *Measuring the Transmission Matrix in Optics: An Approach to the Study and Control of Light Propagation in Disordered Media*, Phys. Rev. Lett. **104**, 100601 (2010).

[20] Y. D. Chong and A. D. Stone, *Hidden Black: Coherent Enhancement of Absorption in Strongly Scattering Media*, Phys. Rev. Lett. **107**, 163901 (2011).

[21] S. F. Liew *et al.*, *Coherent Control of Photocurrent in a Strongly Scattering Photoelectrochemical System*, ACS Photonics **3**, 449 (2016).

[22] K. Bittkau, R. Carius, and C. Lienau, *Guided optical modes in randomly textured ZnO thin films imaged by near-field scanning optical microscopy*, Phys. Rev. B **76**, 035330 (2007).

[23] K. Bittkau *et al.*, *Nanoscale investigation of light-trapping in a-Si:H solar cell structures with randomly textured interfaces*, phys. stat. sol. (a) **205**, 2766 (2008).

[24] K. Bittkau and T. Beckers, *Near-field study of light scattering at rough interfaces of a-Si:H/μc-Si:H tandem solar cells*, phys. stat. sol. (a) **207**, 661 (2010).

[25] K. Jäger, O. Isabella, R. A. C. M. M. v. Swaaij, and M. Zeman, *Angular resolved scattering measurements of nano-textured substrates in a broad wavelength range*, Meas. Sci. Technol. **22**, 105601 (2011).

[26] M. P. V. Albada and A. Lagendijk, *Observation of Weak Localization of Light in a Random Medium*, Phys. Rev. Lett. **55**, 2692 (1985).

[27] P.-E. Wolf and G. Maret, *Weak Localization and Coherent Backscattering of Photons in Disordered Media*, Phys. Rev. Lett. **55**, 2696 (1985).

[28] E. Akkermans, P. E. Wolf, and R. Maynard, *Coherent Backscattering of Light by Disordered Media: Analysis of the Peak Line Shape*, Phys. Rev. Lett. **56**, 1471 (1986).

[29] A. A. Maradudin and E. R. Méndez, *Enhanced backscattering of light from weakly rough, random metal surfaces*, Appl. Opt., AO **32**, 3335 (1993).

[30] R. E. Luna, E. R. Méndez, J. Q. Lu, and Z.-H. Gu, *Enhanced Backscattering Due to Total Internal Reflection at a Dielectric-air Interface*, Journal of Modern Optics **42**, 257 (1995).

[31] M. P. van Albada, M. B. van der Mark, and A. Lagendijk, *Observation of weak localization of light in a finite slab: Anisotropy effects and light path classification*, Phys. Rev. Lett. **58**, 361 (1987).

[32] M. P. van Albada and A. Lagendijk, *Vector character of light in weak localization: Spatial anisotropy in coherent backscattering from a random medium*, Phys. Rev. B **36**, 2353 (1987).

[33] M. P. v. Albada, M. B. v. d. Mark, and A. Lagendijk, *Polarisation effects in weak localisation of light*, J. Phys. D: Appl. Phys. **21**, S28 (1988).

[34] M. B. van der Mark, M. P. van Albada, and A. Lagendijk, *Light scattering in strongly scattering media: Multiple scattering and weak localization*, Phys. Rev. B **37**, 3575 (1988).

[35] T. A. F. König *et al.*, *Electrically Tunable Plasmonic Behavior of Nanocube-Polymer Nanomaterials Induced by a Redox-Active Electrochromic Polymer*, ACS Nano **8**, 6182 (2014).

[36] D. E. Aspnes and A. A. Studna, *Dielectric functions and optical parameters of Si, Ge, GaP, GaAs, GaSb, InP, InAs, and InSb from 1.5 to 6.0 eV*, Phys. Rev. B **27**, 985 (1983).

[37] P. B. Johnson and R. W. Christy, *Optical Constants of the Noble Metals*, Phys. Rev. B **6**, 4370 (1972).

[38] Y. Pochi, *Optical Waves in Layered Media* (Wiley) (2005).

[39] T. D. Visser, H. Blok, B. Demeulenaere, and D. Lenstra, *Confinement factors and gain in optical amplifiers*, IEEE Journal of Quantum Electronics **33**, 1763 (1997).

[40] L. Novotny, R. D. Grober, and K. Karrai, *Reflected image of a strongly focused spot*, Opt. Lett., OL **26**, 789 (2001).

[41] S.-M. F. Nee *et al.*, *Slope distribution of a rough surface measured by transmission scattering and polarization*, Appl. Opt., AO **39**, 1561 (2000).

Samenvatting

Dit proefschrift beschrijft onderzoek naar de verstrooiing van licht aan verschillende materialen met structuren op de nanometer schaal. Verstrooiing ontstaat als licht een discontinuïteit ontmoet in de omgeving waarin het zich voortplant. Een van de belangrijkste effecten van verstrooiing is een verandering in de voortplantingsrichting van het licht. Het meten aan verstrooid licht geeft informatie over het voorwerp dat het licht verstrooit, net zoals we de wereld om ons heen reconstrueren door middel van ons gezichtsvermogen, door het waarnemen van het licht dat door de oppervlakken van materialen wordt verstrooid.

De studie van verstrooiing is vooral interessant wanneer dit voorkomt bij structuren met een grootte in de orde van de golflengte van het licht, of kleiner. Het is belangrijk om te begrijpen hoe licht zich op deze kleine schaal in zulke structuren voortplant, omdat de verkregen kennis toegepast kan worden in een groot aantal gebieden, waaronder optische communicatie, materiaaldiagnostiek en energieconversie. In de vier centrale hoofdstukken van dit proefschrift beschouwen we: (i) verstrooiing van licht dat gevangen zit op een tweedimensionale structuur en dat verstrooit aan nanometer-grote gaten in deze structuur, en (ii) meervoudige verstrooiing in materialen met twee- en drie-dimensionale wanorde.

In de hoofdstukken 2 en 3 bestuderen we de voortplanting van licht in twee verschillende tweedimensionale systemen. De eerste manier om licht in twee dimensies te vangen maakt gebruik van een dun membraan van een diëlektrisch materiaal met een brekingsindex die hoger is dan die van de omgeving. In dat geval plant het elektromagnetische veld zich voort in de vorm van geleide modi: licht is in het membraan gevangen en het kan enkel ontsnappen als er een verstoring aanwezig is, in het membraan of daar zeer dichtbij. De tweede manier van 2D-opsluiting van licht is in de vorm oppervlakteplasmonen: oscillaties van het elektromagnetisch veld en lading dicht bij een grensvlak tussen een metaal en een diëlektrisch materiaal.

In hoofdstuk 2 bestuderen we de verstrooiing door een cilindrisch gat, van licht dat zich voortplant in een tweedimensionale diëlektrische golfgeleider. We gebruiken een “Finite Difference Time Domain” numerieke simulatie, en

bepalen afzonderlijk het verstrooiingsproces in het vlak van de golfgeleider en de fractie van de intensiteit die door het gat uit het membraan ontsnapt. We nemen waar dat verstrooiing binnen het vlak groter is dan de verliezen uit het vlak. Het verstrooiingsproces vertoont kwantitatieve verschillen met de analytische theorie voor een oneindige luchtcilinder (Mie-verstrooiing). De gesimuleerde verdeling van de verstrooiingshoeken binnen het vlak toont dat een gat in een membraan niet gemodelleerd kan worden als een dipool, zelfs niet in de limiet dat de gaat heel klein is (Rayleigh-benadering).

In hoofdstuk 3 bestuderen we hoe oppervlakteplasmonen op een grenslaag tussen goud en glas, verstrooien aan nanometer-grote gaten in het metaal. We meten de hoekafhankelijke transmissie van rijen nanogaten onder belichting bij loodrechte inval. Door hun ordening in een roosterstructuur gedragen de rijen gaten zich als een diffractierooster. Uit de metingen reconstrueren we het verre-veldprofiel van het licht dat door een enkel gat wordt verspreid, door de diffractieordes in transmissie te meten voor verstrooiingshoeken tot 90 graden en voor roosters met verschillende periodiciteit. Voor s-gepolariseerde belichting vinden we een goede overeenstemming tussen onze resultaten en de bekende hoektransmissie van een enkel gat in een dunne laag metaal. Maar voor p-gepolariseerde belichting vinden we afwijkingen. We onderzoeken dit met Coupled Mode Model-berekeningen en Finite Difference Time Domain simulaties, maar het verschil wordt nog niet volledig verklaard.

In de hoofdstukken 4 en 5 bestuderen we hoe licht zich verspreidt in verschillende soorten wanordelijke verstrooiingsmedia. Deze materialen hebben een complexe structuur die de voortplantingsrichting van het licht totaal verandert na één of meerdere verstrooiingsgebeurtenissen. Voorbeelden van complexe media zijn materialen zoals papier, biologisch weefsel, en verf. Het bestuderen van de eigenschappen van wanordelijke verstrooiingsmedia is interessant voor zowel de collectieve verschijnselen, zoals Anderson-lokalisatie van licht, als voor het ontwikkelen van optische technieken om de eigenschappen van wanordelijke verstrooiingsmedia te bestuderen.

In Hoofdstuk 4 demonstreren we een nieuwe methode voor het meten van verstrooiings- en absorptie-eigenschappen van complexe media. Deze methode maakt gebruik van fase-golffrontvervorming onder coherente belichting. Complexe media reflecteren coherent licht in de vorm van een gespikkeld patroon, dat ontstaat door interferentie van meerdere voortplantingsroutes in het medium. We meten hoe dit spikkelpatroon verandert wanneer we een variabele faseverschuiving aanbrengen tussen twee naburige verlichte gebieden. De po-

sitieafhankelijkheid van deze veranderingen, die het grootst zijn vlakbij de lijn waar de verlichte gebieden elkaar raken, bevat informatie over de verstrooiings- en absorptie-eigenschappen van het medium. Wij vergelijken onze meetresultaten met voorspellingen van een eenvoudig diffusiemodel voor driedimensionale wanordelijke media. Verder vergelijken we ze met metingen met de knife-edge belichtingsmethode en met metingen aan versterkte terugverstrooiing (Enhanced Back-Scattering). Onze fase-stap methode kan gebruikt worden voor alle complexe media waarvoor lichttransport statistisch gemodelleerd kan worden. Mogelijke toepassing van deze nieuwe techniek zijn niet-invasieve studies van biologische preparaten en van andere wanordelijke verstrooiende systemen zoals gestructureerde zonnecellen of LED's.

Tenslotte bestuderen we in hoofdstuk 5 de verstrooiings- en transporteigenschappen van een ruwe dunne silicium zonnecel; een quasi-tweedimensionaal wanordelijk medium met absorptie. We verkrijgen informatie over hoe het licht de zonnecel binnentreedt, hoe het zich voortplant in de cel en hoe het ontsnapt. Daartoe worden verschillende belichtingscondities vergeleken, en worden beide gereflecteerde lineaire polarisaties bekeken. In het bijzonder observeren we de zonnecel onder knife-edge verlichting en bepalen we de extinctiecoëfficiënt door de ruimtelijke verdeling van de terugverstrooide intensiteit te meten. We interpreteren de resultaten met behulp van een golfgeleidermodel voor de toegestane modi in de siliciumlaag. Verder meten we de hoekverdeling van het gereflecteerde licht: we vinden twee bijdragen in het gedepolariseerde signaal, die we toekennen aan verschillende reflectiemechanismen. Een van de componenten vertoont een piek die we toeschrijven aan versterkte terugverstrooiing; wij gebruiken deze om de gemiddelde vrije weglengte te bepalen van licht dat in de dunne zonnecel is ingevangen. Ons onderzoek is een stap in de richting van de demonstratie van het gebruik van golffront vervorming om de absorptie te verbeteren, ook in quasi-tweedimensionale wanordelijke media.

Curriculum Vitæ

Flavio Mariani was born on the 23rd of July 1983 in Foligno, a town in the center of Italy. Between 1997 and 2002 he attended Liceo Scientifico G. Alessi in Perugia, where he developed an interest in physics and informatics.

After an initial attraction to Engineering, he, soon after, turned to Physics, after realizing that he felt more attracted to the study of its laws. He obtained his bachelor degree in 2005 with a project conducted at a neutron spectrometer at the Institute Laue-Langevin in Grenoble.

He moved to Parma for his Master's degree in Solid State Physics. During these years he was active in the University Student Union as member of the executive board and elected student representative in the Academic Senate. He completed his Master's degree in 2012 with a research project on the vibrational properties of porphyrin molecules used as functionalization on core-shell SiC nanowires, under the supervision of prof. L. Cristofolini and prof. G. Salviati.

Interested in continuing in research in Europe, he moved to the Netherlands in June 2012 to join the Quantum Optics Group at Leiden University. Under the supervision of prof. M. P. van Exter he started an experimental project on random scattering media. During his graduate studies he learned cleanroom techniques for sample fabrication, performed numerical simulations of light scattering on nanostructures, designed and executed optical experiments on nanostructures comprising plasmonic hole-arrays, 3D scattering media and two dimensional textured silicon solar cells. Part of this research was done in collaboration with other research groups within the national research program "Stirring of Light!".

Following his personal passion for space, Flavio's career continues today as an optical engineer within the Earth Observation Programme of the European Space Agency (ESA).

List of publications

- Scattering of guided light by a single hole in a dielectric slab.
  F.Mariani, M.P. van Exter,
  Optics Express **23**, 17539 (2015).

- Angle resolved transmission through metal hole gratings.
  F. Mariani, F. de León-Pérez, K. J. A. Vendel, L. Martín-Moreno, and M. P. van Exter,
  Optics Express **25**, 9061 (2017).

- Scattering media characterization with phase-only wavefront modulation.
  F. Mariani, W. Loeffler, M. Aas, O. S. Ojambati, P. Hong, W. L. Vos and M. P. van Exter,
  Submitted for publication (2017).

Acknowledgements

A thesis contains scientific results, but the road towards a PhD is a more complex learning experience, and a lot of people are part of the path leading to this booklet. On this final page I want to thank them.

First and foremost, I'm grateful to the Leiden Quantum Optics group, in particular my promotors: Martin for being my guide in these years, providing an example of sharp physical intuition and integrity, and Eric, for his straight-to-the-point understanding and example of dedication. I'm grateful to both, in particular for your support.

In the group I found many other people, passionate scientists with whom I shared fascinations, curiosities and visions. Michiel, Wolfgang, Dirk, Han, Gerard, Kier: it was a pleasure to spend time and have discussions with you, and learn something from each of you. A particular thanks goes to Henriette, our infallible and caring secretary. I also want to thank Aura and Sumant, postdocs at the beginning of my PhD, for their encouragement.

The names of colleagues and friends from my big university family that I would like to mention would fill a long list. I'm happy that my way crossed theirs, for their enthusiasm, their example, the times shared in the office, the common frustrations, the long discussions on science or philosophy or politics, the light-hearted moments of complicity, the stories from your country I haven't yet seen, the songs written together for those who left. If we shared any of these parts, you know your name is on that list, and our common memories are among the best moments of these years.

I want to thank the students that I supervised, Kim, Martijn, Amar and Michelle; having you as research partners forced me to be more accurate, and reminded me how fulfilling it is to have a smallest role in somebody else's process of understanding.

I would like to thank the electronic department, particularly Arno and Peter, and all of the FMD crew for the fast and precise technical help during these years. My gratitude also goes to Marcel Hesselbert and Dimitry Lamers (FOM institute AMOLF) for their lessons on some secrets of nano-fabrication.

My warmest thanks and affection go to the good friends that I found along the Dutch canals. I'm thinking of the *Italian gang* gathered around our

weekly risottos, and to *the three Conchettis*: it doesn't matter how international you might feel, sometimes you can use some Italian family abroad. I'm also thinking of the *Yerseke gang*; sometimes your family is the most coloured and international group of people you can imagine. I also want to thank the LSD diving association, where I found buddies that accompanied me through the silence under the water surface. The PhD is a challenging time, all these people helped keeping the morale high.

I went through a large part of this adventure with one special person: Dorina, with you I shared the most of these years, you've been the dear companion on our journeys, an important presence. You have a role in what made this booklet possible, and more importantly in the person I became. Thank you, for the big and the small things.

My everlasting gratitude goes to my parents and my family. You supported me along the road in uncountable ways, you gave me the map on which I could choose my direction. It brought me this far.